Modelling collisionally pumped X-ray lasers in optically field ionised noble gases

Lee Mark Upcraft

Submitted for the degree of Doctor of Philosophy

University of York

Department of Physics

February 2002

Abstract

This thesis presents a proof of principle investigation into the main physical processes following optical field ionisation (OFI) of noble gases. A high intensity optical laser of circular polarisation can produce a hot plasma which is capable of lasing at soft X-ray wavelengths through electron collisional excitation.

A numerical model of the driving laser which includes OFI with above threshold ionisation (ATI) and inverse bremsstrahlung (IB) heating mechanisms is used to determine the initial state of a plasma for a range of target densities and pulse polarisations. A time dependant atomic / hydrodynamics code is used to calculate gain coefficients and saturated irradiances. Large gains of the order of 100 – 1000 cm^{-1} are predicted for the valence shell lines in the range of 30 – 40 nm for eight times ionised argon, krypton and xenon. Gains of around 20 cm^{-1} are predicted for lines at 15.3 and 15.7 nm on the inner sub shell lines of argon. The saturated irradiance is found to be low at around $10^7 - 10^8$ W/cm^2.

Propagation of the driving laser pulse into the gas / plasma is examined with a code which models the ionisation induced refraction. Refraction is found to be severe and will restrict the use of these schemes to target densities of less than 10^{18} cm^3. A possible solution by using a pre-formed plasma as a wave-guiding structure is examined and it is found that plasma channels of several cm may be formed.

Finally, an examination of the non-thermal nature of the electrons within the plasma is made. For the case of the argon target it is found that a degree of elliptical polarisation in the driving laser may result in optimal pumping of the laser.

Declaration

The work presented in this thesis is entirely the work of the author except where the contributions of others have been acknowledged in the main text or by means of references.

Acknowledgements

I wish to express my sincere thanks to my supervisor Professor Geoff Pert for his support and encouragement throughout the three years of this project. Particular thanks are due for his patient and careful proof reading of this thesis at somewhat short notice.

I would also like to thank members both past and present of the Computational X-ray lasers group at York for having developed the computational codes used throughout this work. Additional thanks must go to Robert King for his insight into a number of topics discussed. Computational support from both Cliff Dixon and Sabbah Salih has been invaluable.

My thanks must be extended Stéphane Sebban at Laboratoire d'Optique Appliquée in Paris for his patience in answering my many queries over his recent experimental observation of the schemes discussed in this thesis and for his considerable help in assisting me to move to the same laboratory. Finally, I should like to thank all the staff associated with the VULCAN facility at the Rutherford Appleton Laboratory for their help in the training sessions I have attended there, and for allowing me to see some of the "real physics" behind the computational work considered here.

Preface

Chapter 1 reviews the subject of X-ray lasers and briefly examines the main difficulties in producing tabletop devices. A number of different methods of producing coherent X-ray radiation are discussed including those from well established techniques to less well proven methods. Some possible applications for such devices are mentioned.

Chapter 2 – The general theory underlying optically field ionised collisionally pumped X-ray lasers is presented. This includes the processes responsible for creating a suitable plasma, the relevant atomic and plasma physics and the propagation of the optical driving pulse.

Chapter 3 – The production and evaluation of the atomic data necessary to model collisionally pumped lasers using the atomic theory presented in the previous chapter is discussed here.

Chapter 4 – Calculations are shown for the gain and saturated irradiance of the noble gas schemes. The effect of changing the degree of polarisation of the driving beam is examined as are the dominant processes responsible for broadening the X-ray laser beam.

Chapter 5 – Propagation of the driving pulse into the gaseous targets is examined. Ionisation profiles of the plasma are shown and the resulting break-up of the driving beam discussed. A novel solution to problem of beam break-up by a pre-formed hydrogen plasma is presented and results examined.

Chapter 6 – An examination of the true electron energy distribution following optical field ionisation is presented. Results obtained from a code developed to model an arbitrary distribution are compared with the thermal Maxwell-Boltzmann distribution upon which much of the previous modelling has been based.

Chapter 7 – Conclusions are made on the overall feasibility of the schemes examined and future possible work is identified.

Chapters 4, 5 & 6 are structured in roughly the same manner in that detailed analysis and discussion is firstly presented for the argon scheme before results are shown for the krypton and xenon schemes. The reason for this is that the simpler atomic structure of argon and the smaller number of remaining bound electrons allows for a wider range of simulations to be performed in a reasonable time. The conclusions from argon can then be extended to the other schemes with fewer detailed simulations being required to illustrate the trends. Where there are significant differences between the three gases additional simulations have been performed and the results presented.

Contents

List of figures

List of tables

Chapter 1

Introduction

The optical laser was first demonstrated by Maiman [1] using ruby as the amplifying medium. Following the rapid development using a wide range of media, lasers are now commercially available in wavelengths ranging from the infra red (IR) into the near ultra violet (UV). Extending the operating range of wavelengths into the far UV and X-Ray region of the electromagnetic spectrum has, by comparison, been a much slower process. Two main requirements of generating X-Ray lasers have required a departure from the technology of the solid state or gaseous amplifying media of optical lasers.

The first of these requirements is that of the large energy gap between lasing levels corresponding to X-Ray photons. These energies are typically in the range of 100 to 1000 eV and simply comparing these figures with the binding energies of solids and molecules of a few eV illustrates the impracticality of traditional approaches to the X-Ray region.

The second requirement is the one achieving amplification in a single (or at most two passes) of the medium. Amplifying cavities of the form used for optical lasers cannot be formed since there are no suitable mirrors at these shorter X-Ray wavelengths. Multilayer mirrors are gradually being developed for specific wavelengths but still have reflectivities of at most around 50% at normal incidence. It therefore becomes necessary to look for an amplifying medium with gain coefficients significantly greater than those of optical lasers where these may be as low as 0.001 cm^{-1}.

Both of these requirements lead to the realisation that X-Ray lasers require a much higher energy density amplifying medium than optical lasers and as such, X-Ray lasers typically use plasmas. The technological difficulties of producing suitable plasmas and the understanding of specific processes within them pertinent to X-Ray lasers are still topics of significant research given that a number of important

applications have been identified which are waiting for an economically feasible "table top X-Ray" laser to be developed. This situation is in stark contrast to that surrounding the optical laser of the 1960's which was widely described at the time as "a solution looking for a problem".

A number of potential applications of X-Ray lasers are discussed towards the end of this chapter, before which a review of progress and problems associated with X-Ray lasers and current devices is given.

1.1 Collisionally pumped X-Ray lasers

In these schemes, hot free electrons are used to collisionally excite bound electrons within the ions to states such that a population inversion is formed. There are two main approaches by which the plasma consisting of the lasing ions and pump electrons are created; these are either by ablation and absorption of an optical laser by a solid target or by electrical discharge through a gas. Both these approaches generate a plasma which can be characterised by a thermal plasma, i.e. the plasma species have energies distributed as a Maxwell – Boltzman function of characteristic temperature T_e. A third category of collisionally pumped systems are those that are the topic of this thesis, namely optical field ionisation (OFI) produced plasmas which are characterised by non-Maxwellian energy distributions.

1.1.1 Solid target collisional systems

Since their first demonstration by the Lawrence Livermore National Laboratory (LLNL) in 1984 by Matthews *et al* [2] the collisionally pumped schemes have become one of the most successful methods of regularly producing reproducible and consistent X-Ray lasers. In these schemes, a high power optical laser is incident upon a solid target (or upon both sides of a foil although this is more difficult to achieve experimentally), and firstly ionises the target material to a closed shell configuration (the most successful schemes being to neon and nickel like). Heating of the freed electrons then occurs by inverse bremsstrahlung (IB). Pump energies to target are typically from around 100 Joules to a few kJ with durations of a few to 10s of picoseconds. The high laser powers required currently limit such work to a few

specialist world-class laboratories and considerable work is ongoing in order to reduce these pump energies. The electrons rapidly thermalise through mutual collisions and have average energies of around 800 eV to 1.5 keV. These can then efficiently drive monopole collisional excitations of the outermost bound electron without causing significant further ionisation. Free electron densities of around 10^{19} - 10^{20} cm^{-3} are required to provide significant pumping to the upper laser level.

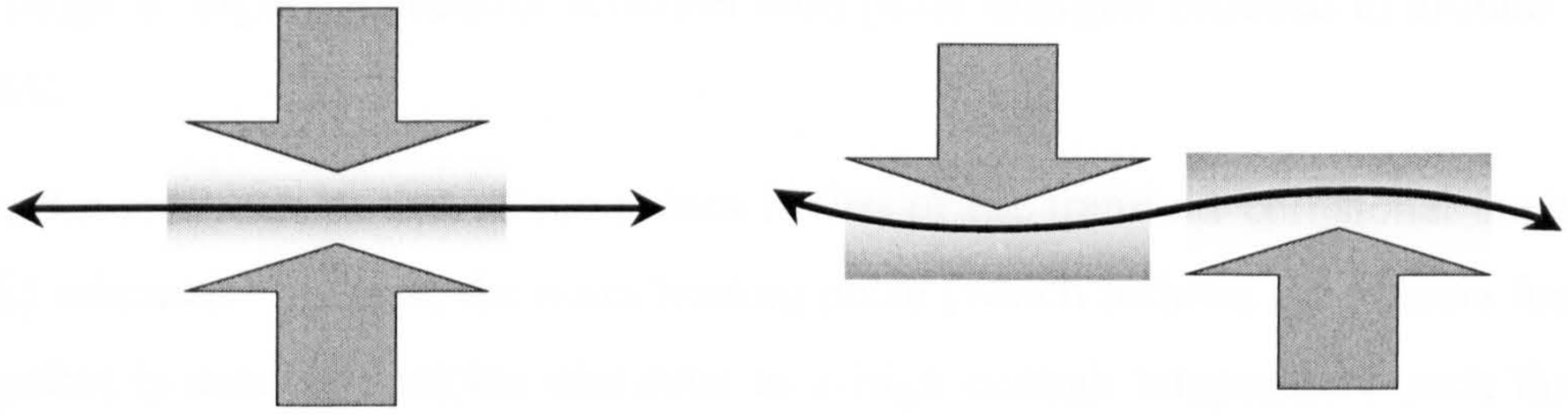

Figure 1.1. Two main geometries for solid target collisionally pumped systems. Left; a foil is irradiated from both sides creating a high density on axis plasma in which an X-ray laser beam is produced and propagates. Right, two targets in which the electron density gradients in one target are compensated for in the next allowing the further amplification of the X-Ray beam.

These relatively simple systems are limited in their efficiency by the creation of large electron density gradients in the plasma which refracts the X-Ray laser away from the denser regions of high gain. They also inhibit coupling of the driving laser energy to the high density inner regions of the plasma. Enhancements to the overall efficiency of the collisional scheme have been made by the use of more ingenious target geometries to counter the refractive effects caused by the electron density gradients. For example, by using two targets illuminated from opposite sides, the X-Ray beam can be made to 'snake' through the opposing density gradients as illustrated in Figure 1.1. This scheme was used by Carillon *et al* [3] to demonstrate the first saturated output of an X-Ray laser. An alternative approach is that of using a toroidially shaped target such that the resulting plasma shape cancels the effect of the density gradients as suggested by Lunney [4] although this is experimentally more difficult to achieve and has not yet been demonstrated. Instead, bent targets offer partial refraction compensation and are now widely used. Simulations of refraction compensation, including the atomic and hydrodynamic effects with plasmas have been extensively modelled by [5] and [6].

A further highly successful method of refraction compensation is to use one or more short pre-pulses of high intensity (~ 10^{14} W/cm^2) and duration ~1 ps to create the plasma of the required ionic species. After a suitable delay in which the plasma expands and the electron density gradients relax, the main pulse of lower intensity (~10^{13} W/cm^2) and duration ~100 ps is applied to heat the electrons. Computational investigations ([7] & [8]) combined with a wealth of experimental work have resulted in a range of highly successful schemes with pulse energies reduced to around 50 to 100 eV.

A similar approach to that of pre pulses is that of the transient collisional excitation (TCE) schemes. In these, the main heating pulse (which follows the plasma forming pre pulse) is used to heat the electrons to a high enough temperature such that the population inversion is formed over time scales short enough that only the upper level is initially populated. This is in contrast to the more usual quasi-static state (QSS) situation where the population of the lasing levels are determined by collisional and radiative transitions involving higher lying levels. As such, larger gains of up to 100 cm^{-1} or more can be established for more modest pump laser energies of the order of 10 Joules. These schemes are expected to self terminate after around 10 ps as the level populations rapidly tend to the thermal equilibrium state destroying the population inversion. Operation of a true TCE X-ray laser has not yet been observed as electron cooling appears to be major limiting factor, however Kalachnikov [9] *et al* have demonstrated lasing in Ne-like Ti at a wavelength of 30.15 nm with a gain of around 35 cm^{-1} for a driving beam energy of only 5J.

Finally, more recent work on travelling wave excitation (TWE) in combination with some of the above approaches, has lead to further significant increases in the efficiency of many of these schemes. Here the basic theory is that the population inversion in the plasma is formed in such a way that it is maximal at exactly the time the X-Ray pulse is propagating through that region of plasma for amplification. This can most readily be achieved by targeting the driving laser onto the target at a 45° angle to the normal such that as seen longitudinally along the target, the driving pulse propagates along it at the velocity of light in step with the X-Ray laser beam. This method can be particularly important given that the lifetime of the population inversion can be less than the transit time of X-ray photons through the plasma. It should also be noted that the X-ray output from TWE methods is uni-directional along

the direction of the travelling pump laser. This is in contrast to that for normal incidence in which X-ray amplification occurs in both directions along the target and may therefore represent a significant loss of the output beam.

The solid target collisionally pumped schemes have proven to be some of the most successful X-ray laser devices with output powers of around 30 MW routinely produced in Ne-like Ge lasing at 19.6 nm. Ni-like schemes offer a more efficient route to shorter wavelengths with saturated lasing observed (refs. [10] and [11]) in Ni-like Dy at a wavelength of 5.86 nm with a gain of 9.2 cm^{-1}.

1.1.2 Electrically discharged collisional systems

If a large electrical discharge is passed through a column of gas, a plasma may be created through collisional ionisation. Ohmic heating of the freed electrons by the current will heat the fomer which can then create a population inversion between bound states of the ions through collisional excitation. This technology is based upon that of the Z-pinch which was widely investigated in the 1960s and 1970s as a method of producing fusion energy. Although these devices have demonstrated lasing at optical wavelengths, scaling to shorter wavelengths requires highly charged ions which in turn need currents of many tens of kA. This creates problems in controlling the resulting plasma column since instabilities in the collapsing column rapidly destroy the uniform plasma needed for X-ray amplification.

Instabilities can be minimised by using driving currents with very fast rise times (so called fast capillary discharges). Rocca *et al* [12] and [13] have demonstrated lasing in Ne-like argon (the same lasing scheme investigated for argon in this work) using currents of ~40 kA with a 10% to 90% rise time of 10 ns. This produced a stable plasma column of up to 12 cm of radius 4 mm in which lasing at 46.9 nm with a gain of around 0.6 cm^{-1} was observed. This value of the gain is low compared with those generally encountered in collisional systems due to the lower electron temperature of around 60 to 80 eV which results in only weak excitation of the upper laser level.

Scaling to still shorter wavelengths requires much higher electron temperatures which again gives rise to problems of plasma stability. Additional work by Gonzalez *et al* [14] has demonstrated hotter stable plasmas of temperatures around 300 eV in argon

using currents of 200 kA which is still considerably below the ~1 keV temperatures needed to effectively generate hard X-rays. Furthermore, given the need for a gaseous material (or a solid which can be easily vaporised such as that demonstrated by Tomasel *et al* [15] in sulphur lasing at 60.8 nm) it is likely that practical discharge systems will be restricted to the extreme ultra violet (X-UV) regime.

1.1.3 Optically field ionised collisionally pumped systems

An intense laser field can have an associated electric field sufficiently strong enough to suppress the potential barrier of an atom and may release bound electrons thus creating a plasma. For a laser of relatively long wavelength (0.8 to 1.0 μm) which is circularly polarised the freed electrons may have energies in the keV range and are thereby suitable for collisionally exciting ions within the plasma. Since electrons are released through a direct interaction of the laser with the atomic electrons, the target material must generally be gaseous. As a consequence of the necessarily lower than solid densities and the lack of ablative and collisional heating effects of the previously discussed collisional schemes, the driving pulse energies for these OFI collisional schemes are reduced to the mJ range. (A complete discussion of the OFI collisionally pumped theory and references therein, is given in the following chapter.)

These schemes are practically interesting given that typical driving lasers (such as the Titanium Sapphire at 800 nm) have repetition rates of many 10s of Hz and pulse energies of several Joules. This in conjunction with a "non-destructive" gaseous target may finally allow for the realisation of "table top" X-ray lasers, although at present the available driving pulse energies strictly restrict the operating range to the X-UV.

Schemes lasing at 46.9, 31.1 and 41.8 nm in argon, krypton and xenon respectively were proposed by Lemoff *et al* [16] in 1994 and sparked considerable experimental interest with little real success. Lemoff *et al* [17] reported a gain of 13.3 ± 0.9 cm^{-1} at an atomic density of 4.6×10^{17} cm^{-3} in xenon for a pulse energy of 70 mJ. This is contrast to their predictions [16] of 164 cm^{-1}. Later work by Mocek *et al* [18] on each of these gases showed that the required ion could be created with pulse energies around 150 mJ but saw no evidence of lasing.

Reproducible lasing has now been produced by Balcou *et al* [19] for xenon at a density of 5.8×10^{17} cm^3 with a measured gain of 67 cm^{-1} which was achieved using a driving pulse energy of some 350 mJ. More recently, the same group [20] has observed lasing in the krypton system with a gain of 78 cm^{-1}. These results are discussed more fully later in this work in the light of the modelling work presented. Finally, Lu *et al* [21] proposed a scheme based on sulphur lasing at 60.8 nm which predicted modest gains in region of 15 to 30 cm^{-1}, however given the difficulties in handling sulphur it is unlikely such a scheme will be demonstrated given the ease with which the noble gases can be handled.

Hooker *et al* [22] presented calculations in Be-like ions and showed that lasing could be expected at shorter wavelengths for transitions involving a change in the principle quantum number ($\Delta n \neq 0$). Predictions were made for neon lasing at 14.1 nm, nitrogen at 46.8 nm and aluminium at 6.78 nm.

The main difficulties with this OFI scheme are involved with the relatively long wavelength of the driving laser and pumping the system itself. Unlike the solid target systems, the beam needs to be driven longitudinally into the gas for many mm in order to create a significant length of the amplifying plasma which creates considerable problems of refraction. Refraction of the driving beam for recombination schemes has been considered by Decker *et al* [23]. In addition, the OFI process creates a plasma which is strongly non-thermal in nature which may have considerable consequences for the models which predict high gains on the basis of QSS calculations based on a characteristic thermal temperature.

1.2 Recombination X-Ray Lasers

The recombination laser operates when free electrons recombine with a stripped ion. Recombination occurs preferentially to the upper states of the ion provided that the electrons are cold and a population inversion may therefore be formed as electrons cascade through to lower energy states. This scheme was first proposed by Gudzenko *et al* [24] in 1965 for lasing at optical wavelengths and was later extended to the X-ray region by Pert and Ramsden [25]. Transitions in moderate Z elements of the Lyman or Balmer series of H-like, Li-like or Na-like will give rise X-ray wavelength

emission. Recombination lasers are self terminating since there is no way of re-establishing the population inversion.

There are two main methods of creating the high density cold plasmas needed. The first is that of focusing an optical laser onto a solid target which then expands and cools adiabatically. The second is through OFI of a gas.

1.2.1 Adiabatically cooled recombination lasers

In this scheme a high power optical laser, typically of a few ns in duration, is focussed onto a solid target which is ionised to a stripped or closed shell configuration. The electrons of the resulting plasma are hot and are cooled through adiabatic expansion. Recombination is a three body process, requiring two electrons to be in the vicinity of the ion at the same time. One will recombine with the ion and the second will carry away the excess energy. This means that a high electron density is required which is not easily achieved in combination with the low electron temperature. For this reason development of these schemes has proven to be difficult and although lasing has been observed, saturated output has not yet been achieved.

The first experimental observation of recombination lasing at X-ray wavelengths was in a H-like carbon plasma on the $n = 3 \rightarrow 2$ transition at 18.2 nm by a thin fibre of diameter ~ 7 μm [26]. Typical gain length products produced are around 2 – 4 with the shortest reported wavelength of 5.4 nm in H-like sodium [27].

Increasing the power to target to a few 10^{15} W/cm^2 in sub ps timescales results in a plasma whose outer layers are rapidly blown off, effectively taking heat from the denser remaining core. This so called exploding target technique has reduced the optical laser powers needed to the region of 10 to 20 J and produced slightly larger gain lengths of around 6 in H-like carbon at 18.2 nm [28] and Na-like copper at 11.1 nm [29].

Considerable difficulties are encountered in fabricating suitable targets for these types of schemes and the inability to demonstrate saturated output has meant that these systems are now largely ignored in favour of the much more robust and successful collisional schemes.

1.2.2 OFI Recombination lasers

Optical field ionisation can produce a plasma whose mean electron temperature is significantly smaller than the ionisation potential of the ions. By using a short wavelength driving laser, typically 248 nm, which is linearly polarised, the electrons released by OFI can have energies of only a few eV. Since the resulting plasma is already cold, recombination should occur without the cooling phase of the adiabatically cooled systems. To date experimental observation of lasing in such systems has only been reported in H-like lithium at 13.5 nm [30], [31] and in Li-like aluminium at 15.5 nm and 10.6 nm [32].

A comprehensive theoretical study of these schemes was conducted by Grout [33] who concluded that considerable gain should be achievable in argon and nitrogen targets that are doped with hydrogen. The hydrogen doping will enable higher electron densities to be achieved than with pure targets and would act as a source of cold electrons. As yet there is no published evidence of these schemes having been observed which may be due to the low saturated irradiances (predicted to be of at most 10^7 W/cm^2) making detection difficult.

1.3 Inner shell photo-ionisation

Scaling X-ray lasers to wavelengths of less than around 2 nm requires inner shell ionisation which is not easily achieved by electron collisions before ionisation of the valence electrons. An alternative is that of photo-pumping. Here, a high Z 'flash lamp' material is irradiated with an ultra short laser pulse. The resulting plasma is a source of incoherent X-rays, the high energy photons of which are allowed to pass through a filter onto the target. Inner shell ionisation preferentially occurs and the hole is filled by an inner shell transition. Healy *et al* [34] modelled a scheme lasing at 1.5 nm although the short gain duration of 50 fs requires extremely precise travelling wave pumping. This scheme has not been observed experimentally. Inner shell photo-pumped lasing was first observed at optical wavelengths in 1998 [35] with shortest wavelength demonstrated so far being 91 nm in Kr III (Refs [36] and [37]).

1.4 High harmonic generation

The generation of high harmonic radiation (HHG) is realised using an experimental configuration which is very similar to that used in OFI experiments. A femtosecond, high intensity optical laser is focused onto target and electrons are released through OFI. As the electric field in the laser changes sign, electrons may be driven back towards the ion and recombine to the ground state emitting any energy gained as photons. The output is characterised by a broad plateau of nearly constant intensity across many times the frequency of the driving laser, with a sharp cut off which represents the maximum kinetic energy gained by the electrons from the laser. Detailed theory of HHG is given by L'Huillier *et al* [38].

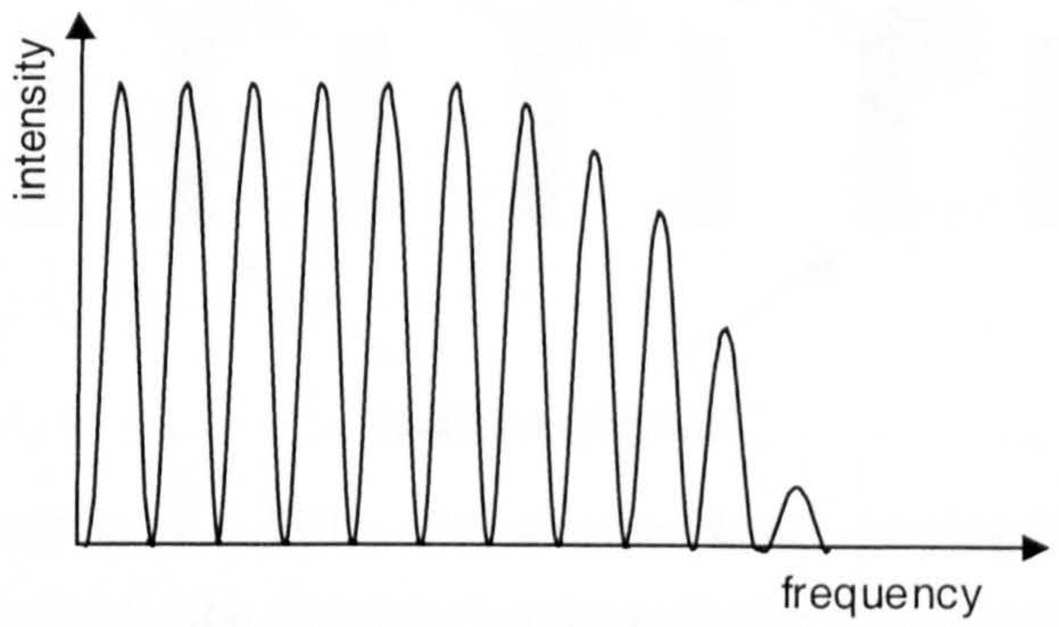

Figure 1.2. Schematic of a HHG spectrum illustrating the regular and discrete structure of the output up to a maximum cut off frequency.

Using a Ti:sapphire laser of wavelength 780 nm, the 131st harmonics have been observed in neon (5.99 nm) [39], 91st in argon (9.7 nm) [39] and the 9th in xenon clusters (86.7 nm) [40]. This work on xenon suggests that yield from these systems could be increased by several orders of magnitude by using clusters of atoms. The shortest reported wavelength of 6.7 nm was obtained using a KrF laser at 248 nm, representing the 37th harmonic [41]. The 67th harmonic of a 1.053 μm (15.7 nm) CPA laser focused onto a plastic target has also been observed [42].

A considerable disadvantage to this scheme is the short pulse duration (around 50 fs) and large linewidth of around 1 nm which restricts the potential applications to those not requiring high spectral resolution. The output intensities are also two to three orders of magnitude lower than those attainable from collisional systems.

1.5 Free electron lasers

The free electron laser (FEL) involves a fundamentally different approach to the generation of coherent radiation from the techniques discussed so far in that it uses a relativistic electron beam as the lasing medium as apposed to bound atomic / ionic states and was first proposed by Madley in 1971 [43]. It has the potential to offer tuneable lasing from the microwave to X-ray regions by the simple method of altering the electron beam energy.

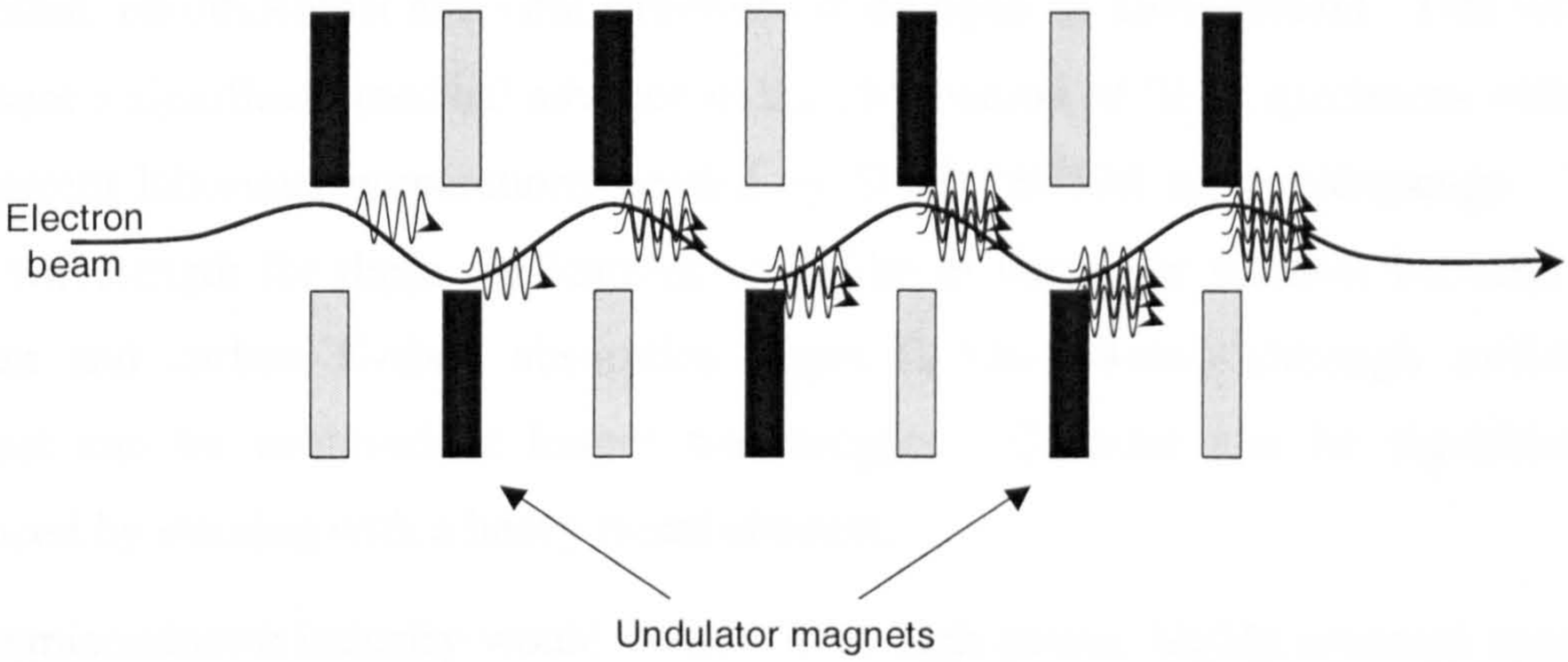

Figure 1.3. Schematic of a FEL. An electron beam passing through alternating transverse magnetic fields (the undulator) emits radiation which can interact resonantly with the beam and result in coherent output. At wavelengths up to the UV, the entire structure may be contained in a resonant cavity.

Lasing in the FEL occurs through an interaction between the emitted radiation and different energy groups of electrons. Electrons moving slightly slower than the average, will tend to absorb the radiation in a process analogous to stimulated emission. Once a significant radiation field has been been established, about half the electrons will gain energy and hence move faster while the other half loose energy and move slower. Thus the electron beam begins to bunch up on the scale of the radiation wavelength. The radiation emission rate scales as the square of the number of electrons for a bunched group as opposed to linearly with the number of electrons for an unbunched group and hence amplification of the radiation occurs. A large number of devices currently operate a wavelengths down to around 100 nm [44].

Scaling to shorter X-UV and hard X-ray wavelengths is more of an engineering problem than physical. The GeV electron energies needed can only be produced by linear accelerators of 100's of metres in length and hence represent a considerable

capital cost. A number of devices around the world are currently planned or nearing completion and should begin operating at wavelengths of less than 5 nm within one or two years.

1.6 Applications of X-ray lasers

One of the most widely reported uses of X-ray lasers would be in biological imaging of protein, chromosomal and viral structures in an aqueous environment. This would represent a significant medical advance in the observation of 'live' specimens without the current laborious preparations needed by SEM / STEM type microscopy. The ideal wavelength for these applications would be in the water window between the oxygen and carbon K-shell absorption edges (2.3 to 4.4 nm) although sufficient contrast can be achieved at longer wavelengths. Contrast can be significantly enhanced by staining with a heavy metal element.

The semiconductor industry would benefit from high power, highly coherent sources as means of creating more detailed photolithography masks and thereby increasing the density of components on integrated circuit chips. Current technology has pushed component sizes down to as small as around 0.1 μm using electron etching techniques although such technology is limited in its resolution by the use of an electrically charged beam.

Plasma diagnostics using X-ray lasers are now widely used, particularly as the large scale facilities needed to generate the laser are often the same used in the experiments themselves. A recent example is that of Takahashi *et al* [45] who used a Ne-like Ge x-ray laser at 19.6 nm to probe the plasma formed in so called hole drilling experiments of interest to the fast ignitor inertial confinement fusion systems.

Chapter 2

Theory of OFI collisionally pumped X-ray lasers

2.1 Introduction

The results presented and discussed in this thesis have been made with a number of simulation codes which model physical processes pertinent to the generation of X-Ray lasers in gaseous targets following optical field ionisation. It is therefore necessary to present a detailed description of the theory behind the important physical processes.

2.2 Optical field ionisation

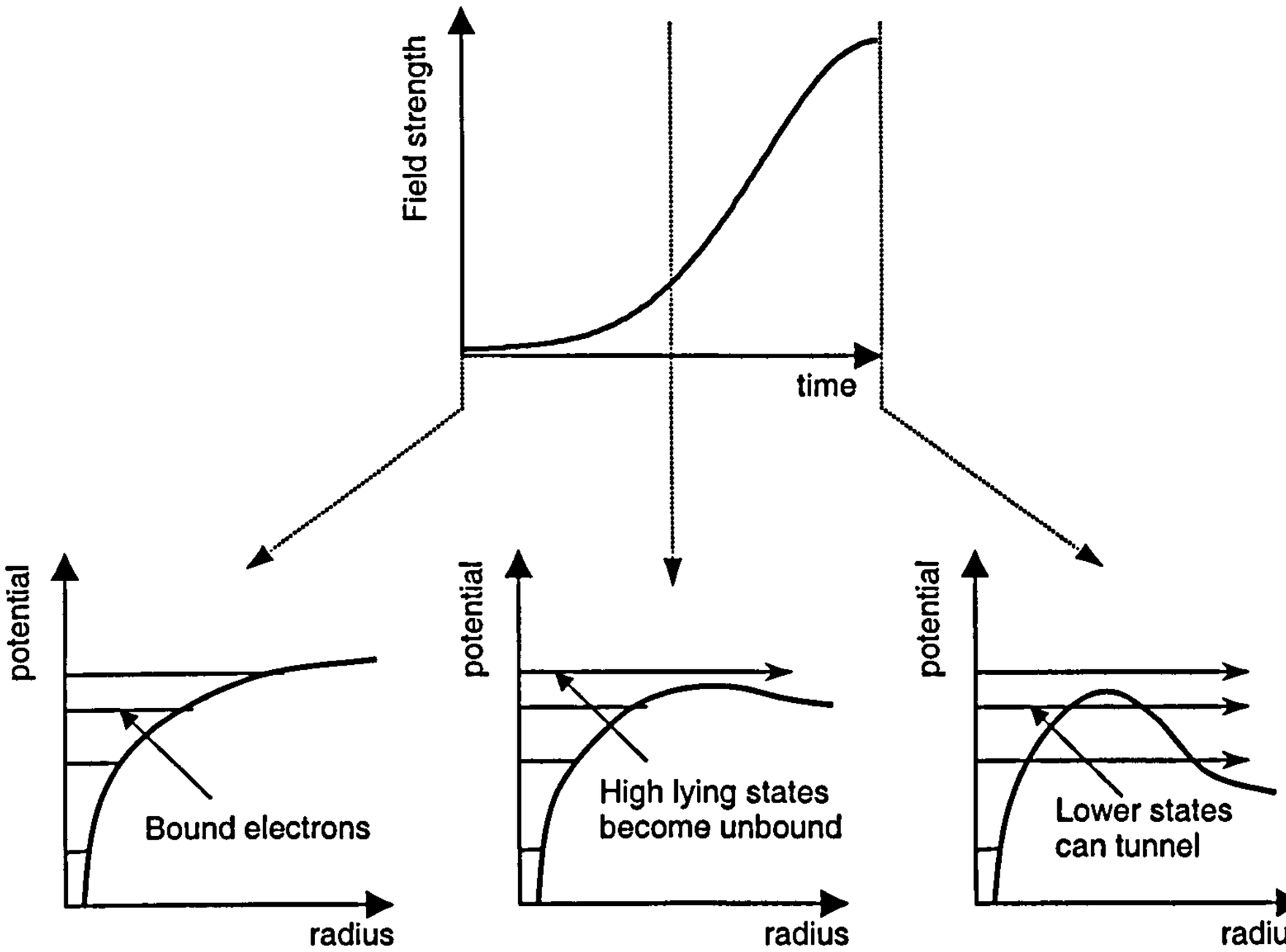

Figure 2.1. The Coulomb potential barrier within an atom (bottom three diagrams) is suppressed in the presence of an electric field which may vary with time (top). As the field strength increases, bound electrons may become completely unbound (bottom centre) or be able to tunnel through the reduced barrier (bottom right).

If an electric field applied to an atom is strong enough it can suppress the Coulomb potential barrier, releasing electrons and resulting in ionisation. This is shown in Figure 2.1. An electromagnetic wave of intensity I W/m^2 (although practically and throughout this thesis, units of W/cm^2 are generally used) has a related peak electric field of;

$$E_0 = \sqrt{2I / \varepsilon_0 c} \tag{2.1}$$

A simple expression can be obtained for the irradiance required to completely suppress the potential binding and electron with ionisation energy ε_i from an atom of atomic number Z giving [46]

$$I_{th} = \frac{\varepsilon_i^4 \varepsilon_0 c}{128\pi Z^2 e^5} \tag{2.2}$$

This allows an estimate to be made of the intensities required to create ionic species of interest to X-Ray laser schemes and shows that intensities typically greater than 10^{15} W/cm^2 are needed. Such intensities are at present only feasibly produced by optical lasers in which the available energy is compressed to sub picosecond time scales. While equation (2.2) is a useful starting point, it is only valid for static fields and not the oscillating fields present in the electromagnetic fields of laser radiation and thus a more detailed theory is required. For an oscillating field the level of barrier suppression is variable and two regimes may be identified leading to different functional relations for the ionisation rate. The first of these is the tunnelling regime in which the 'time of flight' of the electron through the barrier is small in comparison to the field oscillation period in which case the field can be treated as quasi-static. If this is not the case ionisation occurs as a multiphoton process. For the conditions used examined in this thesis, multiphoton ionisation (MPI) was found not to be important. A quantitative distinction between the two is given by the Keldysh parameter [47];

$$\gamma = \frac{\omega\sqrt{2m_e\varepsilon_i}}{eE_0} \tag{2.3}$$

where ω and λ are the laser angular frequency and wavelengths respectively and E_0 is the electric field. This is the square root of the ratio of kinetic energy gained due to the motion of the electron in the oscillating field to the ionisation energy. The tunnelling regime is expected to be strictly valid for $\gamma << 1$ although experimental work by Augst *et al* [48] on the ionisation of noble gases by a CO_2 laser of wavelength 1.053μm and pulse length ~1 ps operating in the range $0.1 < \gamma < 1.0$ confirmed the wider applicability

of tunnelling calculations in this regime. For the laser parameters typically used in this work for a wavelength of 800 nm, peak irradiance of 10^{17} W/cm^2 and a typical ionisation potential of 150 eV, $\gamma \approx 0.1$ and thus MPI is not considered in this work, particularly given the experimental validation of the tunnelling theory to gases of interest here by Augst *et al* [48].

For the tunnelling ionisation regime the ionisation rate in a static field E_0 was derived by Smirnov and Chebisov [49] and subsequently corrected by Perelomov *et al* [50];

$$P_0 = \frac{\omega_{au}}{2} C^2_{n^*,l} \frac{\varepsilon_i}{\varepsilon_h} \frac{(2l+1)(l+|m|)!}{2^{|m|}|m|!(l-|m|)!} \left[2\left(\frac{\varepsilon_i}{\varepsilon_h}\right)^{3/2} \frac{E_{au}}{E_0} \right]^{(2n^*-|m|-1)} \times \exp(-\alpha) \qquad (2.4)$$

Here $\omega_{au} = m_e e^4/\hbar^3$ and $E_{au} = e^5 m_e^2/64\pi^3\varepsilon_0^3\hbar^4$ are the atomic frequency and field strengths respectively, ε_h is the ionisation energy of hydrogen, $C_{n^*,l}$ is a wavefunction matching coefficient, l and m are the angular and magnetic quantum numbers of the state and n^* is the effective principle quantum number;

$$n^* = Z\sqrt{\frac{\varepsilon_h}{\varepsilon_i}} \qquad (2.5)$$

For the hydrogen ground state $C_{1,0} = 2$ while for n^* sufficiently large that the quasi-classical approximation can be used, Ammosov *et al* [51] gives;

$$C_{n^*,l} \approx \left(\frac{2e}{n^*}\right)^{n^*} (2\pi n^*)^{-1/2} \qquad (2.6)$$

The exponential factor α in equation (2.4);

$$\alpha = \frac{2}{3}\left(\frac{\varepsilon_i}{\varepsilon_h}\right)^{3/2} \frac{E_{au}}{E_0} \qquad (2.7)$$

Applying equation (2.4) to the case where the field is oscillatory with an instantaneous strength E gives the ionisation rate per unit time;

$$P(E) = P_0\left(\frac{E_0}{E}\right)^{2n^*-|m|-1} \exp\left[\alpha\left(1-\frac{E_0}{E}\right)\right] \qquad (2.8)$$

At this stage, it becomes necessary to consider the polarisation of the laser field and corresponding electric field. The polarisation parameter, ϕ ($\phi \in \Re(0,1)$), is defined as

the fraction of irradiance in one polarisation, e.g. **x**, which is $\pi/2$ out of phase with that in the orthogonal direction, **y**. From equation (2.1) then if the peak fields are given by;

$$E_{0x} = \sqrt{\frac{2I\phi}{\varepsilon_0 c}} \quad \& \quad E_{0y} = \sqrt{\frac{2I(1-\phi)}{\varepsilon_0 c}} \tag{2.9}$$

then the electric field may be described by a vector;

$$\mathbf{E} = E_{0x}\cos(\omega t)\cdot\mathbf{x} + E_{0x}\sin(\omega t)\cdot\mathbf{y} \tag{2.10}$$

The total magnitude of the electric field at any time is then given by;

$$E(t) = E_0\sqrt{\tfrac{1}{2} + \left(\phi - \tfrac{1}{2}\right)\cos(2\omega t)} \tag{2.11}$$

Linearly polarised fields ($\phi = 0$) are not considered in this thesis (for reasons illustrated shortly) while elliptical ($\phi \neq 0, ½$) and circular ($\phi = ½$) cases are. However, it is instructive to consider the effect of the linear polarisation as one limiting case in addition to the circular case as the other. The cycle averaged ionisation probability per unit time is given by;

$$\overline{p} = \begin{cases} \dfrac{2}{\pi} P_0 e^{\alpha} \dfrac{d^{\left[2n^*-|m|-2\right]}}{d\alpha^{\left[2n^*-|m|-2\right]}} K_0(\alpha) & \phi = 0 \\ 2^{\left(2n^*-\frac{1}{2}|m|-\frac{1}{2}\right)} P_0 \exp\left[\alpha\left(1-\sqrt{2}\right)\right] & \phi = \frac{1}{2} \end{cases} \tag{2.12}$$

$K_0(\alpha)$ is a modified Bessel function of order zero. These results have been obtained by many workers ([52], [53] and [54]), while the work of Delone and Krainov [55] who produced results via a quasi-classical quantum mechanical approach showed that these results are equivalent for the conditions examined in this thesis. No analytic expression for the total ionisation probability for elliptically polarised light exists, but it can be obtained by numerical integration over the appropriate probability function as given in Pert [53]

$$p(\varepsilon)d\varepsilon = \frac{P_0\left(\varepsilon_q/(\varepsilon_q-\varepsilon)\right)^{\left(n^*-\frac{1}{2}|m|-\frac{1}{2}\right)}\exp\left[\alpha\left(1-\sqrt{\varepsilon_q/(\varepsilon_q-\varepsilon)}\right)\right]}{\pi\sqrt{\left[\left(\phi-\frac{1}{2}\right)^2-\left(\frac{1}{2}-\varepsilon/\varepsilon_q\right)^2\right]}}\frac{d\varepsilon}{\varepsilon} \tag{2.13}$$

The key difference between the two total ionisation probabilities given by (2.12) is that the power of the exponent in α is positive for the linear polarisation case and is negative for the circular case. Thus, the ionisation probability is smaller in the circular case. This is as expected given that the electric field amplitude E from (2.11) is smaller than

for the linear case although the field is always non-zero for the circular case and hence the atom is subject to ionisation for longer periods of time.

It should be stated that if the applied electric field becomes strong enough to completely suppress the Coulomb barrier below that binding an electron then the electron becomes unbound and tunnelling theory no longer applies. For realistic cases (and those considered in this thesis) in which the applied field has a finite rise time this in unlikely given the progressive increase of the field strength from zero.

2.3 Above threshold ionisation heating

Once an electron is released through the OFI process, it can then gain energy from the electric field. The classical picture used is that of Corkum *et al* [56] which assumes that at the instance of release the electron is at rest. The total (zero) velocity is then the sum of two components: the thermal and quiver velocities. The latter is the response of the electron to the oscillating electric field. Assuming the field changes sufficiently slowly then the quiver velocity will change adiabatically without changing the thermal component. At the end of the pulse the electron will therefore be left with the quiver velocity at the moment of ionisation. By considering the velocity of an electron in response to the electric field given by equation (2.10) then it can be shown that;

$$\varepsilon(t) = \frac{e^2 E_0^2}{2m_e\omega^2}\left[\phi\cos^2(\omega t) + (1-\phi)\sin^2(\omega t)\right] \tag{2.14}$$

Again taking the two limiting cases of linear and circular polarisation;

$$\varepsilon(t) = \begin{cases} \dfrac{e^2 E_0^2}{2m_e\omega^2}\sin^2(\omega t) & \phi = 0 \\ \dfrac{e^2 E_0^2}{4m_e\omega^2} & \phi = \frac{1}{2} \end{cases} \tag{2.15}$$

Equation (2.15) allows the major difference between linearly and circularly polarisation produced electrons to be seen, namely that those from linearly polarised light are produced with a range of energies over the period of the field. Since the electric field is a maximum at the peak of the field cycle when $\omega t = 0$, from (2.8) (where E_0 should be replaced by $E(t)$) it is seen that more electrons are released with zero energy than for the maximum which occurs when $\sin^2(\omega t) = 1$ which occurs at the minimum of the cycle when the field is zero. The energy of electrons can therefore be considered in terms of

the phase mismatch between the time of release and the peak of the field. This is illustrated in Figure 2.2.

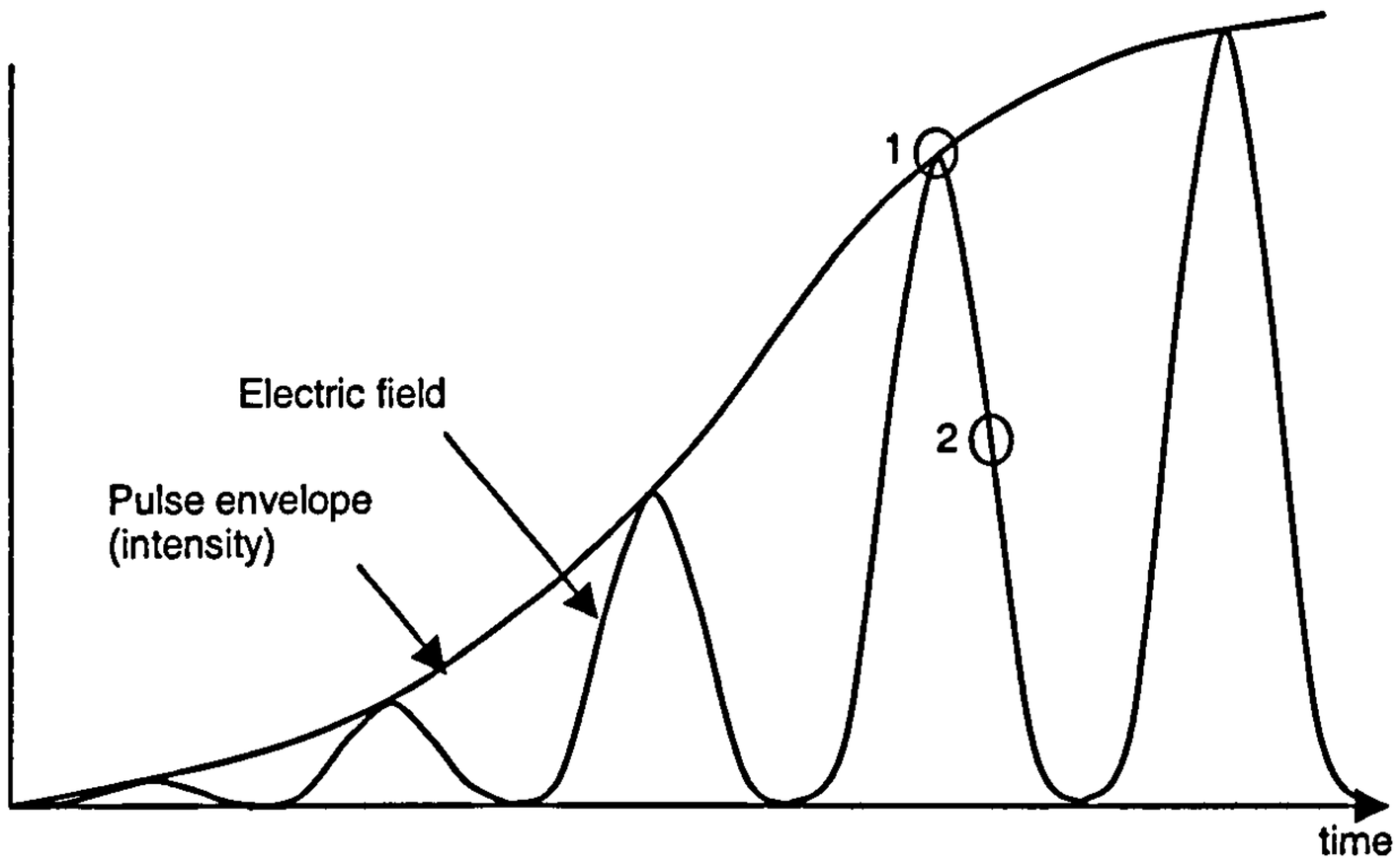

Figure 2.2. The pulse envelope function (the irradiance) and associated oscillating electric field for the case of linear polarisation. More electrons are released at the peaks of the field (points like 1) than elsewhere (like 2). Since the energy of the freed electrons is proportional to this phase mismatch, the mean energy is much less than the maximum.

For the case of circular polarisation however, the total amplitude of the electric field over a cycle (considering that the overall amplitude is approximately constant over the cycle period) is at all times the same. There can be no phase dependence on the energy gain of electrons and hence they gain the same energy.

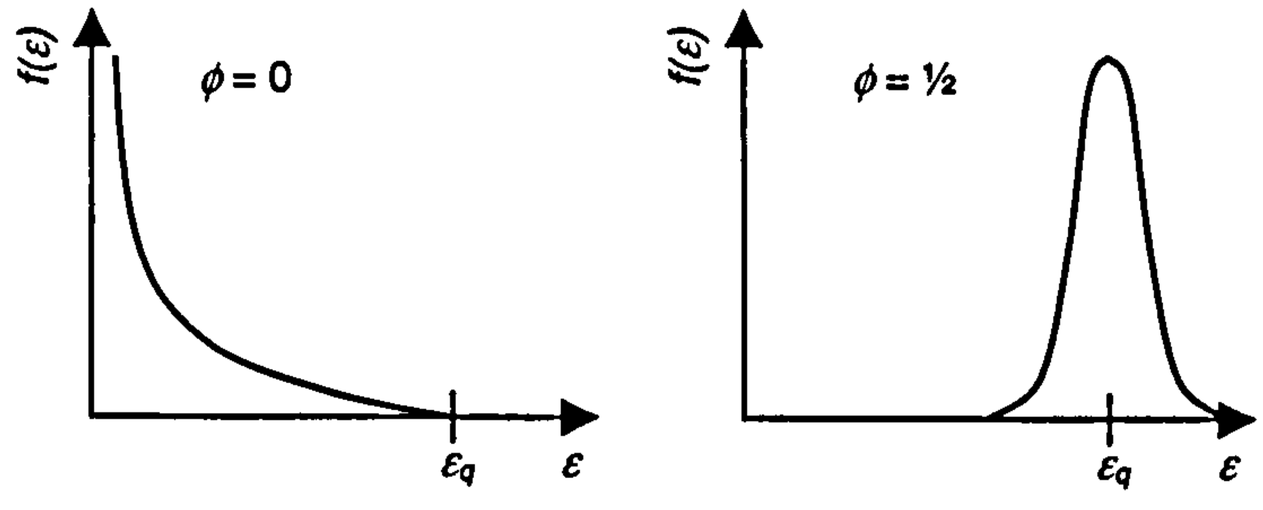

Figure 2.3. ATI energy distributions for the cases of linear and circular polarised fields in terms of the quiver energy ε_q.

The clear difference between the two cases is shown in Figure 2.3 where the energy ε is expressed in terms of the quiver energy $\varepsilon_q = e^2 E(t)^2 / 2m_e\omega^2$. Clearly, the mean energy for the case of a circularly polarised field is equal to ε_q while for the linear case it must be obtained by integrating over the ionisation rate at each part of the field cycle giving;

$$\bar{\varepsilon}_q \approx \left[\frac{3}{2}\left(\frac{\varepsilon_h}{\varepsilon_i}\right)^{3/2}\frac{E_0}{E_{au}}\right]\varepsilon_q \tag{2.16}$$

Given the relative magnitudes of ε_i to ε_h and E_0 to E_{au} it is clear that the mean in this case is much less than the quiver energy. Linearly polarised fields are therefore used in systems such as recombination X-Ray laser schemes where cold electrons are needed while circularly polarised fields produces hot electrons centred about the quiver velocity and are applicable for the collisional systems of interest to this thesis. The general case of elliptical polarisation occupies an intermediate parameter space and thus allows the possibility (in combination with other laser pulse parameters such as wavelength and duration) of matching the peak of the electron distribution to the optimal temperature for pumping the required population inversion.

2.3.1 Relativistic effects

The OFI and ATI processes detailed above are entirely non-relativistic in nature and are usually justified for X-Ray laser calculations given that relativistic effects are not expected to be significant for laser intensities of less than 10^{18} W/cm^2. Smirnov and Krainov [57] extended these results for relativistic effects of atoms under linearly polarised fields and confirmed that the tunnelling of relativistic electrons is very small, justifying the treatment in early works on recombination laser schemes. This is certainly not the case for circularly polarised fields as examined in the work of Krainov [58]. This shows that the peak of the energy distribution is shifted from classical predictions by a factor of;

$$f_{rel} = \sqrt{1+\left(\frac{eE_0}{2m_e\omega c}\right)^2} = \sqrt{1+\frac{e^2\lambda^2 I}{8\pi m_e^2 c^5 \varepsilon_0}} \tag{2.17}$$

The main point to note from (2.17) is its dependence upon the wavelength λ of the radiation. The electron energy from ATI scales as λ^2 and hence for the collisional schemes a longer wavelength is desirable. For the purposes of this thesis where driving by a titanium sapphire (Ti:S) laser is considered at 800 nm with an irradiance of at least 10^{17} W/cm^2 this means that the energy distribution is shifted by some 2% from the classically calculated values. For the bulk of the simulation work presented in this

thesis which assumes thermal Maxwell-Boltzmann distributions, this is not significant. For the work on electron energy distributions with the Fokker-Planck calculations, this becomes more questionable, particularly as it will be shown that an irradiance of 10^{17} W/cm^2 must be considered an absolute minimum for the argon scheme.

2.4 Inverse bremsstrahlung heating

If an oscillating electron in an electric field undergoes an elastic collision with an ion then the direction of motion will be altered and thus a portion of the quiver energy will be transferred into random thermal motion. Hence electrons that are being driven by a laser field in a plasma will absorb energy from the electromagnetic field. This process is known as inverse bremsstrahlung (IB) or collisional heating. It can be viewed as the reverse process to the more familiar bremsstrahlung emission of radiation in that the electron absorbs photons in the presence of an ion with which to conserve angular momentum.

The rate of electron energy absorption from an EM field can be determined from the 'impact approximation' in which absorption is calculated from the momentum transfer cross section, σ_d

$$\sigma_d = 4\pi b_{\min}^2 \ln\left(\left[1+\left(\frac{b_{\max}}{b_{\min}}\right)^2\right]^{1/2}\right) \tag{2.18}$$

The impact parameters b_{min} and b_{max} represent the radius of approach to an ion of the electron necessary to deflect it by 90° and the smallest radius such that it remains undeflected respectively. The correct choice for the inner impact parameter used in the logarithmic term is given by the larger of the Landau parameter Ze^2 / mv^2 for classical collisions or the electron wavelength h / mv (where h is Planck's constant) for quantum mechanical collisions. In the absence of any EM wave then b_{max} is equal to the Debye length of the plasma thus representing the bulk screening effects. In the presence of an EM wave of angular frequency ω then $b_{max} \approx v / \omega$. For large fields this distance may exceed the Debye length as the electron velocity will be given by the quiver velocity

$$v_q = \frac{eE}{m_e\omega} = \sqrt{\frac{2\varepsilon_q}{m_e}} \tag{2.19}$$

For large fields then the electron velocity will generally lie in the range

$$v_T \leq v \leq v_q \tag{2.20}$$

where v_T is the thermal velocity of the electrons.

The impact approximation is valid when the scattering time is short compared to the period of the EM wave and hence for long wavelengths. For classical collisions, Pert [59] gives the momentum transfer cross section as

$$\sigma_d = 2\pi\left[\frac{Ze^2}{m_e}\right]^2 \frac{1}{v^4}\ln\left[1+\frac{v^6}{\left(Ze^2\omega/m_e\right)^2}\right] \tag{2.21}$$

Even though the pulse may be short it will encompass many periods of the wave and since the collisions occur on a time less than the wave period over distances which vary through the changing quiver velocity then the electrons undergo many long range small angle collisions. The momentum cross section must therefore by integrated over the pulse field and the thermal distribution. Doing so gives the rate of energy gain from [59] as

$$\overline{R} = 4m_e n_i\left[\frac{Ze^2}{m_e}\right]^2 \frac{1}{v_q}\ln\left(\overline{\Delta}\right)\left[\tfrac{1}{2}\ln(4x)+\left(\tfrac{\gamma}{2}+\ln 2-1\right)\right] \tag{2.22}$$

where n_i is the ion density, $\gamma \approx 0.577$ is Euler's constant, x is the ratio of quiver energy to thermal,

$$x = \frac{m_e v_q^2}{2k_B T_e} \tag{2.23}$$

and

$$\overline{\Delta} = \frac{\left(\frac{2k_B T_e}{m_e}\right)^3}{\left(\frac{Ze^2\omega}{m_e}\right)^2} \tag{2.24}$$

The rate of (2.22) agrees with that obtained by Polishchuk *et al* [60] derived from alternative considerations. This is strictly valid only for a linearly polarised field. For general polarisation, the detailed forms given by Pert [59] should be used.

A complete derivation and evaluation of the heating rate as applicable to OFI created plasmas suitable for recombination schemes is given by Pert in [53]. He concluded that IB heating can be significant for the parameters necessary for recombination and that it

could increase the ATI temperature by a few eV and thus lead to problems for recombination.

Moving to the much longer wavelengths needed for the collisional schemes produces a reduction in the heating rate which rapidly becomes insignificant compared to the ATI temperature. Only at ion densities at greater than around 10^{19} cm^{-3} is IB heating likely to be significant.

2.5 Plasma effects

It is necessary to present a brief overview of some aspects of plasma theory, particularly in respect of electron – ion thermalisation. It must be stated here that much of the work presented in this section is only strictly applicable to thermalised Maxwellian temperature distributions. Although these clearly do not apply to OFI produced plasmas they provide an important insight into the general behaviour of the plasma. Furthermore, many of the atomic processes later examined perform calculations based on thermal distributions; indeed many of these calculations would be prohibitively expensive if done by other means on the facilities available. Later work in this thesis attempts to address some of these problems by using the true electron energy distribution and theory pertinent to this, which supersedes that here, is presented shortly.

Much of the work presented here is summarised from the thesis of Grout [33].

2.5.1 Equations of state

The hydrodynamics of a laser produced plasma are due to the ion and electron pressures. The ideal gas equations of state including ionisation give the pressures as [61];

$$\begin{aligned} P_e &= n_e(\gamma_e - 1)\varepsilon_e \\ P_i &= n_i(\gamma_i - 1)\varepsilon_i \end{aligned} \tag{2.25}$$

for electron / ion densities $n_{e/i}$, energies $\varepsilon_{e/i}$ and the ratio of specific heats $\gamma_{e/i} = {}^5/_3$.

In assuming Maxwellian energy distributions then the temperature of the two species is given by

$$kT_{e/i} = \tfrac{2}{3}\varepsilon_{e/i} \tag{2.26}$$

The electron and ion densities are related by

$$n_e = Z^* n_i \tag{2.27}$$

where Z^* is the mean fractional ion charge.

The hydrodynamic expansion of OFI plasmas is a small effect for those examined in this thesis. Although this thesis examines the use of circularly polarised light and hence hot plasmas, the densities are still low enough that this is of negligible effect. Experiments and simulations by Dunne *et al* [62], although for linearly polarised light intended for study in recombination schemes, showed that significant expansion in these regimes takes many hundreds of picoseconds. Even adjusting for the hot electrons and higher densities considered here by reducing this by one or two orders of magnitude, then this is still insignificant compared to the gain lifetime.

2.5.2 Electron – ion thermalisation

The distinct plasma species are characterised by their individual behaviours as described by the above equations of state. Interactions between the electrons and ions results in energy exchange such that they tend towards thermal equilibrium. For electrons and ions, each thermalised themselves but with different temperatures, then

$$\frac{d\varepsilon_i}{dt} = -\frac{d\varepsilon_e}{dt} = -C_i \frac{T_i - T_e}{\tau_{ei}} \tag{2.28}$$

Where C_i is the ion specific heat capacity and τ_{ei} is the electron – ion equilibration time as given by Spitzer [63]

$$\tau_{ei} = \frac{3 m_e m_i k^{3/2}}{8(2\pi)^{1/2} n_i Z^2 e^4 \ln(\Lambda)} \sqrt{\frac{T_i}{m_i} + \frac{T_e}{m_e}} \tag{2.29}$$

Also of note is τ_{ce}, the electron self collision time, also from [63]

$$t_c \sim 2\times 10^5 \frac{T_e^{3/2}}{n_e \ln\Lambda} \tag{2.30}$$

This can be a useful estimate of the time taken to remove any anisotropy from a group of electrons and thereby achieve equilibration amongst themselves. It can be used to

provide a rough comparison of classical thermally based calculations such as these with the more detailed work on the true electron energy distributions examined later. It should also be noted that τ_{ei} is much larger than τ_{ce}.

ln (Λ) is the Coulomb logarithm defined as

$$\Lambda = \frac{3}{2Z^2}\left(\frac{T_e^3}{e^3 \pi n_e}\right)^{1/2} \tag{2.31}$$

2.5.3 Electron thermal conduction

The nature of OFI means that although within a region of a given ionisation state the electron temperature gradient will be small, the discontinuous boundaries between adjacent regions of ionisation will result in significant thermal conduction. The hot electrons on the axis of the pulse propagation direction are expected to rapidly cool though conduction with adjacent cooler regions. The classical heat flux Q_c for collisional diffusion may be used;

$$Q_c = -\delta \kappa \nabla T_e \tag{2.32}$$

where δ is a factor of order unity introduced by Spitzer [63] to ensure zero current but finite heat flow. For small temperature gradients the thermal conductivity as given by Spitzer [63] is

$$\kappa = \frac{20(2/\pi)^{3/2}(kT_e)^{5/2}k}{m_e^{1/2}e^4 Z \ln(\Lambda)} \tag{2.33}$$

For large temperature gradients such as those which are expected to occur between adjacent regions of plasma charge state produced by the OFI process, heat flux tends to a collisionless free streaming process. The free streaming limit represents the maximum heat flux given by the density of the energy density, electron thermal velocity and an empirical limiter as

$$Q_m = f(kT_e)n_e\left(\frac{kT_e}{m_e}\right)^{1/2} \tag{2.34}$$

The arbitrary numerical factor f is taken as 0.1 for the work presented here and is justified by empirical observations and a detailed Fokker-Planck calculation (see next section) [64] which puts the usual value in the range of $0.03 \leq f \leq 0.15$. Although the

calculations in [64] were made for high density plasmas, the results are expected to be accurate where the temperature gradients are steep over the scale lengths of a few electron mean free paths. We therefore justify the use of this method in the low density gaseous systems of interest here, given that the OFI process results in adjacent regions of ionisation where the temperature differences are initially discontinuous and therefore of very large temperature gradients. A more complete description of thermal transport in such plasmas requires a Fokker-Planck treatment.

A smooth transition between the two regimes is implemented in the codes by use of the harmonic mean, such that the electron heat flux Q_e is given by

$$Q_e = \left(\frac{1}{Q_c} + \frac{1}{Q_m} \right)^{-1} \tag{2.35}$$

2.6 Electron energy distributions

Previously in this chapter, the important processes involved in releasing electrons (OFI) and then those responsible for heating (ATI and IB) have been presented. These processes will produce an electron energy distribution (EED) upon which subsequent atomic and plasma physical processes will depend. A significant proportion of calculations involving X-Ray laser plasmas are often performed on the assumption that the EED within the plasma is thermal in nature and can therefore be treated with a Maxwell – Boltzmann (MB) distribution of characteristic temperature T_e. Often while this is not true of a system overall, it is a good approximation *locally* and regions of such plasmas are considered to be individually in local thermal equilibrium (LTE). Being able to use MB distributions greatly simplifies calculations, particularly when considering effects such as thermal conduction of different plasma species and atomic processes which are temperature dependent.

LTE simulations are certainly valid in solid target systems where the electron density is high ($>10^{20}$ cm^{-3}) and the primary energy absorption process is via IB over the relatively long incident pulse durations of several nanoseconds. At these densities and time scales, any initial non-thermal nature in the electron energy distribution is rapidly lost via electron – electron collisions. The validity of such assumptions when working with plasmas produced through OFI is more questionable given that the electron energy

distribution produced via OFI is strongly non-thermal given the sequential nature of ionisation. Furthermore, the lower electron densities of around 10^{16} to 10^{19} cm^{-3} limit the ability of electron – electron collisions to remove any non-thermalisation over time scales of relevance to the schemes considered in this thesis. Another consideration for use of more accurate modelling is that concerning mixtures of different gases. Later work will examine the use of hydrogen gas for use as a lasing channel which is doped with lasant gas species. The hydrogen will provide electrons of much lower temperature than the lasant gas and will result in a much cooler average electron temperature.

There are two main approaches to the modelling of EED functions, namely Monte Carlo (MC) methods in which binary collisions between a statistical sample of particles are considered, or by numerical solution of the Boltzmann equation with an appropriate collision term, commonly termed the Fokker – Planck method. Pert has examined both methods in subsequent papers with reference to OFI and ATI (ref. [53] for MC methods and [65] for solution of the Boltzmann equation.). While there are merits to both approaches, MC suffers from the inability to accurately describe the high energy tail of hot distributions. Also the statistical nature of the method means that the distribution is noisy even when large numbers of particles (>100,000) are used which is computationally expensive. The Boltzmann approach has the advantage that it allows the 'exact' form of the EED to be determined and is computationally much faster.

The modelling of arbitrary EED functions uses the Boltzmann equation with a Fokker-Planck collision term;

$$\frac{\partial f}{\partial t}+\mathbf{v}\cdot\frac{\partial f}{\partial \mathbf{r}}-\frac{e}{m}(\mathbf{E}+\mathbf{v}\times\mathbf{B})\cdot\frac{\partial f}{\partial \mathbf{v}}=\left.\frac{\partial f}{\partial t}\right|_{Coll} \tag{2.36}$$

Here f is the EED function and in general will be a function of position **r**, velocity **v** and time t. **E** and **B** are externally applied electric and magnetic fields which are both zero for the work considered in this thesis. For two particles i and j interacting via an inverse square force, the Fokker-Planck collision term is given by;

$$\frac{1}{\Gamma}\left.\frac{\partial f}{\partial t}\right|_{Coll}=-\frac{\partial}{\partial v_i}\left[f\frac{\partial h}{\partial v_i}\right]+\frac{1}{2}\frac{\partial^2}{\partial v_i\partial v_j}\left[f\frac{\partial^2 g}{\partial v_i\partial v_j}\right] \tag{2.37}$$

where Γ is a numerical constant and h and g are the Rosenbluth [66] potentials which are functions of velocity and time.

The first term on the right hand side of (2.37) represents the slowing of particles owing to collisions between themselves and can be considered a frictional term. The second term represents diffusion in velocity space. The frictional term tends to concentrate particles around the flow velocity of the plasma or bring them to rest in a stationary system. The diffusion term tends to spread particles in velocity space and the equilibrium MB distribution results from a balance between the two processes.

If it is assumed that in 1D the velocity distributions are isotropic then in the absence of applied fields, equation (2.36) can be expressed as;

$$\frac{\partial f}{\partial t} = \frac{1}{v^2}\frac{\partial}{\partial v}\left[\alpha f + \beta \frac{\partial f}{\partial v}\right] - v\frac{\partial f}{\partial x} \tag{2.38}$$

where

$$\alpha = \frac{(4\pi)^2 e^4 \ln(\Lambda)}{m^2}\int_0^v f(v')v'^2 dv'$$
$$\beta = \frac{(4\pi)^2 e^4 \ln(\Lambda)}{m^2}\frac{1}{3}\left[\int_0^v f(v')v'^4 dv' + \int_v^\infty f(v')v' dv'\right] \tag{2.39}$$

Pert [65] has detailed a numerical algorithm to solve the above equations and has included IB heating.

2.7 The noble gas lasing schemes

The three lasing schemes investigated in this thesis are those in the noble gases Ar, Kr and Xe and are based upon those first proposed by Lemoff *et al* [16]. For each of these ions, a laser irradiance of 10^{17} W/cm^2 is sufficient to strip the eight outermost electrons via OFI. This figure is significant in that it leaves these ions with a closed shell configuration of electrons which provides a degree of stability against further ionisation from collisional ionisation by the hot electrons which would otherwise remove the lasant ion from the plasma. The Ar^{8+}, Kr^{8+} and Xe^{8+} ions are often referred to as neon, nickel and palladium like respectively although throughout this thesis for reasons of brevity spectroscopic notation is generally used, i.e. Ar IX, Kr IX and Xe IX.

The Ne and Ni like schemes have been successfully proven as reliable in solid target collisionally pumped schemes as discussed in section 1.1.1 although the lower target densities used by the OFI scheme will result in less efficient pumping in this case.

2.7.1 Valence shell lasing

In principle each of the schemes is a simple three level system in which the upper laser level is pumped by monopole collisional excitation from the ground state.

The original work of Lemoff *et al* [16] considered only levels within the principle quantum shell of the lasing levels, that is the $n = 3$, $n = 4$ and $n = 5$ shells for Ar IX, Kr IX and Xe IX respectively and then only considered quasi-steady state (QSS) rates in order to determine the gain coefficient. While collisional excitation is a significant level population mechanism, there will in general be radiative decays from higher levels which are also populated by collisional excitation. This is a particularly important consideration given the high energy of the free electrons and the fairly long time scales over which the systems are expected to lase for of tens to a few hundreds of picoseconds. Therefore for the atomic simulations in this thesis many more levels are included allowing a more detailed collisional / radiative treatment. A full discussion of the level structure used for each scheme is given in the following chapter on atomic data.

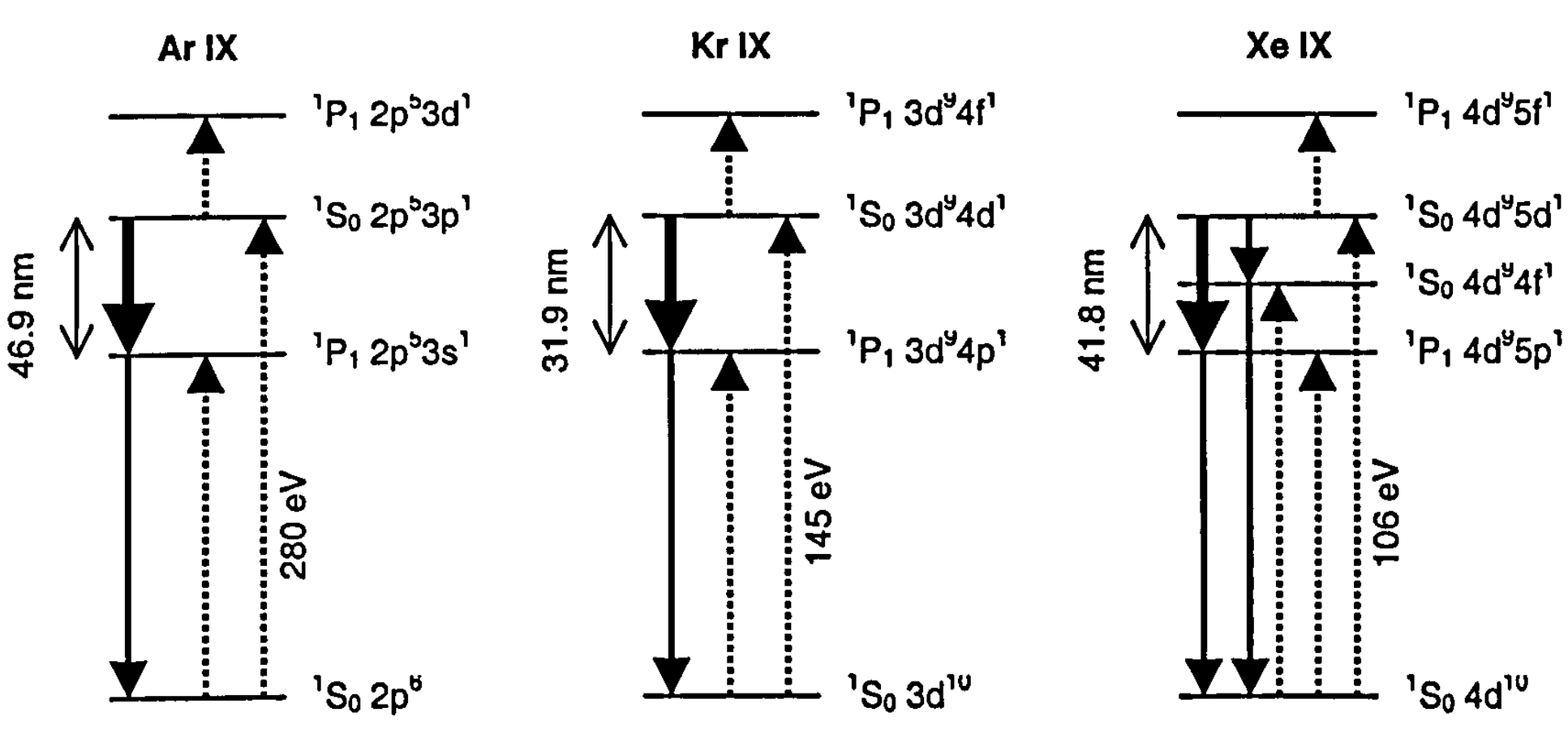

Figure 2.4. Simplified level scheme (of arbitrary scale) showing the main important levels and transitions for the lasant line of the three systems. For simplicity only the singlet levels are shown. The dashed lines show electron collisional transitions while the solid lines illustrate radiative transitions with the bold line being the laser transition. Also shown is the wavelength of the lasing line and the energy (above ground) of the transition to be pumped.

The Ar IX scheme was considered in some detail by Kim *et al* [67] for use in electrically discharged pumped systems. He calculated the level populations and gain coefficients for a number of 3p → 3s lines for a range of ionic densities and electron temperatures and concluded that gains of around 0.5 cm^{-1} could be expected at densities of around 10^{17} cm^{-3} and temperatures of 200 eV. For the purposes of this thesis, only the shortest wavelength line, the $^1S_0\ 2p^5 3p^1 \rightarrow {}^1P_1\ 2p^5 3s^1$ at 46.9 nm is considered.

All level energies, radiative and collisional excitation rates have been obtained with the RCN/RCG atomic code of Cowan [68] which is discussed further in Chapter 3.

2.7.2 Inner sub-shell lasing

If the free electrons have sufficient energy then they may be able to excite a bound electron from a level beneath the ground state of the ion ([Be]$2p^6$, [Ar]$3d^{10}$ and [Kr]$4d^{10}$ for Ar IX, Kr IX and Xe IX respectively.). In these cases, transitions will occur between inner sub-shell levels that have higher energies and thus shorter wavelengths. Although these systems are attractive in that they lead to shorter wavelength lasing, they are more difficult to demonstrate since they require more extreme physical conditions. The work of Healy *et al* [69] presented calculations of inner shell lasing in neon like germanium and yttrium but at electron energies of around 1.6 keV and densities of around 10^{21} cm^{-3}. Ivanova *et al* [70] calculated a small gain in neon like xenon lasing at 5.02 nm but did not discuss how such an ion could be created since with a threshold intensity of 2.4×10^{20} W/cm^2 it cannot easily be created by current lasers.

The success of these schemes depends upon the combination of high energies and densities. While the high electron energies are attainable via OFI, achieving the higher densities is much more difficult due to the driving beam propagation and as such there has been little consideration of inner shell lasing in OFI systems. However, with the possibility of guiding the driving pulse through higher density targets via techniques such as parabolic wave guides which are considered in this thesis, these schemes now become worthy of investigation.

Hooker [71] has presented QSS calculations of inner shell lasing in Ar IX and predicted modest gains of around 10 cm^{-1} for two inner shell lines at densities of around 3×10^{19} cm^{-3} although he predicted a much higher mean electron temperature than that predicted by the models used in this thesis.

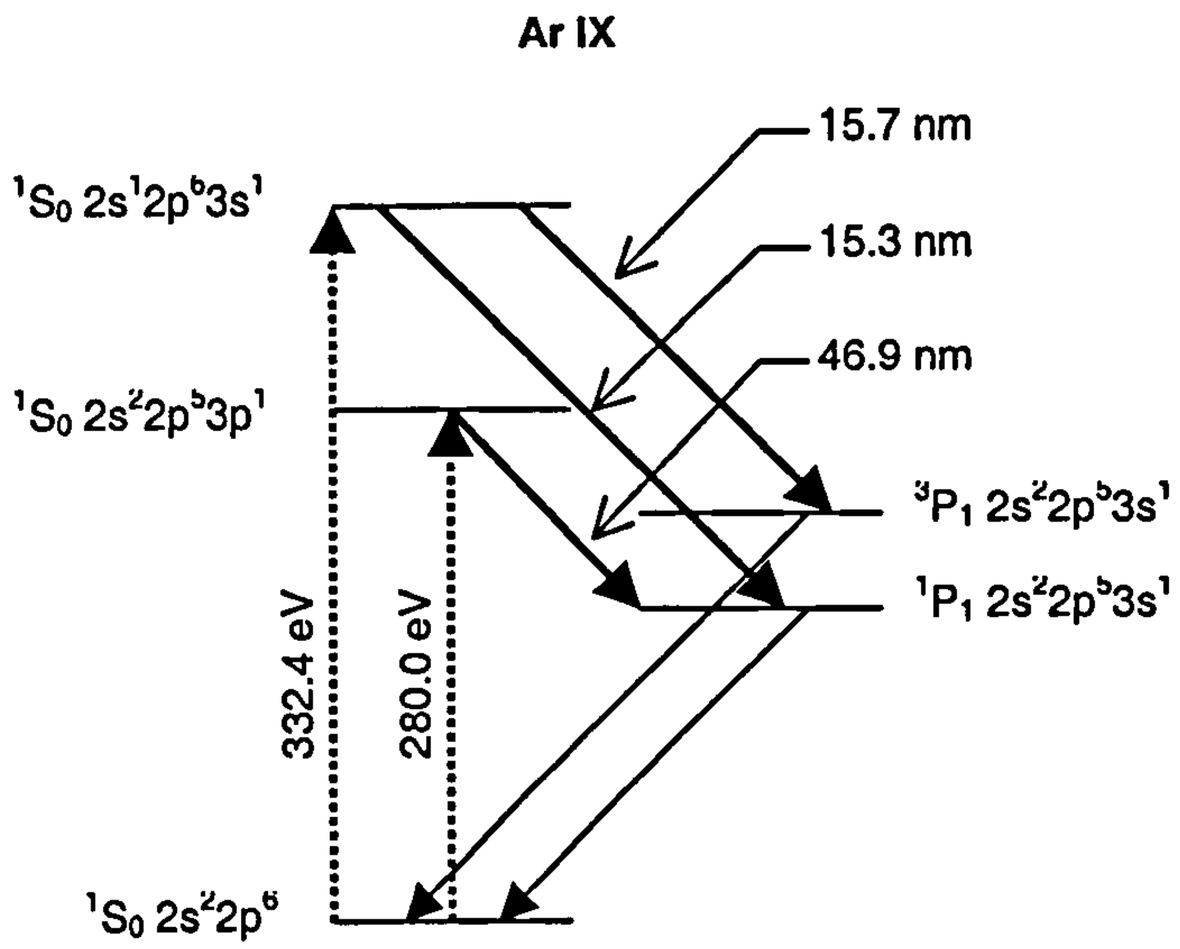

Figure 2.5. The lasing level diagram for Ar IX showing the inner sub-shell transitions

Figure 2.5 shows the simplified level diagram for Ar IX including the inner shell lasing lines. An important consideration to note is that the 15.3 nm and 46.9 nm lines share the same lower level. In this case, strong lasing from one of the lines may act to limit the lasing in the other.

No calculations have been performed specifically for Kr IX but the general nickel like schemes may be extended to Kr IX. However for this particular ion, the lowest energy inner-sub shell levels, those of [Mg]$3p^5 3d^{10} 4s^1$, have energies of up to 218 eV which is only 12 eV below the energy required to ionise to Kr X. This means that any plasma that is hot enough to excite this transition will also be hot enough to rapidly ionise out of these levels thereby preventing sufficient population to be established to generate significant lasing. This has been confirmed in exploratory simulations and it was decided that the very small gains of around 10^{-5} cm^{-1} did not warrant the computational effort required in simulating the additional levels.

The situation with Xe IX may be expected to be similar, however given the complexity of the Xe IX level structure (there is considerable mixing of the higher angular momenta *l* shells at the higher *n* shells) reliable calculations are difficult to achieve. There are no level calculations for inner sub-shell levels in the literature and they are beyond the scope of the facilities available for this thesis. Therefore, no inner sub-shell lasing calculations are examined for the Xe IX system.

2.8 Pulse propagation

The propagation of both the driving and X-ray laser pulse through the gas / plasma requires some examination, particularly given the long wavelength needed in these schemes which leads to severe refraction through the plasma. Much of the work presented here has been taken, with some modifications, from that of Grout [33]. The effects of propagation for a linearly polarised laser for recombination schemes was also investigated in [73]

2.8.1 Driver pulse

The leading edge of the pulse will ionise the gas such that the bulk of the pulse following will be refracted. The refractive index in a plasma is given by

$$\eta^2 = 1 - \frac{n_e}{n_{cr}} \tag{2.40}$$

where n_{cr} is the critical density, above which propagation of radiation is not possible

$$n_{cr} = \frac{\varepsilon_0 m_e \omega^2}{e^2} \tag{2.41}$$

It is therefore seen that any electron gradient will result in a corresponding refractive index gradient which will act to refract the laser pulse. The nature of the OFI process means that an electron density maximum is created on the pulse propagation axis and the resulting refractive index gradient will act to defocus the beam into the lower electron density regions. Techniques for creating a density minimum on axis and thus effectively prevent the pulse from refracting by means of a positive gradient in the refractive index are discussed in section 5.4.

The diffractive spread of a light wave is $\sim \lambda / a$ where a is the focal width. Thus the more tightly focussed the beam, the more it will diffract. Small focal spot sizes are typically used in OFI experiments as a means of achieving the high irradiances needed and this then becomes important.

The physics of light may be treated in two different ways, either by geometric or by wave optics. Wave optics are necessary where the diffractive spread is important, i.e. for Fresnel numbers, F, of order unity and smaller

$$F = \frac{\text{Geometric spread}}{\text{Diffractive spread}} = \frac{a^2}{\lambda l} \tag{2.42}$$

where l is the length of medium that the signal is passing through. For OFI pulses applicable to this thesis, then $a \sim 30$ μm, $\lambda = 800$ nm and $l \sim 5$ mm giving $F \sim 0.2$.

For an ionising laser beam the Fresnel diffraction integral in differential form is used. From this the time dependant scalar wave equation is given by

$$\frac{\partial^2 E}{\partial r^2} - \frac{1}{c^2}\frac{\partial^2 E}{\partial t^2} = \frac{1}{\mu_0}\frac{\partial J}{\partial t} \tag{2.43}$$

This is known as the inhomogeneous Helmholtz equation. Ionisation of the plasma is included as a source term in the plasma current

$$J = -n_e e v_e \tag{2.44}$$

where v_e is the electron velocity.

Consider a cylindrically symmetric pulse function which does not change appreciably as the wave propagates and can be written in the trial form

$$E = u(r,z,t)\exp[i(kz - \omega t)] \tag{2.45}$$

With wavenumber k and angular frequency ω. Using the Laplacian operator in cylindrical geometry, and making the paraxial approximation ($z >> r$) then the temporal evolution of the pulse, neglecting seconding order derivatives with respect to z and t, may be written as

$$\frac{\partial u}{\partial t} = \frac{ic}{2k}\left(\frac{\partial^2 u}{\partial r^2} + \frac{1}{r}\frac{\partial u}{\partial r}\right) - c\frac{\partial u}{\partial z} - \frac{ikc}{2}\frac{n_e}{n_{cr}}u \tag{2.46}$$

The right hand side terms represent radial diffraction, propagation evolution and ionisation induced refraction respectively. A description of the Gaussian paraxial wave without refraction of mode structure is given by Hawkes and Latimer [72] as

$$E(r,z) = E_0 \frac{w_0}{w(z)}\exp\left[-\frac{r^2}{w(z)^2}\right]\exp\left[-i\left\{kz - \tan^{-1}\left(\frac{z}{z_R}\right)\right\}\right]\exp\left[-i\left\{\frac{kr^2}{2R(z)}\right\}\right] \tag{2.47}$$

The three terms describe the amplitude, longitudinal phase and radial phase of the pulse respectively. For finite pulses the temporal amplitude variation of the pulse also needs to be considered through E_0.

In the above equation, w_0 is the beam waist which is the radial distance at $z = 0$ where the field amplitude falls to $^1/_e$ of the value at the peak amplitude. The Rayleigh length is defined as the propagation distance over which the beam waist increases by a further factor of $2^{1/2}$

$$z_R = \frac{\pi w_0^2}{\lambda} \tag{2.48}$$

The radial distance to the $^1/_e$ point defines the spot size and is given by

$$w(z)^2 = \frac{2}{kz_R}\left(z_R^2 + z^2\right) \tag{2.49}$$

The longitudinal phase term allows for the π phase shift as the beam passes through the focus, known as the Guoy shift. The wavefront radius of curvature is given by

$$R(z) = \frac{z^2 + z_R^2}{z} \tag{2.50}$$

An indication of conditions for when refraction becomes important is given by Rankin *et al* [74]. A $\pi/2$ phase change at the beam centre produces a modification of one diffraction limited divergence. This phase change occurs over a plasma length, L_D, given by

$$L_D = \frac{\lambda}{2}\frac{n_{cr}}{n_e} \tag{2.51}$$

Refraction is expected to occur if this distance is shorter than the Rayleigh length. Refraction is therefore expected to be significant if

$$\frac{n_{cr}}{n_e} > \frac{\lambda^2}{2\pi w_0^2} \tag{2.52}$$

For a 800 nm laser, $n_{cr} = 1.9 \times 10^{21}$ cm^{-3} and with $n_e \sim 10^{18}$ cm^{-3} then diffraction can be expected to be important for spot sizes of around 14 μm and will therefore play an important role in propagation effects.

2.8.2 X-ray pulse

In a plasma, light at shorter wavelengths has a larger group velocity than at longer wavelengths. Therefore the produced X-ray pulse will eventually catch up and overtake

the optical driving pulse. Once this occurs the X-ray pulse will be propagating in neutral gas and amplification will cease and so it becomes pointless trying to create target lengths greater than this distance.

It is most advantageous for the X-ray pulse to remain a constant delay behind the driver pulse so that the highest population inversion are sampled and the amplification is at a maximum. This can only be achieved using a travelling wave configuration which is not appropriate to these OFI schemes. An estimate of the interaction length is given by time taken to reach the same position. Assuming that the optical pulse leads the X-ray pulse by a time τ then

$$\frac{L_{(X)}}{v_{g(X)}} = \frac{\left(L_{(X)} - v_{g(OPT)}\tau\right)}{v_{g(OPT)}} \tag{2.53}$$

Where $v_{g(X),(OPT)}$ are the X-ray and optical pulse group velocities respectively. $L_{(X)}$ is the distance travelled by X-ray pulse and allows the interaction distance to be estimated as

$$L_{(X)} = \frac{v_{g(X)}v_{g(OPT)}\tau}{v_{g(X)} - v_{g(OPT)}} \tag{2.54}$$

The group velocities are given by

$$v_{g(X),(OPT)} = c\left[1 - \left(\frac{\omega_p}{\omega_{(X),(OPT)}}\right)^2\right]^{1/2} \tag{2.55}$$

Simulations in this thesis suggest a typical time to develop the peak gain of around 5 ps for electron densities of 8×10^{18} cm^{-3}. Thus for X-ray and optical wavelengths of ~ 40 nm and 800 nm respectively, with respective group velocities of 2.99798×10^8 ms^{-1} and 2.99122×10^8 ms^{-1}, this interaction length is around 60 cm and is thus much larger than any likely plasma length.

2.9 Atomic Physics

The production of lasing requires the creation of physical conditions which do not exist in a normal state of thermal equilibrium. Once this situation is created, there may be a number of different processes occurring within the atoms and ions which may be required for, or be detrimental to, the lasing process.

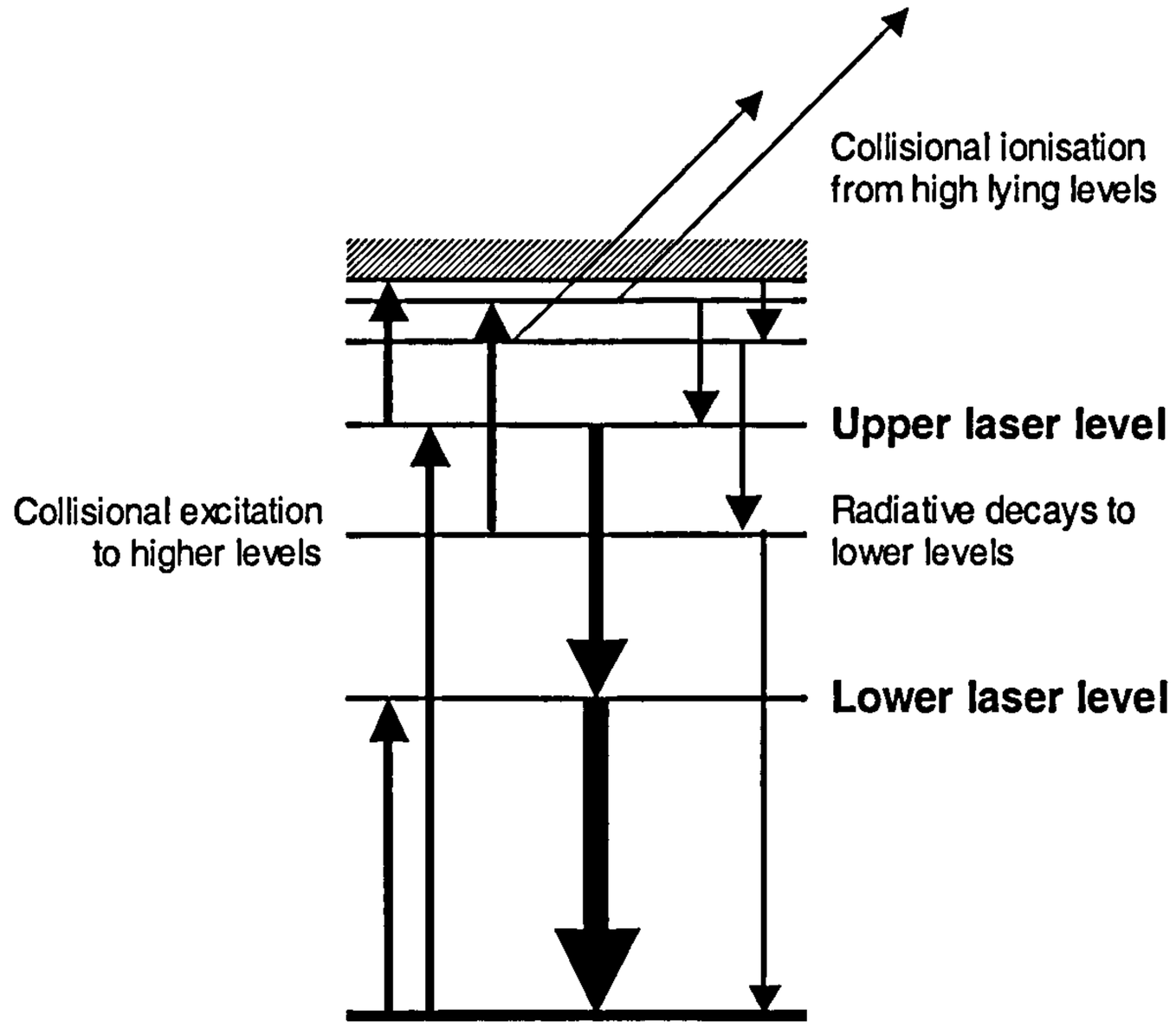

Figure 2.6. Level schematic of an atom/ion showing the dominant processes for the collisionally pumped laser. As collisional excitation populates higher levels, radiative decays repopulate the lower levels. Lasing will occur between the upper and lower levels if more ions exist in the upper state than the lower. High lying levels will tend be depopulated by collisional ionisation.

Following OFI of the gas with a circularly polarised beam, a plasma will be created which will consist of cold ions with their remaining bound electrons in the ground state and hot free electrons at a density given by (2.27) where immediately following OFI, Z^* will be an integral number (at least in the central region of the pulse). The hot free electrons will then collisionally excite the bound electrons into higher bound states from where they will radiatively decay to lower states in successive stages until the ion is returned to the ground state. Meanwhile the free electrons may further ionise the ion. These processes are shown schematically in Figure 2.6

2.9.1 Radiative processes

For a system with a number of different states with populations N_1, N_2, $N_{...}$ of energies E_1, E_2, $E_{...}$ ($E_1 < E_2 < E_{...}$) with associated degeneracies g_1, g_2, $g_{...}$ then we can say that there is a certain probability per unit time of atoms in a state 2 decaying to a lower state 1, i.e.;

$$\frac{dN_2}{dt} = -A_{21}N_2 \tag{2.56}$$

where A_{21} is the Einstein A coefficient or more descriptively, the spontaneous decay rate coefficient

$$A_{21} = \frac{8\pi^2 e^2}{3\varepsilon_0 c^3 \hbar}\frac{g_1}{g_2}\nu^3 \left|\mathcal{R}_{21}\right|^2 \tag{2.57}$$

Where ν is the linear frequency of the radiation and $\mathcal{R}_{21}$ is the electric dipole matrix element which can only be accurately determined from quantum mechanical calculations of atomic the wave functions.

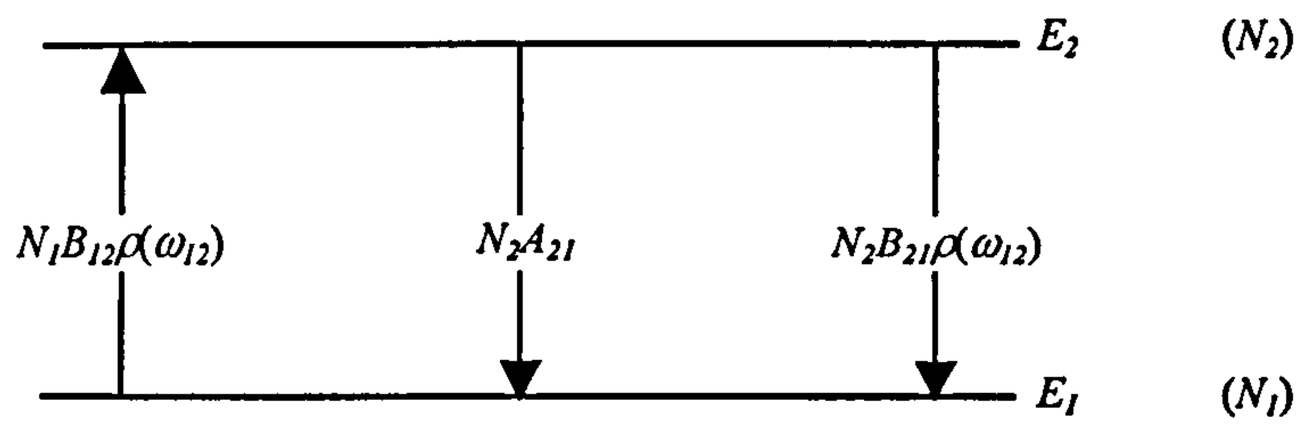

Figure 2.7. A simple two level structure showing the possible radiative transitions between them. From left to right; absorption of incident radiation of irradiance ρ at a frequency ω_{12}, spontaneous decay and finally stimulated emission by incident radiation.

A second possible process is that of absorption of incident radiation of irradiance $\rho(\omega)$. The atomic structure will allow absorption of frequency ω_{12} at a rate of $N_1B_{12}\rho(\omega_{12})$. However, the reverse process is also possible whereby radiation of the same frequency may stimulate the decay of the upper state to the lower. This is the process of *stimulated emission* which will occur at a rate of $N_2B_{21}\rho(\omega_{12})$. Stimulated emission differs from spontaneous in that is emitted with the same phase as the incident radiation and in the same direction. It is therefore coherent and hence leads to many of the useful properties of laser light. It can be shown that [72];

$$B_{21} = \frac{g_1}{g_2}B_{12} \tag{2.58}$$

All three processes are illustrated in Figure 2.7. Finally, there is a simple ratio between the spontaneous and stimulated emission coefficients;

$$\frac{A_{21}}{B_{21}} = \frac{\hbar\omega^3}{\pi^2 c^3} \tag{2.59}$$

2.9.2 Amplified emission

Again using the notation for an atom with a number of energy states $E_{...}$ presented in the above section, then in thermal equilibrium the ratio of populations of any two states is given by

$$\frac{N_2}{N_1} = \frac{g_2}{g_1} \exp\left(-\frac{E_2 - E_1}{k_B T}\right) \tag{2.60}$$

Given that the rates for absorption and stimulated emission are equal (ignoring the statistical weights) then for light amplification by stimulated emission (lasing) to occur there must be more atoms in the upper state (N_2) than the lower (N_1) which, from the above equation, is a non-equilibrium situation and thereby requires an input of energy to achieve. This is the process of pumping such that a population inversion is formed. More strictly, the statistical weights must also be considered such that lasing may occur if

$$\frac{N_2}{g_2} > \frac{N_1}{g_1} \tag{2.61}$$

Clearly if an inversion can be maintained for useable periods of time (of the order of the lifetime of the upper state) then the stimulated emission from one event may lead to another such that amplification may occur. The amplification in irradiance I of radiation along a medium is simply described by

$$I = I_0 \exp(gl) \tag{2.62}$$

where I_0 is the irradiance at some initial position, l is the distance travelled through the medium and g is the small signal gain coefficient. Amplification of any initial radiation will therefore occur for $g > 0$. For significant amplification, a large gain length product, gl, is required. In optical lasers this is usually achieved with g only slightly larger than zero but with a considerable amplification length through the use of mirrors. The general lack of X-ray mirrors and difficulties in producing long plasma columns means that scaling towards shorter wavelengths requires much larger gain coefficients.

The gain coefficient [72] is dependant upon the size of the population inversion, the wavelength of the lasing line (through the angular frequency ω), the spontaneous emission coefficient from the upper to the lower level, A_{21} and also the line shape function $v(\omega)$;

$$g(\omega) = \nu(\omega)\left(N_2 - \frac{g_2}{g_1}N_1\right)A_{21}\frac{\pi^2 c^2}{\omega^2} \tag{2.63}$$

This is strictly only valid until the onset of gain saturation. At this point, the stimulated emission radiation causes depopulation of the upper level at the same rate as it is populated by other mechanisms and amplification occurs linearly with distance along the medium. The output irradiance at which gain saturation occurs, I_s, is called the saturation irradiance. The saturated irradiance is important in that it represents the point at which the maximum amount of energy is being extracted through lasing. It is also, in theory, relatively straightforward to measure experimentally through graphs of output irradiance (or energy) as a function of the length of the lasing media.

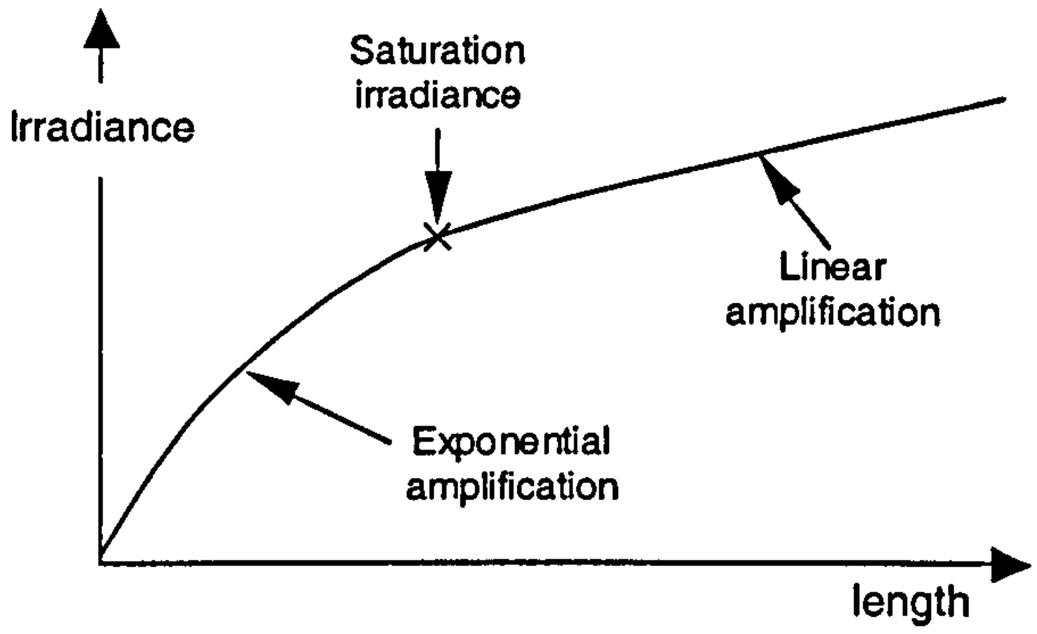

Figure 2.8. Schematic graph showing the behaviour of laser amplification as a function of the laser medium length. Once amplification occurs linearly with distance, this irradiance is known as the saturation irradiance.

The line shape function, which describes the effect of various line broadening mechanisms, is normalised such that;

$$\int_{-\infty}^{\infty} \nu(\omega)d\omega = 1 \tag{2.64}$$

The saturation irradiance within a homogenous medium can then be expressed by [72];

$$I_s = \frac{\hbar\omega}{\tau_2}\frac{1}{\sigma_{SE}(\omega_0)} \tag{2.65}$$

where τ_2 is the recovery time of the upper state and σ_{SE} is the stimulated emission cross section (at the line centre, ω_0);

$$\sigma_{SE}(\omega) = \nu(\omega)\frac{A_{21}}{g_1}\frac{\lambda_0^2}{4n^2} \tag{2.66}$$

n is the refractive index of the medium which for the purposes of this thesis is considered to be unity.

A more detailed analysis of lasing in an inhomogeneous medium (which is more strictly the case in the plasmas of interest here) is given by Hawkes and Latimer [72] while Pert [75] develops a model specifically aimed at determining the output characteristics of amplified stimulated emission lasers. Detailed expressions for the local gain and saturation irradiances are presented and it was found that the above equations will tend to overestimate the amplification before and during saturation. The effect is not important in this thesis where no detailed effort is made to analyse the exact nature of the output X-ray laser through ray tracing techniques.

2.9.3 Collisional excitation

If free electrons have an energy equal to or greater than the difference between the energies of bound ionic levels i (initial lower level) and f (final upper level) then they will have a certain probability of exciting those electrons to the upper level. This is the process of collisional excitation. It is useful to express the rate at which a unit volume of ions is excited from the initial to final state in terms of a collision cross section σ, the velocity v of the free electrons and their distribution, $f(v)$;

$$C_{if} = \langle \sigma_{if} v \rangle = \int v \sigma(v) f(v) dv \tag{2.67}$$

The collision cross section is more often given in terms of the dimensionless collision strength, Ω, which can be obtained from quantum mechanical calculations;

$$\sigma(\varepsilon)_{if} = \frac{h^2}{8\pi m_e \varepsilon_c g_i} \Omega(\varepsilon)_{if} \tag{2.68}$$

where ε_c is the energy of the impacting electron. Thus if the collision strength is available over a range of energies then the collision rate for an arbitrary EED can be obtained by;

$$C_{if} = \frac{\pi a_0^2}{g_i} \int \frac{v \Omega(v)_{if} f(v)}{\varepsilon_c} dv \tag{2.69}$$

If a thermal MB distribution of temperature T_e (in eV) is assumed then the excitation rate can be more simply expressed as;

$$C_{if} = 8.01\times10^{-8}\frac{\sqrt{T_e}}{g_i}\int_y^\infty \Omega(\varepsilon_c)_{if}\, e^{-u}\, du \qquad (2.70)$$

where $y = \Delta\varepsilon_{if} / T_e$, $u = \varepsilon_c R_\infty / T_e$ with R_∞ being the Rydberg constant = 13.606 eV.

For the purposes of practical calculations, equation (2.70) still requires numerical integration of the collision strengths over a large energy range which can be computationally expensive. A more compact form (in terms of the data required to be stored and the calculations needed) is that of van Wyngaarden *et al* [76]. The collision strengths are firstly fitted to the following form;

$$z^2\Omega(x)_{if} = d_0 + d_1x^{-1} + d_2x^{-2} + d_3x^{-3} + d_4x^{-4} + d_5\ln x \qquad (2.71)$$

where $z = Z$ - 1 is the net charge experienced by the active ionic electron, i.e. that being excited and $x = \varepsilon_c / \Delta\varepsilon_{if}$.

The collisional excitation rate can then be obtained from;

$$C_{if} = 8.01\times10^{-8}\, yz^{-2}\sqrt{T_e}\, I \qquad (2.72)$$

where

$$I = y^{-1}\left[d_0e^{-y} + d_5E_5(y)\right] + \sum_{n=1}^{4} d_nE_n(y) \qquad (2.73)$$

with

$$E_n(y) = \int_1^\infty x^{-n}e^{-yx}\, dx \qquad (2.74)$$

For cases where the collision strengths are not available it may be appropriate to use simple formulae to calculate the excitation rate, a review of which is given by Salzmann [77]. That utilised by the codes used in this thesis is of van Regemorter [78];

$$C_{if} = 3.2\times10^{-7}\left(\frac{R_\infty}{T_e}\right)^{3/2} g_f\frac{e^{-y}}{y}G(y) \qquad (2.75)$$

where $G(y)$ is the Gaunt factor which accounts for quantum mechanical corrections. Its asymptotic behaviour for small and large arguments is;

$$G(y) \approx \begin{cases} \sqrt{3}E_1(y)/2\pi & y \to 0 \\ 0.200 & y > 1 \end{cases} \qquad (2.76)$$

The van Regemorter rate is reasonably accurate for transitions within the same principal quantum shell but for $\Delta n > 0$ the accuracy is expected to be no more than an order of magnitude.

2.9.4 Collisional ionisation

A free electron, if sufficiently energetic, may collide with and release a bound atomic electron, thus increasing the ionisation state of the ion. This process is important with respect to our OFI schemes in that with an electron temperature of order 0.5 to 2 keV these electrons will act to remove the lasing ion from the plasma and thus limit the lasing action. This collisional ionisation process will also act to change the electron density gradients within the plasma and thus affect beam propagation. In addition to these detrimental effects, ionisation will occur in regions of plasma which, following the OFI driving pulse, are below the required lasing stage and may act to create the required ion. Further, as collisional excitation populates higher and less tightly bound atomic states, these will be more easily depopulated by collisional ionisation. This may be a significant factor for the Xe scheme.

The calculation of collisional ionisation rates requires detailed quantum mechanical calculations which are beyond the scope of this thesis and the codes used. However there are a number of empirically based formulae available that are generally accurate to around 10% which allow for rapid calculations. A review of a number of these is given by Salzmann [77]. That implemented by the codes used in this work is of Lotz [79];

$$\mathcal{J}_{c.nl} = 3\times10^{-6}\,\xi_{c,nl}\,T_e^{-3/2}\,\frac{1}{y}E_1(y) \tag{2.77}$$

where the subscript c refers to the charge state of the ion and nl of the principle and angular quantum numbers of the state being ionised from. $\xi_{c,nl}$ is the number of electrons in the ionising shell. y is the energy of the impacting electron;

$$y = \frac{\left|\varepsilon_{c,nl}\right|}{T_e} \tag{2.78}$$

2.9.5 The collisional – radiative (COLRAD) model

(Much of the work presented here is similar to the thesis of Grout [33] but is reproduced in brief here with the discussion shifted to collisional excitation considerations since it is of central importance in the simulations used throughout this thesis. For a detailed discussion of the model, see[33].)

For any realistic calculation of lasing to be performed, it is necessary to follow the temporal evolution of the populations of the atomic levels involved in lasing which will in general require all possible rates to be determined for processes between all available atomic states, i.e.

$$\frac{dq_m}{dt} = \sum_{n \neq m} \left(X_{mn} q_n - X_{nm} q_m \right) \tag{2.79}$$

where q_m is the fractional population of state m and X_{mn} is the total transition rate involving all possible transitions between states m and n.

A complete series of energy levels in an ion with collisional and radiative transitions at an appropriate rate in steady state was first formulated by Bates *et al* [80] which is still the basis for many calculations today, in particular those of Lemoff *et al* [16] upon which this thesis is based, are such steady state calculations. The model was subsequently extended by McWhirter and Hearn [81] and then Burgess and Summers [82] to a time dependent model. The total transition rate, X_{mn}, between bound states is

$$X_{mn} = n_e C_{mn} + \begin{cases} A_{mn} & \text{if } E_n > E_m \\ 0 & \text{otherwise} \end{cases} \tag{2.80}$$

where A_{mn} and C_{mn} are the radiative and collisional rates defined in sections 2.9.1 and 2.9.3 previously.

The bound – free transitions include collisional ionisation (implemented in our versions of COLRAD by the theory described in section 2.9.4), three body recombination, radiative recombination, dielectric (non-hydrogenic ions) recombination, autoionisation and cascade recombination. The various recombination processes require a cold plasma to be significant and while they're included in the COLRAD model, they are not important to this thesis and are not considered further.

The complete COLRAD model allows the energy change involved in transitions to be determined and thus allows changes in the temperature of the electrons within the plasma to be calculated. This is important with respect to this work since collisional

excitation of the atomic states will lead to a cooling of the electrons which will eventually terminate effective pumping of the upper laser level and thereby lasing itself.

In modelling X-ray lasers, the time dependant COLRAD model [83] can be integrated alongside the hydrodynamic simulation [84]. However, a complete description of all atomic states within the plasma would be computationally prohibitive and therefore only the ionisation state of the lasing ion is considered in detail which is sufficient to accurately examine the lasing process. A number of states which are relativistically split into LSJ coupled levels are used which approach the ionisation threshold of the lasing ion.

The creation of the atomic data required by the COLRAD model for this thesis is discussed in Chapter 3.

Chapter 3

Atomic Data

3.1 Introduction

In section 2.7 the noble gas schemes were discussed and the lasing levels and lines presented, while in section 2.9 the atomic processes of importance were detailed before the COLRAD model was presented. In order to make use of this model a considerable quantity of atomic data must be supplied if an accurate calculation is to be made. Unfortunately, there are few published measurements of the atomic levels and transition rates for the ions of interest to this thesis and while there is a modest amount of computationally calculated data published for a range of metallic ions (refs [85], [86] and [87]) aimed at astrophysical and X-ray laser calculations, none of any detail currently exists for the ions under consideration here. It has therefore been necessary to generate appropriate atomic data specifically for the simulations codes used later in this work.

A number of widely used and independently verified codes are freely available for the generation of atomic data. The multi-configurational Dirac Fock (MCDF) code of Grant *et al* [88] can calculate atomic energy levels in a number of coupling schemes and oscillator strengths to an accuracy of better than 1% in most cases. For collisional excitation rates, distorted wave (for theory aimed at computational evaluation see [89] and [90]) codes such as that of Eissner [91] are capable of producing accurate data which can include resonant structure. The limited available published data is generally calculated from such codes although the computational demands involved in evaluating any realistic case are considerable. Although the codes of [88] and [91] are individually highly accurate, neither produces each of the level energies, oscillator strengths and collision strengths necessary for the work here. Initial efforts to combine the data of both produced unsatisfactory results in test cases where published data was available.

It was therefore decided to use the atomic code of Cowan [68]. This is a highly versatile suite of codes capable of self consistently calculating data for a large number of atomic processes including those necessary for this work. The codes are relatively easy to use and capable of calculating realistic cases in a matter of minutes on current desktop computers. Level energies and oscillator strengths are generally accurate to around 1%. Collision strengths are less accurate since the Plane-wave Born calculations are only partially relativistic and cannot calculate resonant structure but only the general trend. Nevertheless, collision strengths are generally accurate to 25% and are rarely worse than 100%. Work by King [92] on iron targets in solid target collisionally pumped X-ray lasers comparing calculations made with the Cowan data with that from Zhang *et al* [86] showed that the COLRAD model using the Cowan data is still accurate. Using the data of Cowan has also allowed the development of simple codes to consolidate the output automatically into a form suitable for our simulation codes. Thus once verified, datasets can now be created in a matter of minutes.

This chapter is intended to outline the data obtained in order to model the noble gas schemes and discuss its accuracy where comparisons are available. Detailed data is not listed verbatim but in sufficient depth to allow the important points later in this thesis to be discussed.

3.2 Ionisation energies

Although widely available, the ionisation energies of up to the 10^{th} stage are listed here for reference since they are of some importance in later considerations.

Of note in the above table is the energy needed to ionise beyond the lasing ion (indicated by the bold entry). Collisional ionisation will act to remove the required stage from the plasma if a significant proportion of the electrons have energies above the ionisation energy. Therefore argon will offer the best degree of stability while xenon may be easily over-ionised.

These ionisation energies should be compared with the energy of the upper laser level, these being 280 eV, 145 eV and 106 eV for Ar, Kr and Xe respectively. For Xe, this energy is not far from that required to ionise to the next stage and therefore

as discussed in section 2.9.4, there will need to be significant populations in states higher that the 5d to prevent collisional ionisation depopulating the upper laser level.

	Ar		Kr		Xe	
I	$3p^6$	15.76	$4p^6$	14.00	$5p^6$	12.13
II	$3p^5$	27.63	$4p^5$	24.36	$5p^5$	21.21
III	$3p^4$	40.74	$4p^4$	36.95	$5p^4$	32.12
IV	$3p^3$	59.81	$4p^3$	53.00	$5p^3$	38.30
V	$3p^2$	75.02	$4p^2$	65.00	$5p^2$	51.50
VI	$3p^1$	91.01	$4p^1$	78.00	$5p^1$	64.20
VII	$3s^2$	124.3	$4s^2$	111.0	$5s^2$	91.40
VIII	$3s^1$	143.5	$4s^1$	123.0	$5s^1$	106.6
IX	**$2p^6$**	**422.5**	**$3d^{10}$**	**230.9**	**$4d^{10}$**	**175.2**
X	$2p^5$	478.7	$3d^9$	275.0	4d9	196.2

Table 3.1. Ionisation energies (eV) for first 10 stages of each of the noble gases. Also shown is the configuration of the electron to be removed from a given stage to ionise to the next.

The laser threshold intensity needed to ionise to the eight stage, as given by equation (2.2) is 2.7×10^{16} W/cm^2, 1.5×10^{16} W/cm^2 and 8.3×10^{15} W/cm^2 for argon, krypton and xenon respectively. Those required to over ionise to the next stage are 1.6×10^{18} W/cm^2, 1.4×10^{17} W/cm^2 and 4.8×10^{16} W/cm^2. It should be remembered that these are for a constant static field only and that the ionisation rates need to be calculated through the rate equations given in section 2.2. However, these figures clearly illustrate the order of magnitude difference needed in intensity to ionise beyond the eighth stage.

3.3 Atomic energy levels

In order to adequately model the lasing ion stage it is necessary to have sufficient energy levels defined such that the overall system can accurately calculate the rates into and out of the small number of levels which are of interest, i.e. the lasing levels for this work. Thus many more levels than the lasing levels themselves are required so that collisional excitation from, and radiative decay to, the lasing levels can be determined. While memory restrictions are no longer a real problem with current computers, determining rates between n levels requires of order n^2 calculations

which imposes a practical restriction on the number of levels modelled. The problem is exacerbated given the nature of LSJ coupling at high n and l quantum numbers which results in large numbers of levels.

As a practical compromise, configurations are used with the principle quantum shell involved in lasing and the next two. All l subshells within these are used with the exception of the 7h shell for Xe which lead to divergent calculations within the Cowan code. This allows for a considerable number of levels above the those involved in lasing to be modelled approaching reasonably close to the ionisation limit. The configurations used for each ion are listed in Table 3.2. These resulted in 125, 207 and 263 LSJ coupled levels for Ar IX, Kr IX and Xe IX respectively.

Ar IX	Kr IX	Xe IX
[Ne]	[Ni]	[Pd]
[Be] $2p^5 3l^1$ ($l = 0 \rightarrow 2$)	[Ar] $3d^9 4l^1$ ($l = 0 \rightarrow 3$)	[Kr] $4d^9 4f^1$
[Be] $2p^5 4l^1$ ($l = 0 \rightarrow 3$)	[Ar] $3d^9 5l^1$ ($l = 0 \rightarrow 4$)	[Kr] $4d^9 5l^1$ ($l = 0 \rightarrow 4$)
[Be] $2p^5 5l^1$ ($l = 0 \rightarrow 4$)	[Ar] $3d^9 6l^1$ ($l = 0 \rightarrow 5$)	[Kr] $4d^9 6l^1$ ($l = 0 \rightarrow 5$)
[He] $2s^1 2p^6 3l^1$ ($l = 0 \rightarrow 2$)		[Kr] $4d^9 7l^1$ ($l = 0 \rightarrow 5$)

Table 3.2. Atomic shell configurations used to calculate levels in LSJ notation for the three gases.

The scarcity of available data for the levels of these ions has made verification of the produced data difficult, particularly as much of the previous theoretical work on these schemes has also been done on the basis of the Cowan code (refs. [16] and [71]). Table 3.3 lists a number of levels of significance for each ion and shows comparisons where available.

The agreement is generally good, with the possible exception of the upper laser level for Kr. However, the comparison for this case from [93] is made on the basis of interpolated data made to fit the same lasing line in Ni like Y, Zr, Nb, Mo, Pd, Ag and Cd. The $4f^1\ ^1P_1$ level for Xe is of some concern since it may provide an important decay route from the upper laser level. Our data has this level barely lower than the upper laser level, compared to the difference from [94] of 1.4 eV however

exploratory simulations using the correct value showed negligible difference in the gains produced.

Ar IX			Kr IX			Xe IX		
Level	Energy (eV)	% Diff	Level	Energy (eV)	% Diff	Level	Energy (eV)	% Diff
$2p^5 3p^1\ ^1S_0$	280.92	+0.3[4]	$3d^9 4d^1\ ^1S_0$	146.15	+1.6[2]	$4d^9 5d^1\ ^1S_0$	105.58	+0.9[3]
$2p^5 3s^1\ ^1P_1$	253.70	-0.3[1]	$3d^9 4p^1\ ^1P_1$	106.27	- 0.1[1,2]	$4d^9 5p^1\ ^1P_1$	75.28	+0.4[3]
$2s^1 3p^1\ ^1P_1$	347.78	-0.1[1]	$3d^9 4f^1\ ^3P_1$	160.46	-0.6[1]	$4d^9 4f^1\ ^1P_1$	105.07	+1.8[3]
$2p^5 4s^1\ ^3P_2$	334.56	-0.1[1]						
$2p^5 5s^1\ ^3P_2$	369.04	0.0[1]						
$2p^5 5f^1\ ^3F_4$	378.27	0.0[1]						
$2p^5 5f^1\ ^3F_2$	380.55		$3d^9 6g^1\ ^3H_4$	203.51		$4d^9 7g^1\ ^3H_5$	158.74	

Table 3.3. Selected LSJ levels and their energies as determined by the Cowan code. Where published data is available from measurements or calculation by a different code, percentage differences are shown. Those annotated with the superscript 1 are from ref. [95], 2 from [93], 3 from [94] and 4 from the fact that the 46.9 nm line in argon is well characterised and thereby allows the energy difference of the two levels to be calculated. The first two entries for each ion are the upper and lower valence shell lasing line levels and the last is the highest energy level included in each dataset for comparison with the ionisation energy.

For the cases of Ar and Xe, the valence shell lasing lines have been observed experimentally thereby allowing the energy difference between the two levels to be determined. Given the fairly small discrepancies in these cases, the energies of these levels used in the simulations have been overridden from those shown in Table 3.3 with known values.

3.4 Radiative emission rates

Radiative emission rates, specifically the spontaneous emission coefficients, A_{fi}, are also calculated by the Cowan code for all dipole-allowed transitions. The lack of published measured rates for these transitions makes direct comparison impossible, however they may be expected to be of the same order of accuracy as the level

energies. This has been confirmed for a number of transitions in the test case of Ne-like Fe where alternative data is available from [85] and [86].

3.5 Collision strengths

Using the same atomic configurations as listed in Table 3.2, collision strengths between levels were calculated and then numerically fit to the van Wyngaarden [76] forms by a least squares procedure for use in the simulation codes. There is no published data for the collision strengths of these ions beyond that also produced by the Cowan codes in [16] and [71] thereby rendering validation impossible. However, a comparison of the data produced for Ne-like Fe with that from [85] and [86] confirmed a general accuracy of better than 50% and rarely worse than 100% for a number of transitions within the $2s^2 2p^6$ to $2s^2 2p^5 3l^1$ (l = s, p & d) levels.

The most important collisional transitions in these schemes are those which directly populate the laser levels. Collision strengths from the ground state to the main laser levels for the three ions are shown in Figure 3.1. These show that only in argon is the upper laser level going to be pumped more strongly from the ground state than the lower over the entire range of energies. This is largely due to the decrease in the binding energy of the valence electrons at higher Z and the energy difference of the levels being pumped. For krypton and xenon, at energies below around 450 eV and 180 eV respectively, the lower laser level will be pumped more strongly than the upper. In these systems, higher electron energies should increase the size of the population inversion. For argon, this situation is reversed. The difference in the collision strengths for the upper and lower levels decreases at higher electron energies and will therefore reduce the size of any inversion formed.

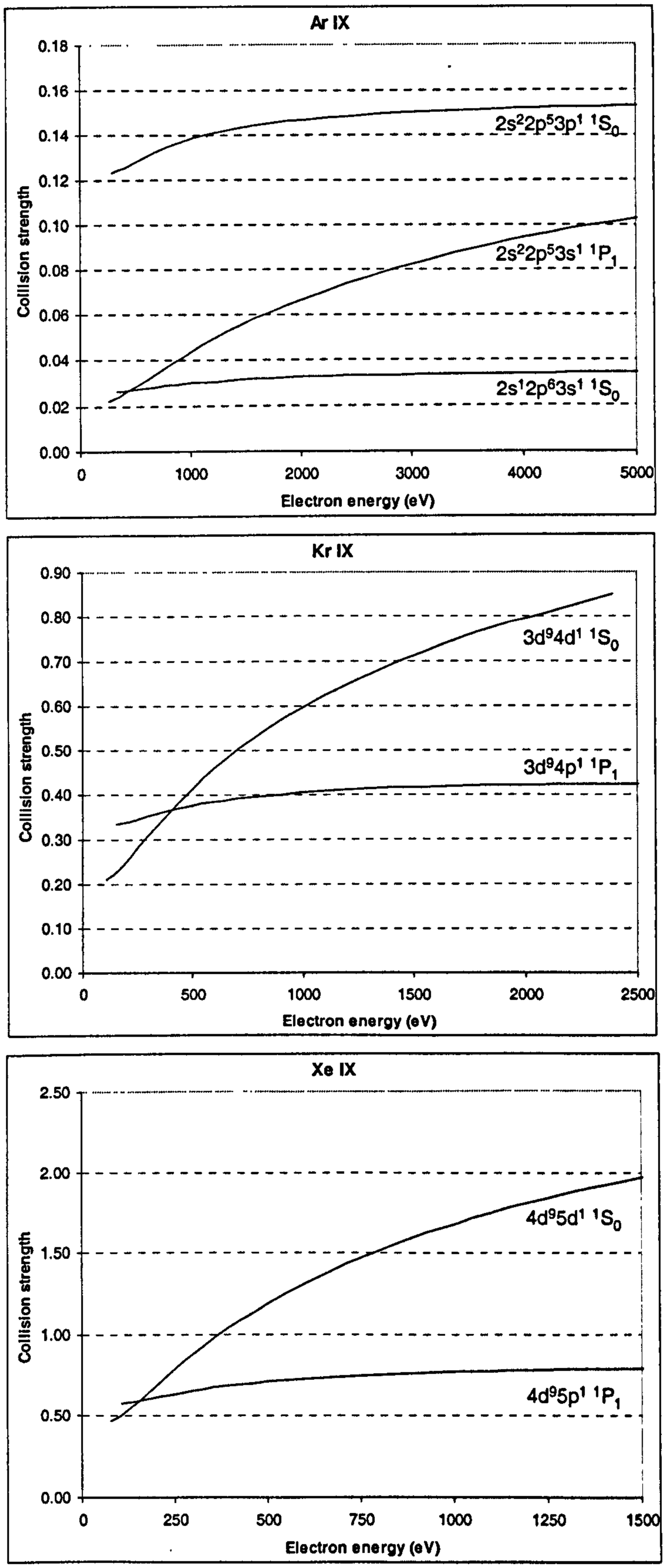

Figure 3.1. Collision strengths from the ground state to the designated laser levels for the three ions.

These collision strengths suggest that it may be desirable to look for ways of manipulating the EED in order to operate in different pumping regimes. However, it should be remembered that in the COLRAD based calculations, it is the net rates into and out of the lasing levels from and to all others which are important in determining the population inversion.

3.6 Conclusions

Atomic energy levels, radiative transition rates and collisional excitation rates have been obtained for the three ions using the computational package of Cowan [68] in order to provide data for the COLRAD routines used by the later simulation codes. A large number of levels in LSJ coupling notation have been calculated approaching the ionisation threshold which should allow for accurate calculations of the lasing ion stage. Comparison of the energy levels with the limited data available implies that the radiative transition rates should also be of good accuracy.

Direct validation of the collision strengths is not possible, however, we expect these to be accurate to within the limits of the plane-wave Born approximation of around 25%. The trends illustrated by the collision strengths from the ground state to the lasing levels would suggest that the upper (valence) lasing level will be more strongly pumped than the lower level at lower electron energies for argon and may therefore allow for increased gain. This is not the case for krypton and xenon where at low energies the collision strength to upper level is smaller than lower.

Chapter 4

Calculations of gain coefficients and output irradiances following OFI

4.1 Introduction

The lack of suitable X-ray mirrors with which to form an amplifying cavity means that large values for the gain coefficients are required for useful X-ray laser schemes. The difficulties involved in forming lasing channels of moderate lengths (which are examined in Chapter 5) along with large electron density gradients within the plasma which will refract any X-ray laser output also imply that large values are necessary. Of equal importance is the output energy of the device which is typically measured in terms of the saturated irradiance of the lasing line. Ideally, irradiances of around at least 10^7 W/cm^2 are required for many of the proposed uses of X-ray lasers.

This chapter examines the gains and output irradiances produced from the three gases in a 1-D time dependant system following OFI using the BREAKDOWN code which is described next. All three systems are examined over a range of ion densities from 10^{17} cm^{-3} to 10^{19} cm^{-3}, the lower limit being set the requirements of large gains and irradiances and the upper by the difficulties in creating plasmas of such densities. Particular emphasis is given to the argon scheme since its simpler atomic level scheme has allowed for a wider range of more detailed calculations to be performed within a reasonable time.

It is assumed in this chapter that a uniform plasma is created by OFI at the focal position of a driving pulse. It is therefore assumed at this point that propagation affects do not prevent the formation of a suitable plasma. This issue is addressed fully in the following chapter on pulse propagation. The pulse in all simulations in this chapter is assumed to be that of a spatially smooth Gaussian profile with a radius of HW($^1/_e$)M 30μm and peak vacuum irradiance of 10^{17} W/cm^2. The pulse duration

is of FWHM 30 fs and a zero to peak rise time of 20 fs. The wavelength used (as throughout the thesis) is 800 nm.

The only previous modelling work of the three systems published for comparison is the seminal paper of Lemoff *et al* [16]. These QSS calculations are limited in that they consider only the transitions within the lasing manifold, that is $n = 3, 4$ & 5 for the argon, krypton and xenon systems respectively. The gains predicted are listed below in Table 4.1.

System	Density (cm^{-3})	Gain (cm^{-1})
Ar IX	1×10^{17}	17
	2×10^{17}	34
Kr IX	2×10^{16}	7.5
	1×10^{17}	94
Xe IX	2×10^{16}	20
	1×10^{17}	107

Table 4.1. Predicted gains for the three systems using the QSS calculations of Lemoff

These predictions are made by calculating the collisional excitation rates assuming that the EED can be approximated by eight delta functions corresponding to the quiver energies of the electrons released by OFI. This is in contrast to the calculations presented in this section which assume a MB distribution with characteristic mean temperature.

4.2 The simulation model, BREAKDOWN

The 1D code used to produce the results in this chapter consists of two parts. The ANALYTIC routines firstly calculate the breakdown of the gas by the driving laser pulse over its radial profile through OFI using the laser cycle averaged rates. ATI and IB heating of the freed electrons is calculated thereby allowing mean electron energies at the end of the pulse to be determined.

At this stage it has been found to be necessary to introduce an arbitrary cut-off in the field strength below which ionisation is not calculated in order to avoid numerical problems. The resulting temporal pulse shape is therefore no longer Gaussian at very

early and very late pulse times and it is therefore expected that there will be some inaccuracy in the determination of the initial electron temperature. The overall ATI energy is strongly dependant on the pulse shape, however the hottest electrons, and the more significant components of the total temperature, are created near the peak of the pulse where the profile is treated as Gaussian.

From an experimental perspective, the sub-picosecond pulses used in these experiments remain poorly characterised and the Gaussian pulses used here represents a typically assumed profile. Furthermore, there are no reliable published measured electron temperatures from OFI of complex multi-stage ions and we therefore ackowledge that there may be errors in this treatment. A more thorough examination of the effects of the pulse profile has not been carried out in this work in light of the lack experimental comparisons available.

The second part of the code subsequently begins by firstly initialising a plasma in which the ions are of a charge state determined by `ANALYTIC` and are at room temperature. The electrons are assumed to be in local thermal equilibrium and are characterised by a MB distribution of $T_e = \frac{2}{3}\bar{\varepsilon}_e$. The hydrodynamics of the plasma are then determined with the thermal conduction of both ions and electrons across the radial mesh. Equilibration between electrons and ions is included. For each radial cell, atomic calculations are performed which determine the change in the ionisation state of the plasma. For specific ion stages, a more complete collisional / radiative analysis may be performed with the `COLRAD` routines thereby allowing lasing parameters to be calculated. For this work, only the lasant ion stage is treated in this manner. The whole system is then numerically integrated in time in a fully consistent manner which allows for energy exchange between the plasma species and the atomic processes.

The radial mesh extends out to 3 times the pulse radius thereby allowing expansion and thermalisation with the cold un-ionised gas. For this work, the large number of atomic states used for calculations by the `COLRAD` routines has resulted in a trade off with the number of radial cells used in order to obtain results in a reasonable time and thus a relatively small number of 75 cells has been used.

4.3 Electron heating mechanisms – ATI vs. IB

Chapter 2 presented theory for the two mechanisms which are responsible for heating electrons by the laser, above threshold ionisation (ATI) and inverse bremsstrahlung (IB) and it is convenient at this point to evaluate the relative importance of the two mechanisms. The ANALYTIC subroutines of BREAKDOWN can be used as a 'stand-alone' package to calculate the mean electron temperature for given laser pulse characteristics.

Table 4.2 shows that IB heating is negligible for the three gases at densities below 10^{19} cm^{-3}. At a density of 10^{19} cm^{-3} IB accounts for only 0.16%, 0.25% and 0.30% of the total energy for argon, krypton and xenon respectively. The increasing significance of this contribution with the atomic number is due to the fact that the electrons are released earlier in the pulse for higher atomic numbers due to their smaller ionisation energies and as a result the ATI energy is smaller.

Although BREAKDOWN calculations are performed at densities of 10^{19} cm^{-3}, the next chapter will show that operating at this density is difficult due to pulse propagation effects. It is therefore the case that the electron temperature can generally be assumed to be entirely due to the ATI heating at the workable densities of up to 10^{18} cm^{-3}.

	Ar IX		Kr IX		Xe IX	
Density (cm^{-3})	$\bar{\varepsilon}_{ATI}$ (eV)	$\bar{\varepsilon}_{IB}$ (eV)	$\bar{\varepsilon}_{ATI}$ (eV)	$\bar{\varepsilon}_{IB}$ (eV)	$\bar{\varepsilon}_{ATI}$ (eV)	$\bar{\varepsilon}_{IB}$ (eV)
10^{17}	1588.13	0.06	1043.47	0.03	608.18	0.02
10^{18}	1588.13	0.25	1043.47	0.24	608.18	0.17
10^{19}	1588.13	2.53	1043.47	2.44	608.18	1.84

Table 4.2. Mean electron energies following OFI of the noble gases showing the ATI and IB contributions. The driving laser is circularly polarised, λ = 800 nm and with $I_{peak} = 10^{17}$ W/cm^2.

4.4 Gain coefficients for the argon lines

4.4.1 Temporal and radial effects

Of considerable importance in understanding the gain from these systems is how they develop in both time and space. Considering for now just a purely circularly polarised driving laser it is necessary to examine how the state of the plasma created from OFI affects the gain produced.

Immediately following OFI of the gas, all the ions will be in the ground state, i.e. $[Be]2p^6$ for argon. Collisional excitation by the free electrons will take time to populate the upper lasing level. In addition there will be excitations to levels above the upper lasing level which will eventually decay radiatively back to the ground state, some of them though the lasing levels and thus also affect the population inversion. Collisional ionisation will also act to remove the lasing ions from the plasma. Finally, the electrons, in transferring energy to the ions will loose energy and eventually cool to the point where they can no longer effectively pump the upper lasing level. It therefore becomes clear that there will be some form of temporal evolution of the gain coefficients which is shown in Figure 4.1.

All three lasing lines show a similar trend in the development of the gain over the two orders of magnitude of density examined in that there is a rapid rise in the gain (rapid in terms of the total duration of the gain) as the population inversion is established followed by a gradual decline from a well defined peak value.

A sudden drop in the value of the gain coefficient is observed at the low density of $10^{17}\,cm^{-3}$ at around 175 ps for the 46.9 nm and 15.7 nm lines and can be attributed to radiative transitions from higher levels which have taken some time to decay ultimately into the lower laser level which is shared by these lines.

By examining the development of the gain alongside that of the electron temperature, T_e, and the ionisation state of the plasma, Z^*, as shown in Figure 4.2 it can be seen that two different mechanisms operate at low and high densities to limit the duration of the gain. At the low density of $10^{17}\,cm^{-3}$ ions within the plasma remain almost completely in the Ar IX stage over durations of several hundreds of picoseconds. The electron temperature however rapidly falls below the 280 eV required to pump

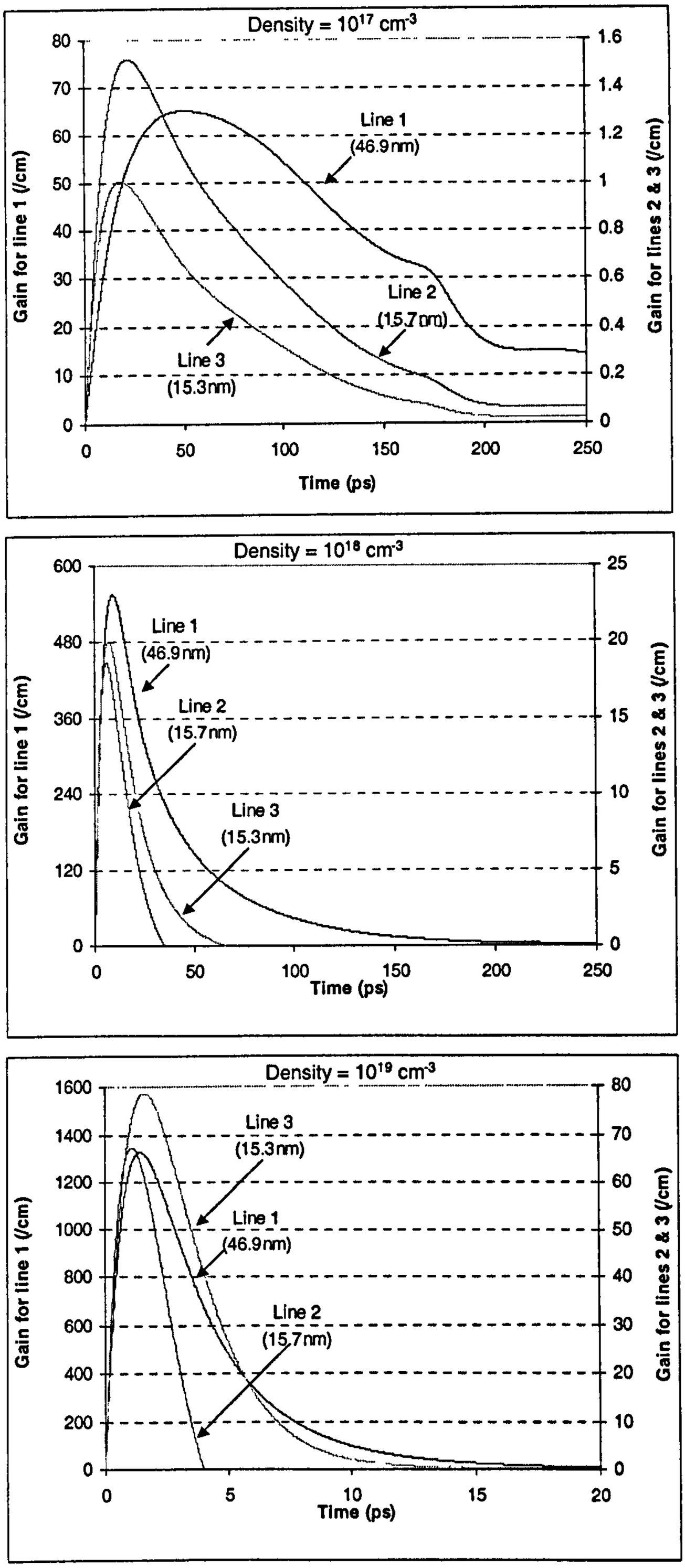

Figure 4.1. Temporal gain profiles for the three lines of Ar IX at ionic densities of 10^{17} cm^{-3}, 10^{18} cm^{-3} and 10^{19} cm^{-3}. Note that the inner shell lines are shown on the second vertical axis of each graph.

the upper level although a small number of electrons in the tail of the thermal MB distribution will provide limited pumping. After this point, population of the upper level can only occur through radiative decays of higher levels which were collisionally populated at earlier times. Evidence of this can be seen in the gain curve of the 46.9 nm line in Figure 4.1. At around 150 ps there is a drop in the rate of decrease of the gain before the sudden drop previously discussed. By 200 ps the value of the gain is nearly constant implying that upper laser level is being populated at the same constant rate as the lower decays. With the electron temperature below 200 eV by this point, collisional pumping will have virtually ceased.

In contrast, the limiting factor on the gains for the densities higher than around $10^{19}\,cm^{-3}$ is that of collisional ionisation. Referring to Figure 4.2 it is seen that at the highest density considered of $10^{19}\ cm^{-3}$, collisional ionisation has so rapidly over ionised the plasma that in less than 10 ps the average ionisation is of Ar X ions. There are therefore very few of the lasant ions available for pumping even though the electron temperature remains high enough to provide modest pumping.

Although collisional excitation of the atomic levels and collisional ionisation are important causes of electron cooling, thereby limiting the pumping duration, the most significant lose of energy is through thermal conduction. The results shown so far are of the region of plasma at the centre of the driving pulse where the peak irradiance allows for the required lasant ion to be created. Moving away from the centre of the pulse the state of the plasma will change as the irradiance falls below that necessary to create the required ion species.

The stepwise nature of the OFI process means that there will be major changes in the plasma state in moving between adjacent regions of ionisation. This is clearly shown in Figure 4.3 for an ion density of $10^{18}\ cm^{-3}$. In addition to the well defined changes in the ionisation state from region to region, there are also large discontinuous changes in the electron temperature. These are very rapidly averaged out through thermal conduction so that although there is initially a very hot region exceeding 1.05 keV of radius 7 μm, within 10 ps this has been replaced by a much cooler region of temperature ~480 eV of radius 25 μm.

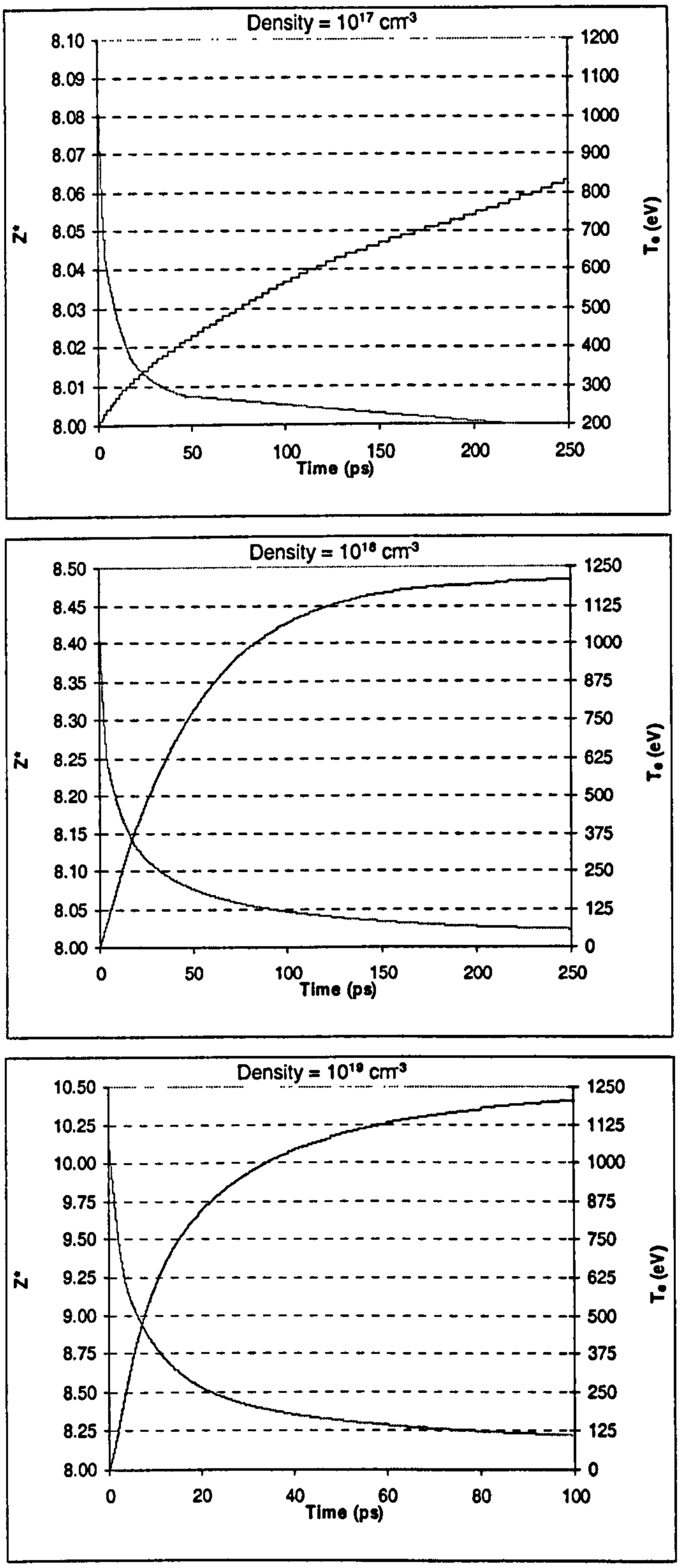

Figure 4.2. Temporal evolution of the average state of ionisation, Z^*, and the electron temperature, T_e, for ionic densities of 10^{17} cm^{-3}, 10^{18} cm^{-3} and 10^{19} cm^{-3}. The coarse nature of the ionisation curve at 10^{17} cm^{-3} is due to the limited number of significant figures output from BREAKDOWN and the narrow range depicted on the graph.

Although this will necessarily limit the gain in the central region of the plasma, it allows for much a larger region of lasant ions to be created by collisional ionisation than that created by the driving laser itself. The development of significant regions of $Z^* \sim 7.5$ at around 10 to 20 ps is clearly shown in Figure 4.3. The combination of thermal conduction and collisional ionisation thereby allow gain to be produced in a larger region of plasma. This is illustrated in Figure 4.4 where it is seen that large gains of around 150 cm^{-1} are produced in the region of plasma that was originally purely Ar VIII following OFI within 20 ps. By around 50 ps gains of around 100 cm^{-1} are produced nearly uniformly up to a radius of around 20 μm.

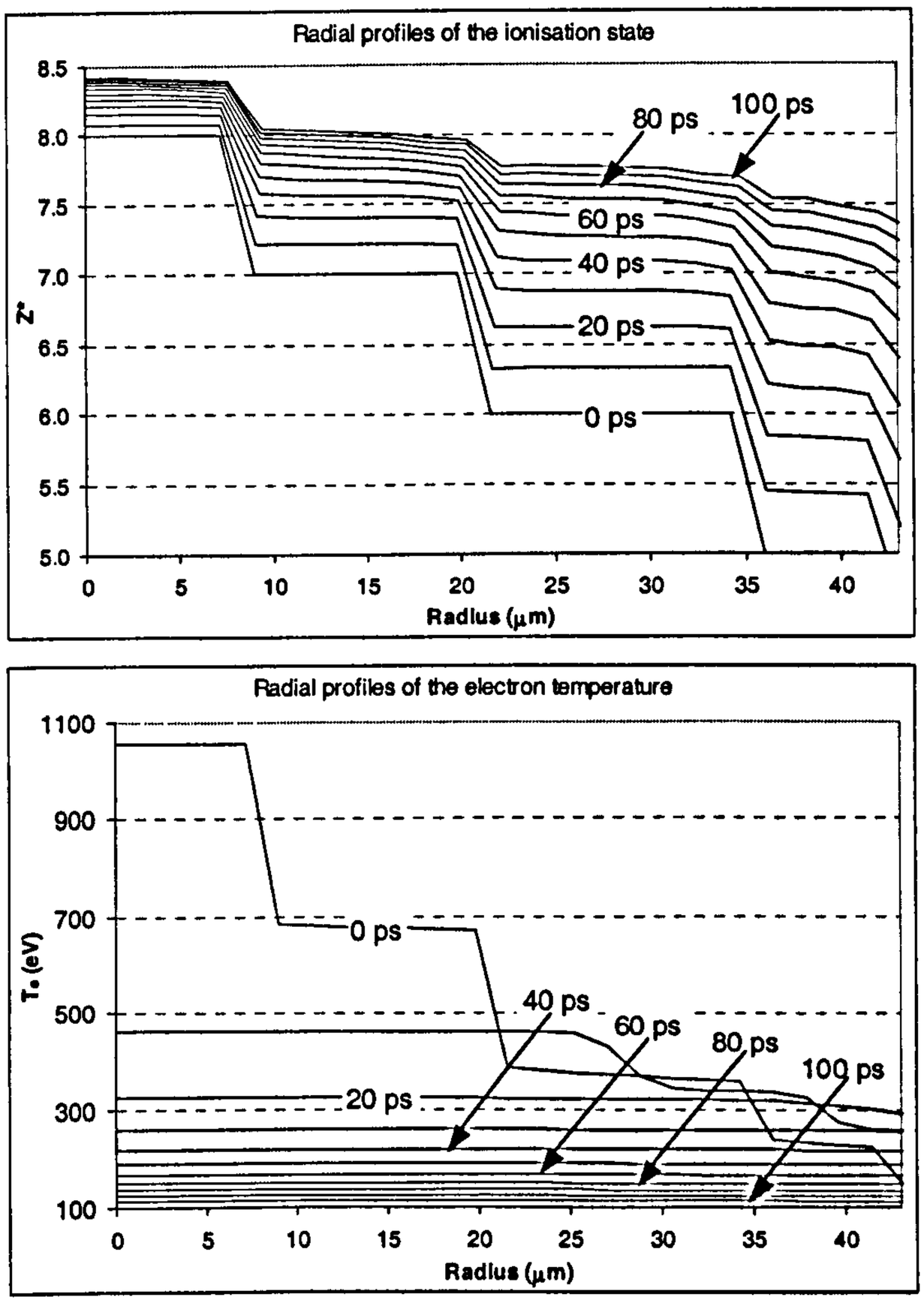

Figure 4.3. Radial profiles of the ionisation state, Z^*, and electron temperature, T_e, for an ion density of 10^{18} cm^{-3}. The bold lines are for the plasma immediately at the end of the OFI pulse at the start of the hydrodynamic calculations. Subsequent lines show 10 ps intervals up to a total time of 100 ps. (Note that as in all BREAKDOWN simulations, although the radial meshes extended beyond 100 μm, the range output to the data files is much less than this in order to limit the size of these files.)

While it is clear that collisional ionisation may allow for larger regions of gain to be produced than from OFI alone, this process may itself create difficulties in observing this practically. Within regions of equal ionisation there are initially no (or very small) electron density gradients with which the X-ray laser beam will be refracted. As collisional ionisation occurs this will change and thus will limit the usefulness of such regions. No attempt has been made in this thesis to examine this problem and it may well warrant future investigation given the potentially large gains predicted here.

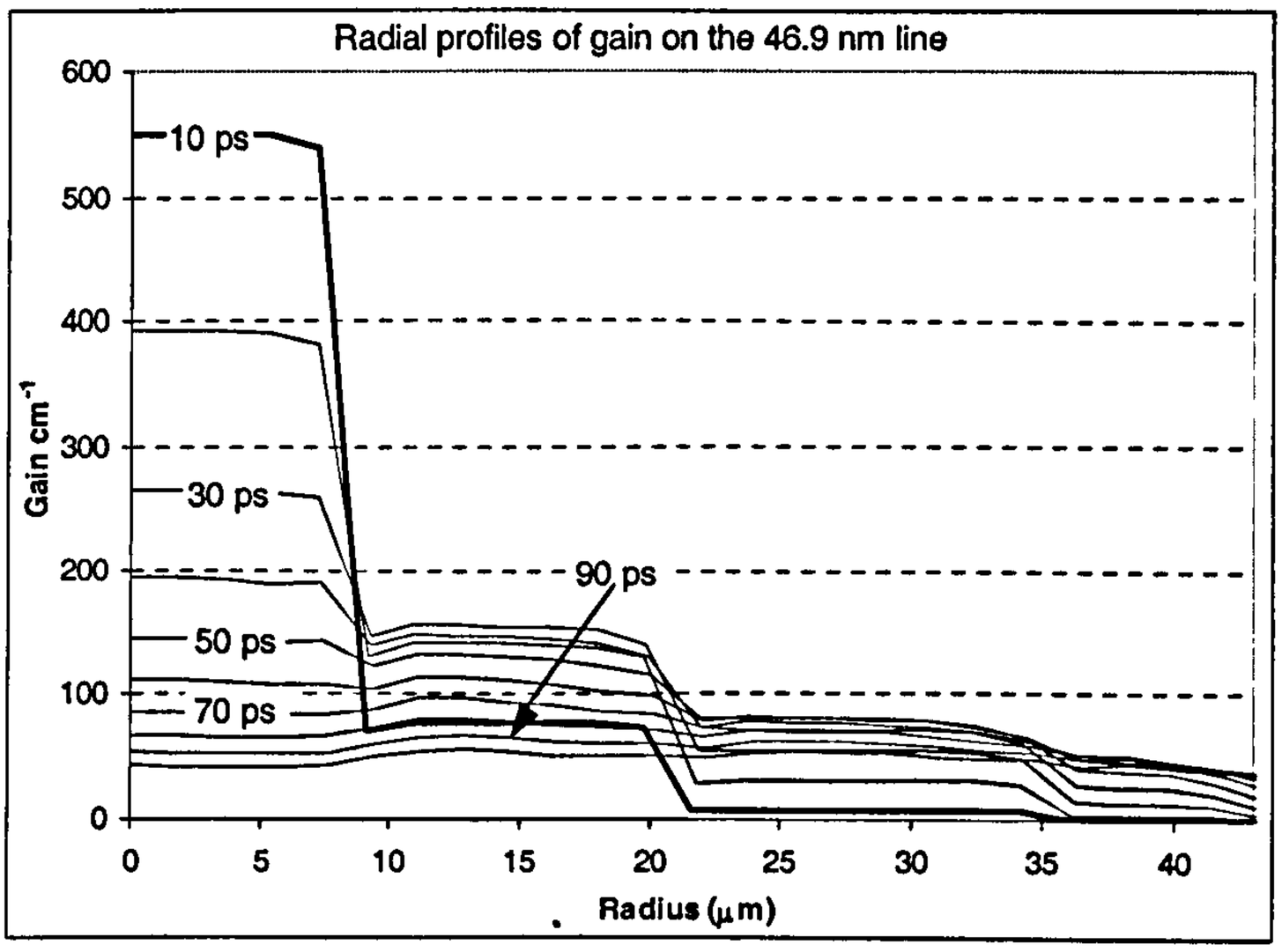

Figure 4.4. Radial profiles of gain on the 46.9 nm line at an ion density of 10^{18} cm^{-3}. The bold line is shown for the first time of 10 ps with the remaining lines at 10 ps intervals showing gain in the central region progressively decreasing.

The temporal and radial gain profiles of the three lines has been presented in some detail, however it often more convenient to simply quote the peak values of gain, particularly when it comes to comparison with the quasi-steady state calculations such as those of Lemoff *et al* [16] listed in Table 4.1. This value is also of use in comparison with experimental measurements where in general only a single estimate of the gain can be made.

From Figure 4.5 it is seen that very large peak gains are predicted for the 46.9 nm line even at low densities which should allow for saturated output to occur in plasma lengths of less than a few millimetres. These results are around 4 times larger than those QSS predictions of Lemoff *et al* [16]. We predict peak gains of 65 and

$140\ cm^{-1}$ at densities of 10^{17} and $2 \times 10^{17}\ cm^{-3}$ respectively compared to 17 and $34\ cm^{-1}$ as listed in Table 4.1. While some of this difference can be attributed to his use of delta functions to determine the collisional excitation rates, the bulk of these larger predict gains is attributable to the complete collisional / radiative treatment of the ion stage which allows the population of the upper level through radiative decays from higher levels. We therefore believe that QSS calculations will tend to underestimate the peak gain available in these systems.

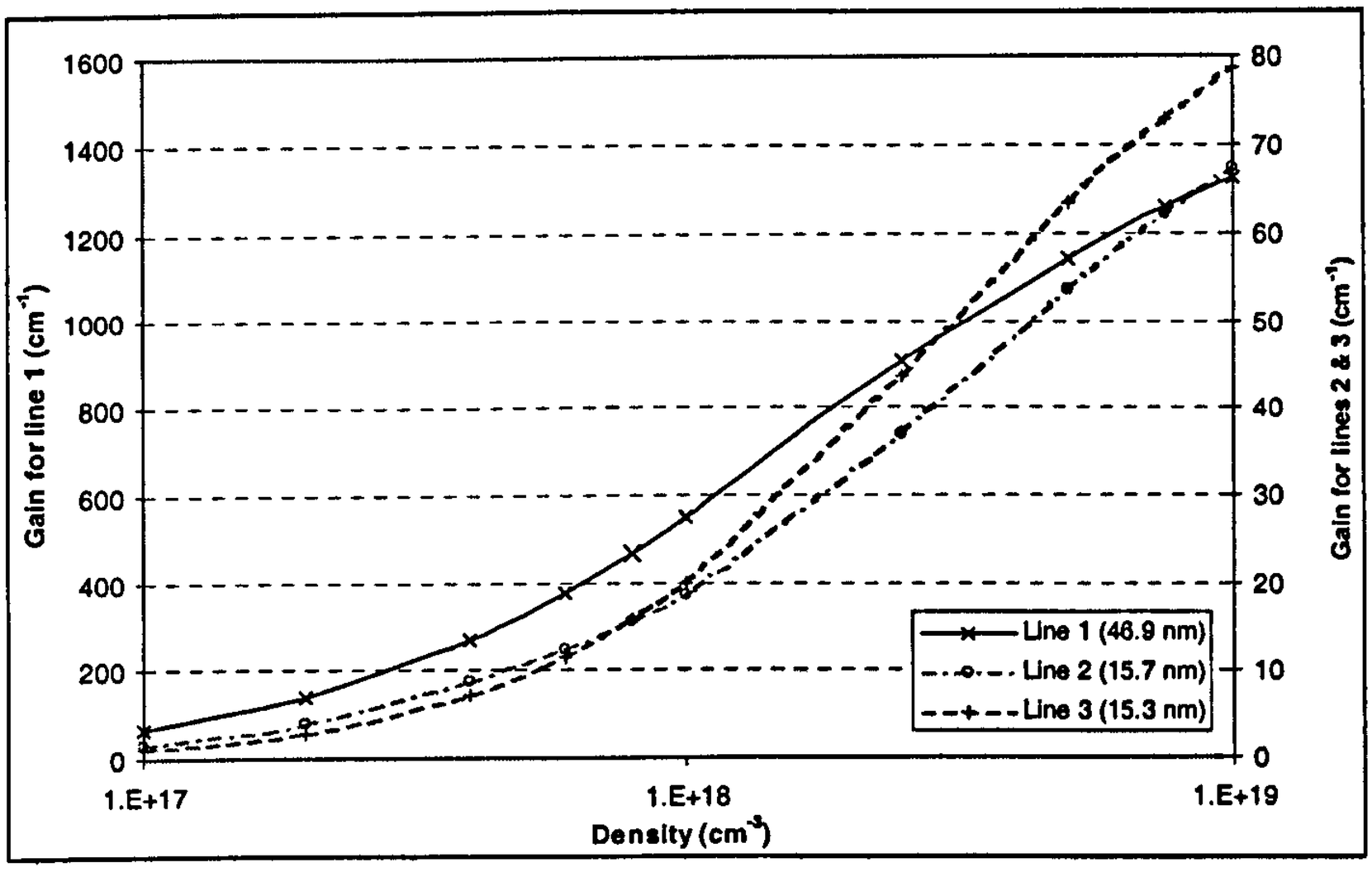

Figure 4.5. Peak gains taken from the centre of the plasma (r = 0 μm) for the three lines in argon over the density range 10^{17} to $10^{19}\ cm^{-3}$. Note that the inner sub-shell lines are shown on the second vertical axis.

The situation for the inner sub-shell lines is less encouraging. The gain from these is around 1 to 2 orders of magnitude less than for the valence shell line reflecting much smaller collision strengths available to excite the inner shell transitions. Densities of at least $10^{18}\ cm^{-3}$ are required to produce useable gains of at least $20\ cm^{-1}$. These values compare with those predicted by Hooker [71] with his QSS calculations of $13.7\ cm^{-1}$ for the 15.7 nm line at a density of $1.5 \times 10^{18}\ cm^{-3}$.

4.4.2 Driving pulse polarisation effects

Section 3.5 presented the collisional excitation cross sections for the main lasing levels and concluded that for each noble gas scheme, the difference in pumping rates between the upper and lower laser levels is greatest at lower energies. Therefore in

order to achieve the maximum population inversion, it may be desirable to cool the electron temperature. ATI heating, as discussed in section 2.3, scales with both the driving laser wavelength and polarisation. However, the wavelength is not practically easily varied at the irradiances needed and we thus consider the effects of changing the driving pulse polarisation from purely circular to varying degrees of elliptical. Figure 4.6 shows the mean electron energy as a function of pulse polarisation as calculated from the ANALYTIC package.

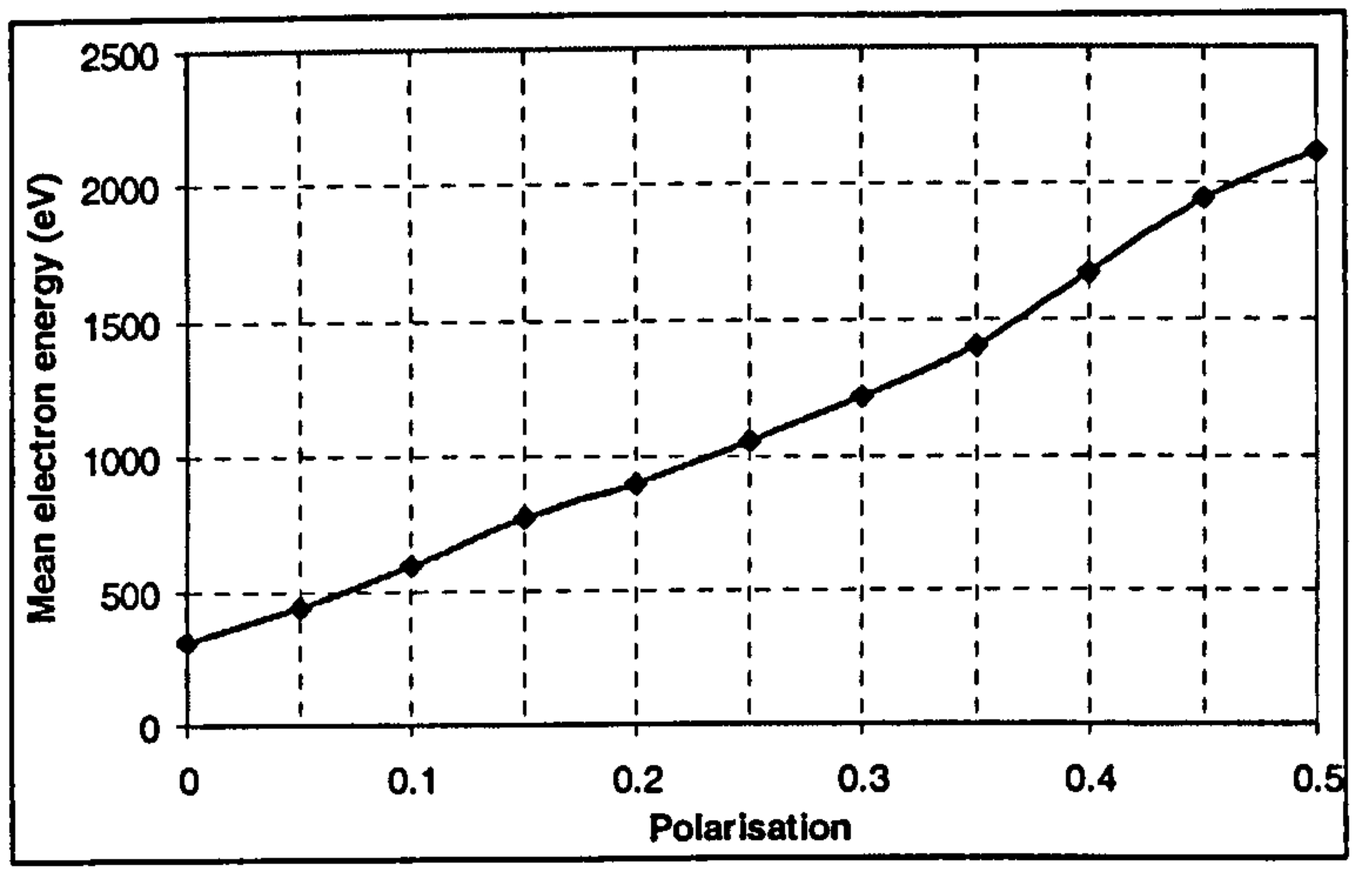

Figure 4.6. The mean electron energy as a function of the polarisation of the driving laser for argon at a density of 10^{18} cm^{-3}.

While the mean electron energy of 318 eV for linearly polarised light would be sufficient to pump the upper level it is clear that there is going to be negligible lasing with such low energies and so we consider only polarisations in the range $0.25 \leq \phi \leq 0.5$.

Calculations were performed for different pulse polarisations over the density range 10^{17} to 10^{18} cm^{-3} and have shown that the maximum gains for each line is obtained with circularly polarised light. This indicates that the complete collisional / radiative treatment involves transitions which outweigh the expected benefit of forming larger population inversions at lower temperatures by considering just those rates from the ground state to the laser levels. It appears that stronger pumping to higher levels by hotter electrons and their subsequent decay to the upper laser level, is more important than the slightly larger inversion we expect to be formed between the laser levels by cooler electrons. This once again illustrates the advantage of a full collisional radiative treatment over QSS calculations.

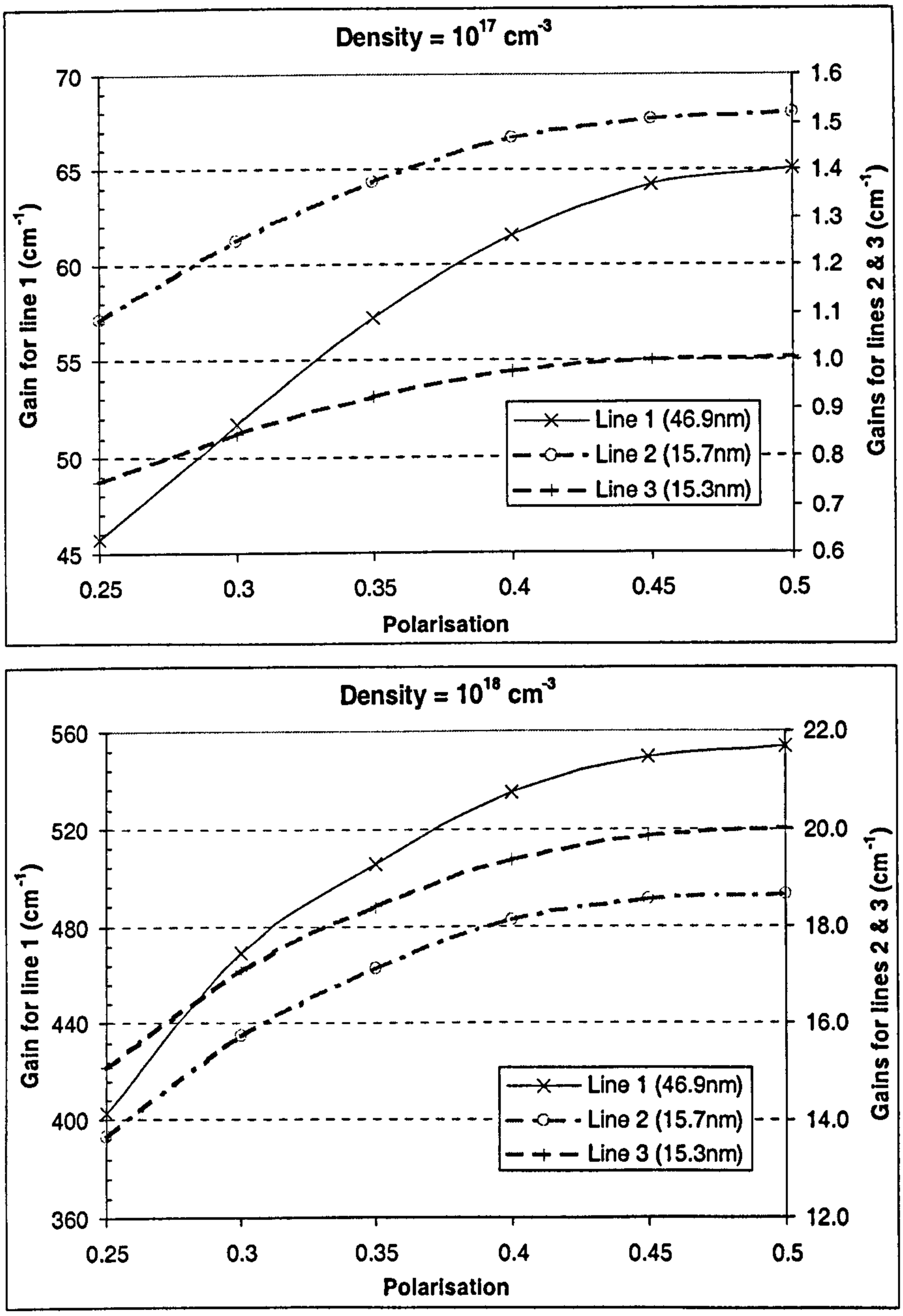

Figure 4.7. Peak gains for the three lines of argon as function of the driving pulse polarisation at densities of 10^{17} and 10^{18} cm^{-3}. Note that the inner-sub shell lines are shown on the second vertical axis.

The lower electron energy at elliptical polarisations inevitably means that the gain duration will be shorter than for circular polarisation, however this does not appear to be a major effect. Temporal profiles of the gain in the 46.9 nm line are shown in Figure 4.8 for three polarisations down to $\phi = 0.3$ and show that even in this case, when the initial electron energy is ~1.2 keV, significant gain continues to be produced up to 60 to 80 ps. For $\phi = 0.4$ the development of the gain is essentially indistinguishable from the circular case.

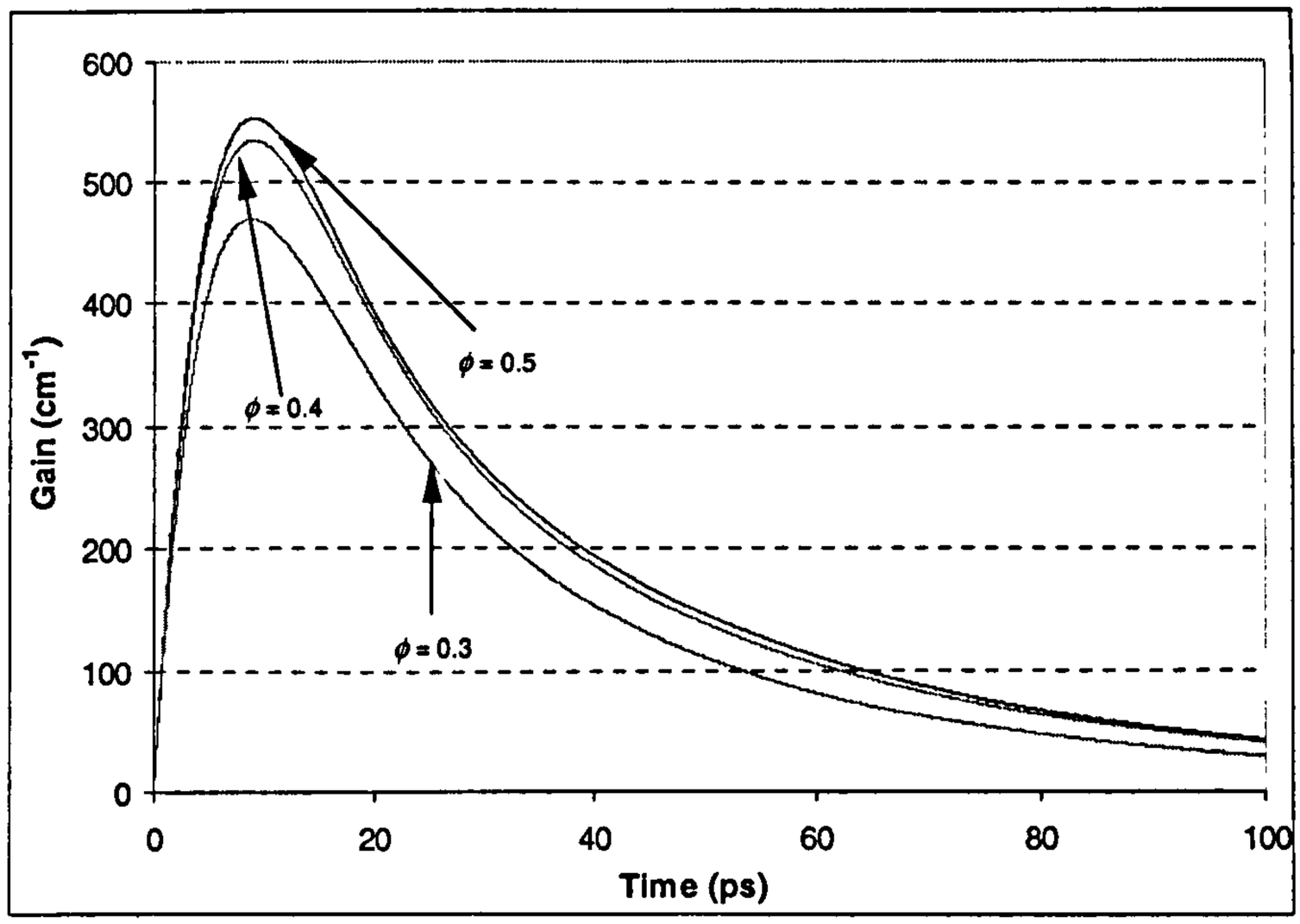

Figure 4.8. Temporal evolution of the gain for the 46.9 nm line in argon at a density of 10^{18} cm^{-1} following driving pulses of polarisations $\phi = 0.5$, 0.4 and 0.3.

While increasing the gain does not appear to be possible, there is an advantage to using a degree of ellipticity in the driving pulse, particularly if some of the large gain (on the valence shell line) can be sacrificed. By moving to elliptically polarised light, a larger diameter channel of the required ion species can be created for a given spot size.

The maximum amplitude of the electric field strength as given by equation (2.11) (that is when $\cos(2\omega t) = -1$) is larger for linearly polarised light than for circular. Thus at any given radius, this larger electric field will allow higher ionisation stages to be produced for linearly polarised fields than for the circular case. The effect is shown in Figure 4.9 for pulse polarisations of $\phi = 0.5$, 0.4, 0.3 and 0.2.

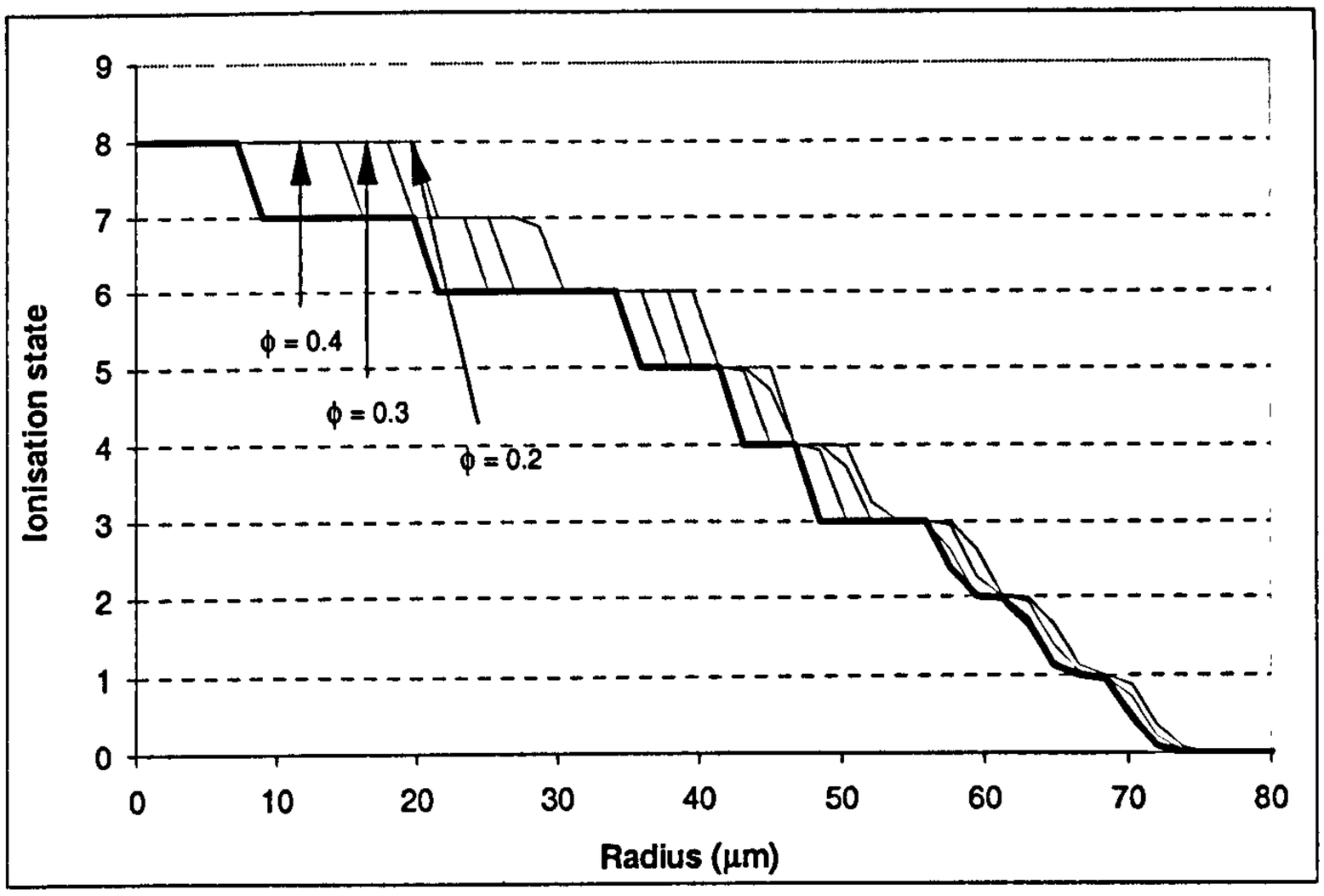

Figure 4.9. Ionisation profiles for argon subject to a pulse of $I_{peak} = 10^{17}$ W/cm^2 of radius HW(1/e)M 30μm for different polarisations. The bold line is for a circularly polarised beam.

For subsequently smaller values of ϕ (that is more elliptically polarised) the region of Ar IX increases. Simply moving to $\phi = 0.4$ doubles the radius of Ar IX produced for an initial peak irradiance of 10^{17} W/cm^2 yet the peak gain is reduced by around only 5% from the circular case. This should enable a much larger amount of energy to be extracted from the X-ray laser for only a small decrease in the gain.

4.5 Saturation irradiances for the argon lines

While large values of gain have been predicted for the valance shell line with much smaller values for the shorter wavelength inner sub-shell lines, for the schemes to be viable, a reasonable amount of energy in the X-ray output must be available. This is most conveniently expressed by the saturation irradiance as presented in section 2.9.2.

Figure 4.10 shows the saturation irradiance for the three argon lines at the time of peak gain over the range of densities examined and it is seen that for the 46.9 nm line is particularly small at only a few times 10^6 W/cm^2 at densities below 10^{18} cm^{-3}. This is a full order of magnitude below the realistic minimum of several 10^7 W/cm^2 that would be needed for any practical application. It may also explain the lack of

observation of this line in OFI X-ray laser experiments (given the provisos of creating the plasma in the first place which is discussed in the next chapter). With such a low irradiance this line may not be easily distinguished from other spontaneous emission from the plasma.

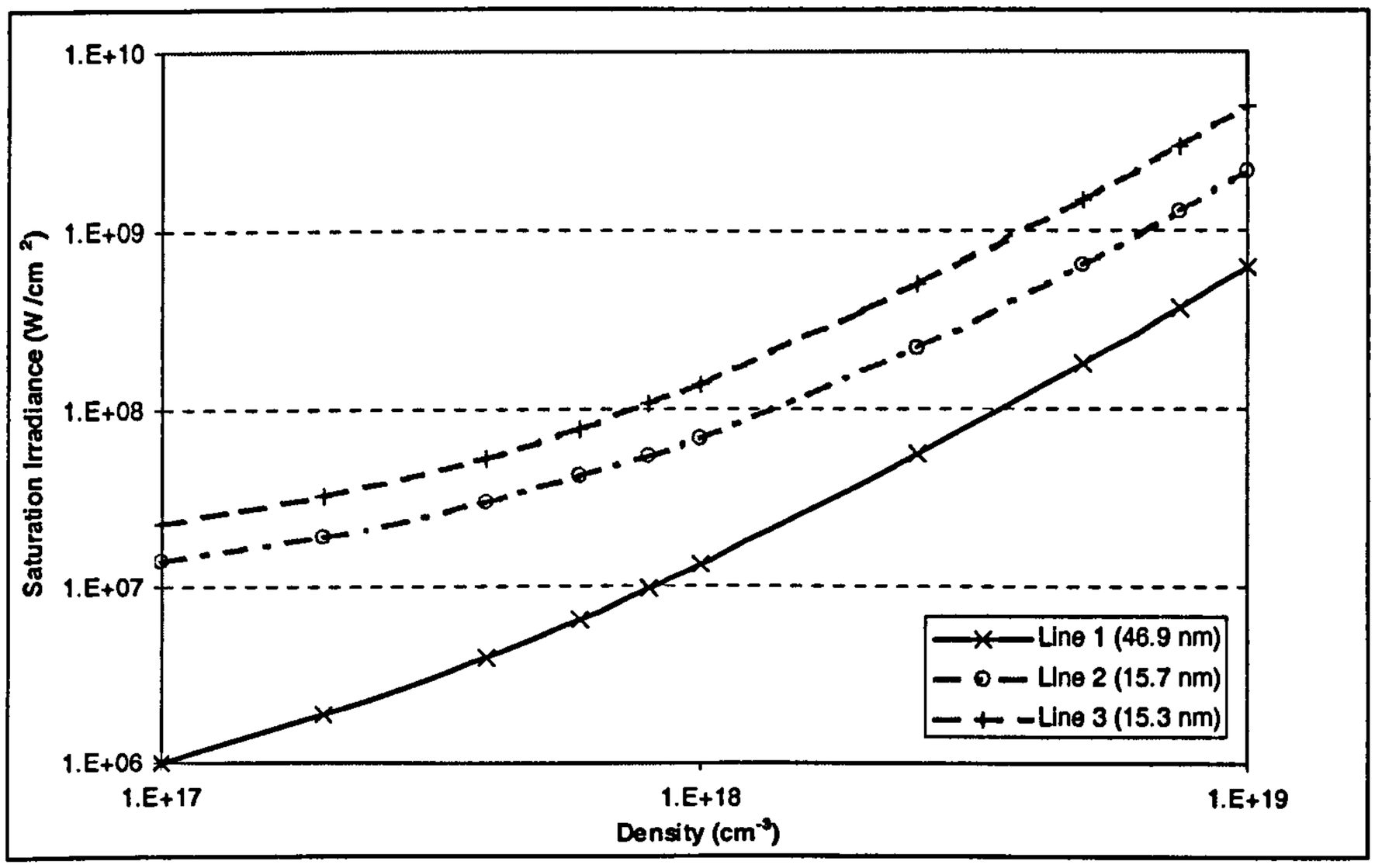

Figure 4.10. Saturation irradiances at the same time as the peak value of the gain for the three argon lines as a function of ionic density.

By eliminating the product $\nu(\omega)A_{21}$ from equations (2.63) and (2.66) it can be readily shown that

$$I_S \propto g(\omega)^{-1} \tag{4.81}$$

We can then see that the low saturated irradiances are at least partly due to the high gains. Examining the equations in section 2.9.2 show that there are few parameters available in order to decrease the gain, only the size of the population inversion (through the gas density) is easily varied experimentally, and reducing this would further reduce both the gain and the saturated irradiance as shown in Figure 4.10. The other parameter which *may* be configurable is the line width function, $\nu(\omega)$, and it is this which is responsible for the high gains. A more detailed discussion on line broadening will be given shortly, however for now it is sufficient to state that the line width function can generally be expressed in terms of a characteristic line width, $\Delta\nu$,

$$\nu(\omega) \propto \Delta\nu^{-1} \tag{4.82}$$

We can therefore conclude that large gains (and hence smaller saturation irradiances) are produced because the lasing transition is of a narrow width.

This effect is also partly responsible for the saturation irradiances of the inner sub-shell lines being approximately an order of magnitude larger for a given density than for the valence line, although it should be noted that the dependence of the stimulated emission cross section, σ_{SE}, on λ^{-2} will act to increase the saturation irradiance. While these saturation irradiances are more encouraging than for the valence line, it must be remembered that in order to achieve saturation, a considerable gain length product of order 10 to 20 cm^{-1} is required and given the lower gains of these lines, a plasma length of around 1 cm must be formed. The next chapter will show that this may not be feasible, particularly at the densities of around 10^{18} cm^{-3}.

4.6 Line broadening effects

The previous section illustrated that the undesirably small saturation irradiances are at least in part due to a narrow line width of the lasing transition. There are a number of important line broadening mechanisms, but the two which prove to be of significance in this work are doppler and collisional. While a thorough discussion of these mechanisms (and others) is given by Hawkes and Latimer [72], the details are briefly outlined here.

4.6.1 Collisional broadening

Atoms in a gas (or ions in a plasma) are subject to collisions between both themselves and free electrons that will perturb the energy levels and thus change the frequency of any emitted radiation. It can be shown that the interaction time is typically of the order of 10^{-13} s compared to the 10^{-11} s involved in the emission process. Thus is it possible to consider collisional broadening of spectral lines as a succession of weak perturbations. It can be shown that the line shape function for collisional broadening, $\nu_C(\omega)$, is of a Lorentzian profile

$$\nu_C(\omega) = \frac{\tau_C}{\pi} \frac{1}{1+(\omega-\omega_0)^2 \tau_C^2} \tag{4.83}$$

where τ_C is the mean time between collisions. For a gas, in which the collisions are elastic, this can be estimated as the particle separation divided by their velocity. For plasma however the dominant process is that of inelastic collisions which requires a more detailed analysis. However, for the illustrative purposes of this analysis this approximation can be used. Thus for a plasma species x [72]

$$\tau_C \sim \left(\frac{2}{3}\right)^{1/2} \frac{(m_x k_B T_x)^{1/2}}{4\pi r^2 P} \sim \frac{1}{\Delta\nu_C} \tag{4.84}$$

where r is the typical interparticle distance and P is the pressure. It can be seen that around the centre of the frequency spread, the line width function approximates to the form of equation (4.82) with a line width $\Delta\nu_C$.

For the purposes of our work, the dominant collisional broadening mechanism is due to the electrons. The ions are essentially left at room temperature (~0.025 eV) by the femtosecond pulse while the electrons are of keV temperatures. Thus the line width due to electron collisions is expected to be several times that of the ions.

From the above equation we therefore expect the line width to increase at high pressures and low temperatures. We would like to operate at high densities in any case in order to create large population inversions. This shows that in doing so the large collisional line width would act to restrict the gain and increase the saturation intensity.

4.6.2 Doppler broadening

Doppler broadening is simply the affect of radiation being emitted by the moving atoms / ions. Since the particles will have a range of velocities there will be a characteristic broadening of the emitted radiation. For the usual case in which the atoms / ions are described by a MB distribution, the broadened profile takes a Gaussian of the form

$$\nu_D(\omega) = \frac{1}{\Delta\nu_D}\left(\frac{\ln 2}{\pi}\right)^{1/2} \exp\left[-\ln 2\left(\frac{\omega-\omega_0}{\Delta\nu_D}\right)^2\right] \tag{4.85}$$

where

$$\Delta\nu_D = 4\omega_0\left(\frac{2k_B T_i}{m_i c^2}\ln 2\right)^{1/2} \tag{4.86}$$

Again, around the line centre, the line width function takes the form of equation (4.82).

4.6.3 Line broadening effects in argon

The previous summary of the line broadening mechanisms was prompted by the predicted low saturated irradiances and the proposal that this was due to a narrow line width. Summarising the expressions for the gain coefficient (2.63) and for the saturation irradiance (2.65) then, around the line centre,

$$g \propto \nu(0)$$
$$I_S \propto \frac{1}{\tau_R \nu(0)} \tag{4.87}$$

If we consider two extremes of density, then at a low density collisional broadening will be insignificant and the line width will be dominated by doppler broadening which is independent of density, i.e. $\Delta\nu \sim$ constant. At higher density collisional broadening will tend to become more important which is dependant upon the ion density, i.e. $\Delta\nu \sim n_i$. In addition, the recovery time of atomic levels scales as the inverse of the collision frequency, thus $\tau_R \sim n_i^{-1}$. Using these simple scaling assumptions with relationships of equations (4.82) and (4.87) then it is possible to identify two distinct regimes of behaviour for the gain and saturation irradiance;

$$\text{At low density} \qquad g \propto n_i \qquad \text{and} \qquad I_S \propto n_i$$
$$\text{At high density} \qquad g \propto \text{const} \qquad \text{and} \qquad I_S \propto n_i^2 \tag{4.88}$$

These two regimes are seen in the argon data already presented, particularly on the peak gain values of the 46.9 nm line shown on Figure 4.5 where the gain appears to be flattening off at densities of around 5×10^{18} cm^{-3}. The effect should be much more visible on graphs of the saturation irradiance given its expected quadratic dependence upon the ionic density. This can be seen at the higher end of the density range for the three lines plotted on Figure 4.10 where they tend to straight lines on the log / log

plot. This is more clearly seen if a fit using the last few data points to a power law of the form $y \propto x^a$. Performing such fits to the last three points at densities of 5×10^{18}, 7.5×10^{18} and 10^{19} cm^{-3} and plotting the resulting lines alongside the irradiance curves more clearly shows the transition towards collisionally dominated broadening.

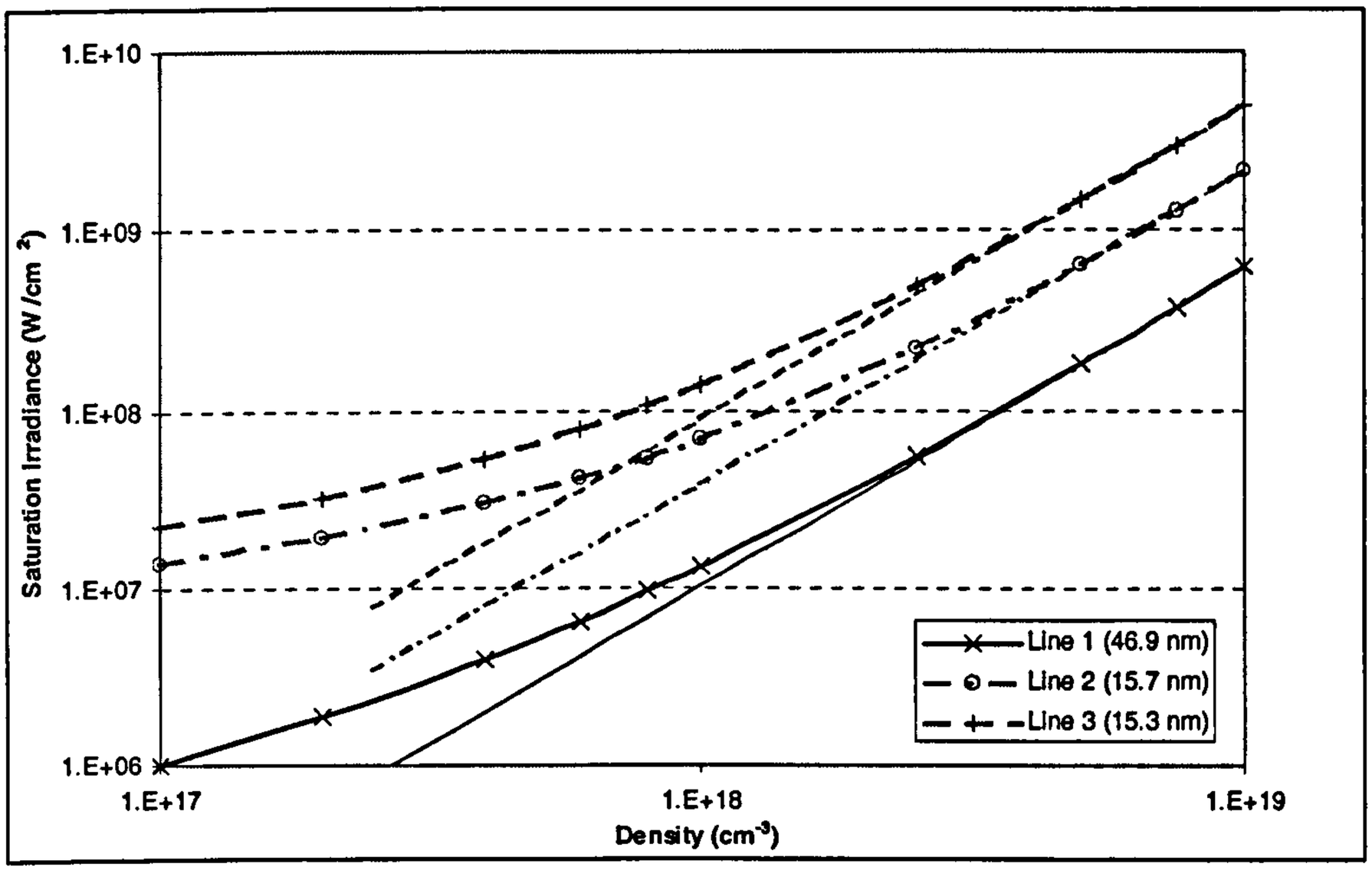

Figure 4.11. Saturated irradiance curves for the three argon lines shown with power law lines fitted to the last three points of each line at densities of 5×10^{18}, 7.5×10^{18} and 10^{19} cm^{-3} illustrating the dominance of collisional broadening of the lines at these densities.

The lines fitted as shown in Figure 4.11 are not exactly quadratic but are of the forms $I_s \propto n_i^{1.78}$, $I_s \propto n_i^{1.74}$ and $I_s \propto n_i^{1.75}$ for the 46.9, 15.7 and 15.3 nm lines respectively. This suggests that the lines are not completely dominated by collisional broadening even at the higher densities.

Electron – ion collisions will act to heat the ions and will therefore increase the doppler line width. However, significant heating does not occur until much later times than that of the peak gain and so can not be considered important as a mechanism for increasing the saturated irradiance around the same time of the maximum gain.

It can now be appreciated that the line widths are the main reason for such differences in the magnitudes of the gain coefficients between solid target collisional systems and these OFI schemes. The much higher electron density of 10^{20} to

10^{22} cm^{-3} enables very strong electron collisional heating such that the ions may be of few hundred eV. This then means that the doppler width is very much larger in this case. The strong heating of the ions means that these are also going to act in collisionally broadening the lines in addition to the electron collisions. Ion collisional broadening is negligible for OFI X-ray lasers.

A more thorough examination of the interactions between different types of broadening mechanisms requires the convolution of the individual line shape functions. This is not a simple procedure given that the two mechanisms examined here are a mixture of homogeneous (collisional) and inhomogeneous (doppler) broadening. The convolution of the two types results in a line shape which is neither Lorentzian (for homogeneous broadening) nor Gaussian (for inhomogeneous) but of a Voigt profile which cannot generally be solved exactly. The work of Pert [75] considers in some detail the various line broadening mechanisms and their effects on the gain and saturated irradiance with particular respect to X-ray lasers.

4.7 Krypton simulations

Simulations were run for krypton over the same density range and pulse conditions as for argon and the same general trends were observed, that is, of large gains and low saturated irradiances.

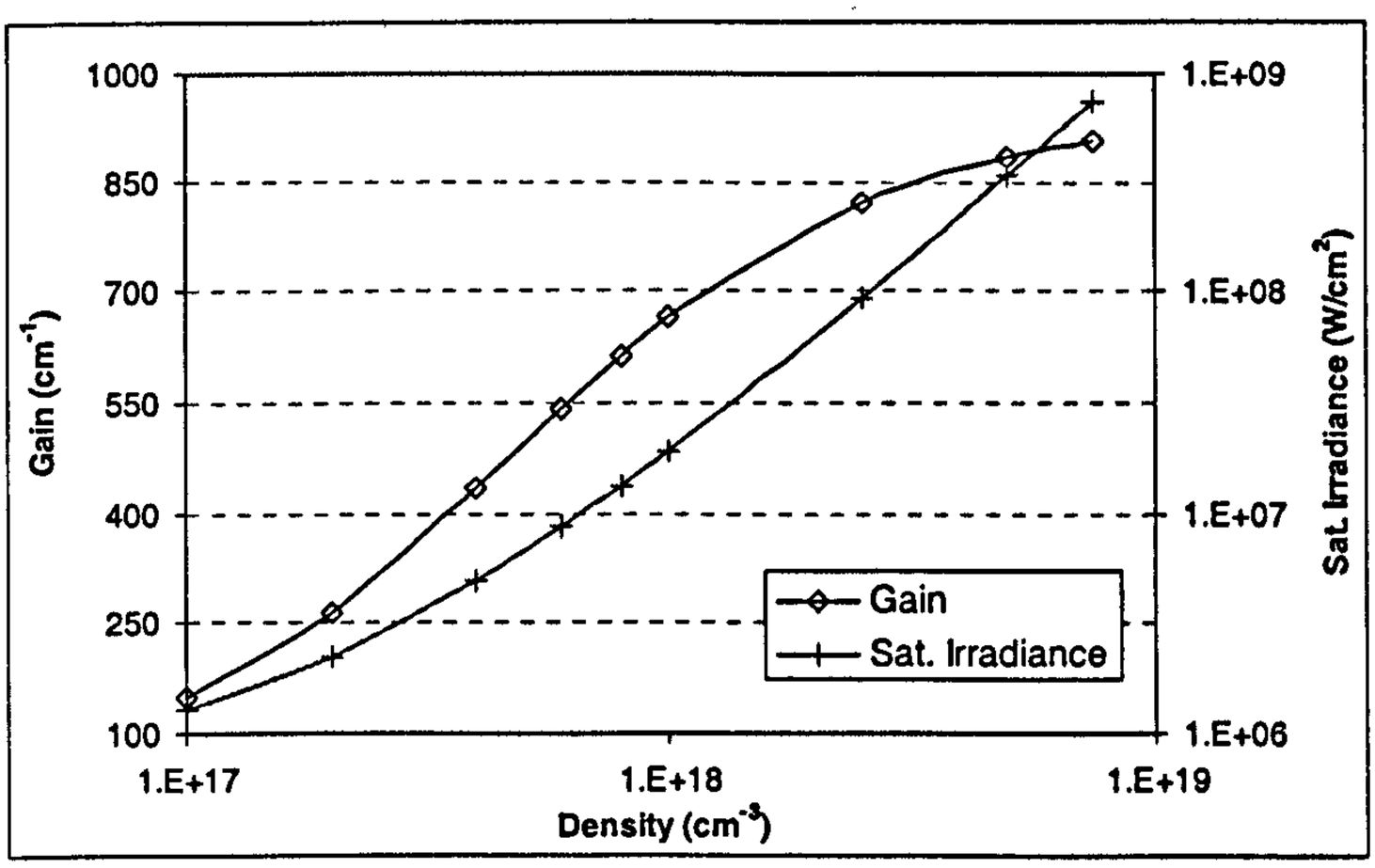

Figure 4.12. Peak gains and saturated irradiances (at time of peak gain) for krypton as function of the ionic density

There is an approximately quadratic (linear on the log / log scale) dependence of the saturation irradiance at the high densities, again indicating that collisional broadening is dominant in this region and that the narrow doppler width is acting to limit the saturation irradiance at low density.

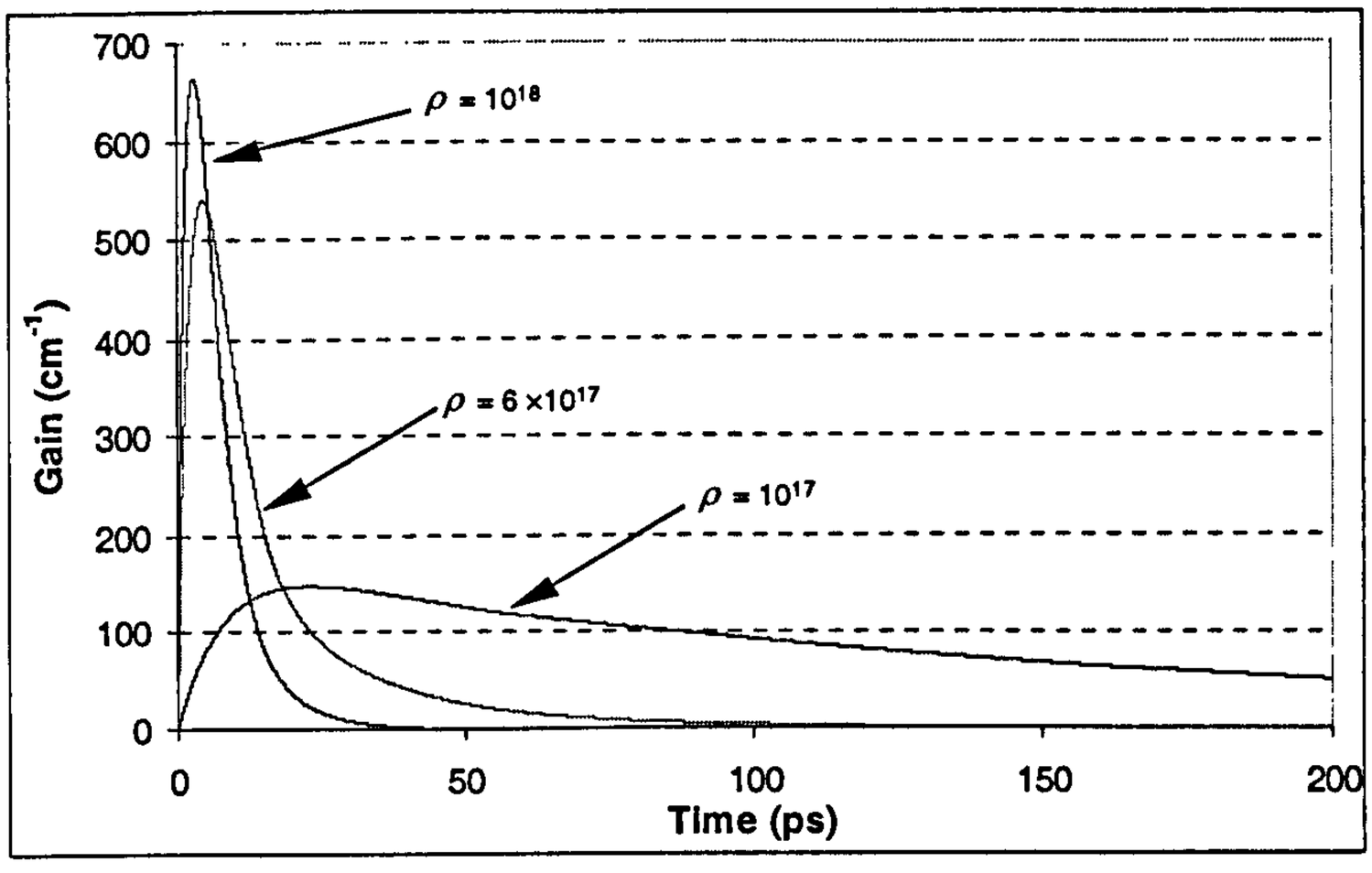

Figure 4.13. Temporal gain profiles at the driving pulse centre for densities of 10^{17}, 6×10^{17} and 10^{18} cm^{-3} for kyrpton.

The temporal evolution of the gain coefficient follows the same trend as the argon lines, however, at the lowest density examined it seen that the gain duration is very long lived with a very small rate of decline. There is still gain of around 50 cm^{-1} at 200 ps (the total length of the simulations) representing about $^1/_3{}^{rd}$ of the peak value. This is because the electron temperature is still sufficiently high enough to effectively pump the upper level, but low enough to lead to a significant reduction in the rate of collisional ionisation. This can be seen in Figure 4.14 where the very rapid drop in electron temperature is due to thermal conduction with the outer regions of the plasma.

The only experimental evidence of lasing in the krypton scheme is that recently of Sebban [20] who has measured a gain of 78 cm^{-1} at a density of 7.7×10^{17} cm^{-3}. This is much lower than the ~500 cm^{-1} obtained from these simulations but allowing for the expected factors of around 2 to 5 in reduction due to refraction of the X-ray output by electron density gradients, this figure is actually in reasonable agreement.

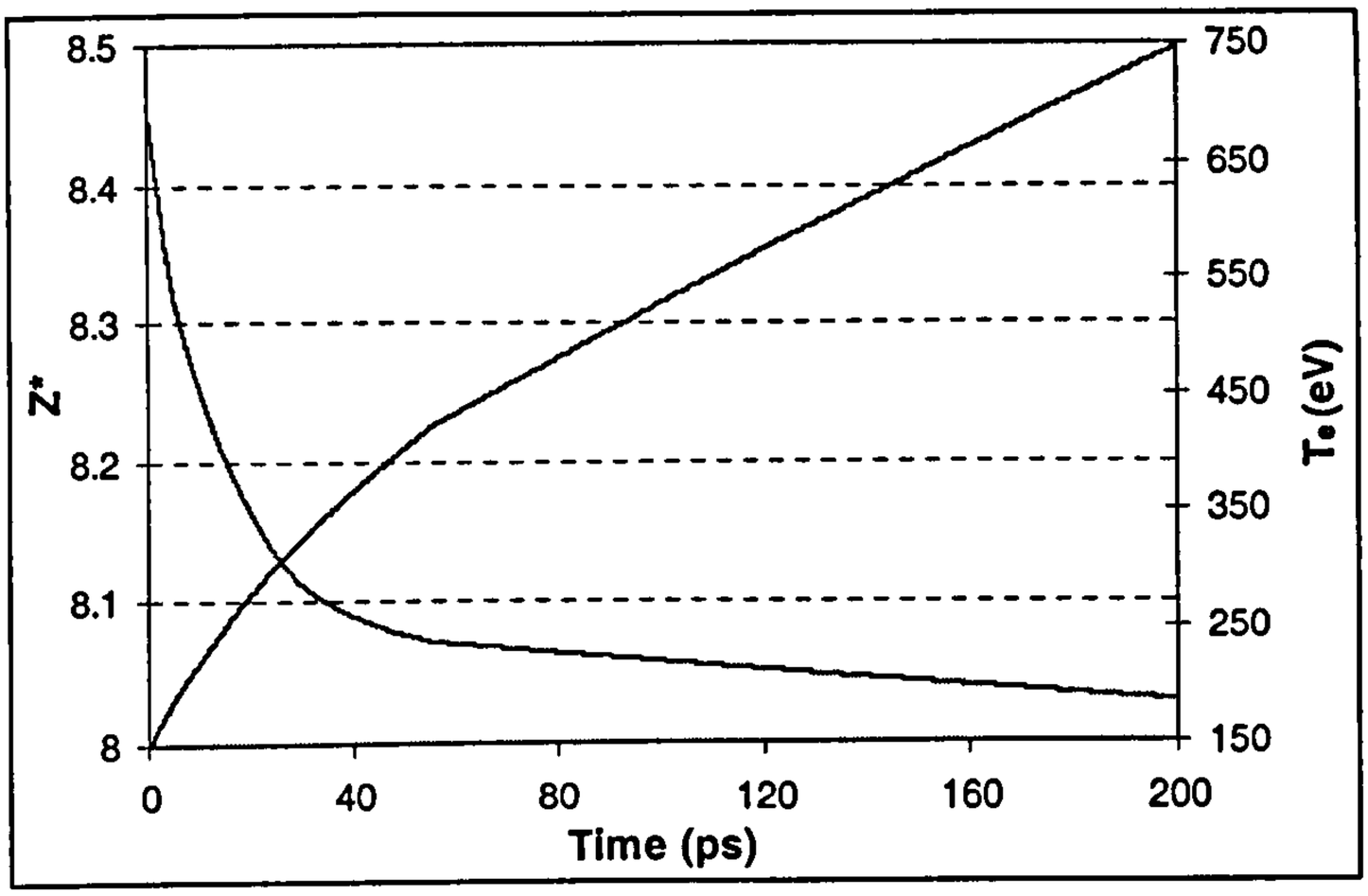

Figure 4.14. Temporal evolution of the average state of ionisation, Z^*, and the electron temperature, T_e, for an ionic density of 10^{17} cm^{-3}.

4.8 Xenon simulations

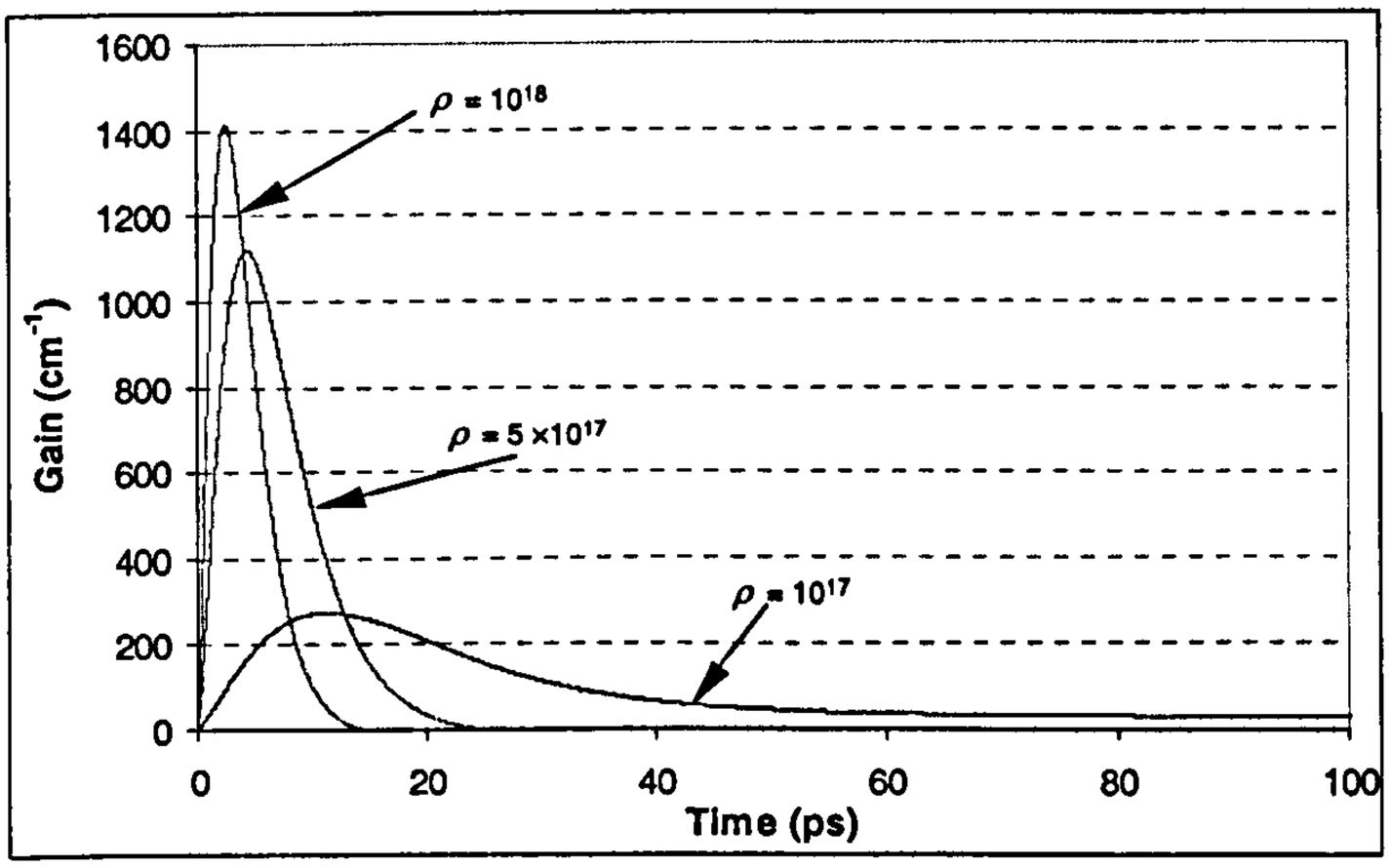

Figure 4.15. Temporal gain profiles at the driving pulse centre for xenon at ion densities of 10^{17}, 5×10^{17} and 10^{18} cm^{-3}.

The BREAKDOWN simulations run for xenon differ from those of argon and krypton in that they have only been run over a density range of 10^{17} to 10^{18} cm^{-3}. Going much beyond this upper value, the hot electrons so rapidly ionise the loosely bound electron (Table 3.1) that over ionisation occurs on time scales of around 1 ps. Simulations indicate that at higher densities, ionisation occurs from the upper states so rapidly that a population inversion cannot be formed and thus no significant lasing

is possible. Figure 4.15 shows that gain has completely ceased at 10^{18} cm^{-3} within around 15 ps. The lower densities again show the long lifetime seen in krypton.

The gains predicted are very large which is again largely a result of the narrow line width due to the small doppler broadening of the heavy xenon ions. Performing the same line broadening analysis for xenon as that for argon in section 4.6.3 shows that over the entire range of densities considered here, collisional broadening is dominant.

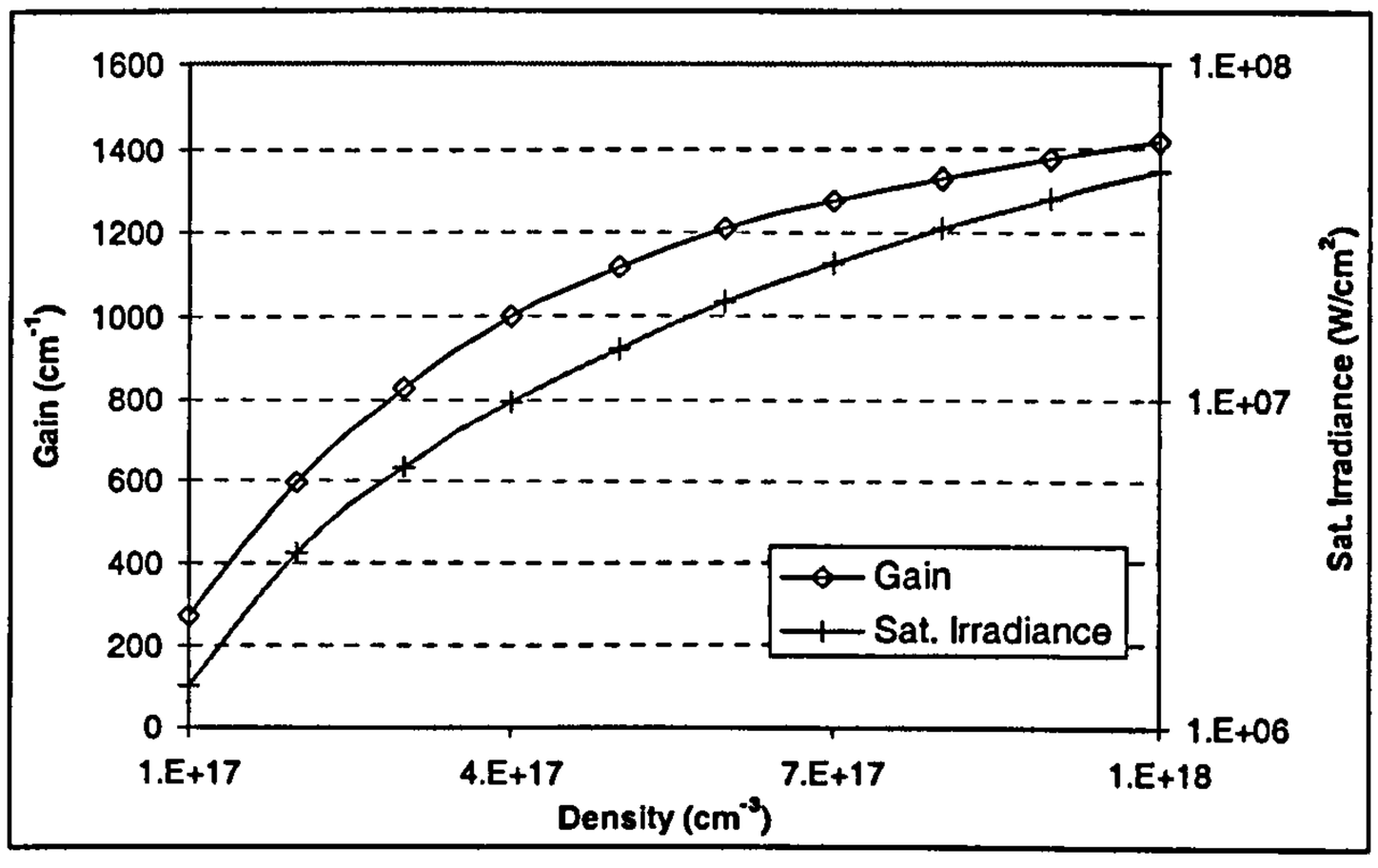

Figure 4.16. Peak gains and saturation irradiances (at peak gain) for 41.8 nm line in xenon. Note that unlike similar graphs for the other gases, the density scale is linear.

These results can be compared with the experimental work of Lemoff *at al* [17] and Balcou *et al* [19] who reported gains of 16.8 ± 0.5 cm^{-1} at a density of 4.7×10^{17} cm^{-3} and 68 cm^{-1} at 5.8×10^{17} cm^{-3} respectively. Both of these are considerably smaller than the ~1000 cm^{-1} predicted by the calculations here and it is unlikely that refraction alone can account for such a large discrepancy as in the case of the krypton.

However, the measured value of the saturated irradiance by Balcou *et al* of 2×10^7 W/cm^2 is, by comparison, in near perfect agreement with the predicted value of 1.95×10^7 W/cm^2 for a density of 6×10^{17} cm^{-3}. A more detailed discussion and comparison of these results will be given later in view of subsequent work.

4.9 X-ray laser output energies

The previous sections in this chapter have shown that lasing with large gains and small saturated irradiances is predicted for all three systems. The total energy emitted by the X-ray laser is given by the integration of the saturation irradiance over the area of lasing and over the duration of the laser action. This then allows an estimate of the efficiency of the schemes to be made. For the driver pulse used in the simulations of this chapter, the energy in the pulse is around 85 mJ.

	Density = 10^{17} cm^{-3}		Density = 10^{18} cm^{-3}	
Laser line	Energy (nJ)	Efficiency	Energy (nJ)	Efficiency
Ar 46.9 nm	3.84	4.5×10^{-8}	109	1.3×10^{-6}
Ar 15.7 nm	29.5	3.5×10^{-7}	150	1.8×10^{-6}
Ar 15.3 nm	72.8	8.6×10^{-7}	356	4.2×10^{-6}
Kr 31.9 nm	5.93	7.0×10^{-8}	22.7	2.7×10^{-7}
Xe 41.8 nm	6.29	7.4×10^{-8}	17	2.0×10^{-7}

Table 4.3. Output energies and conversion efficiencies of the laser lines.

The energies and conversion efficiencies listed in Table 4.3 above are estimated from the BREAKDOWN output by integrating the saturated irradiance from the centre cell to a radius at which no lasing takes place. Thus lasing due to the creation of the lasant ion through collisional ionisation is included. This is integrated over time for as long as lasing in the centre cell continues, i.e. until collisional ionisation results in the termination of lasing at the peak intensity position of the driving pulse. Lasing continues in the outer regions of the plasma for longer periods but is not included since practically this implies an output beam of annular cross section which is unlikely to be of practical use.

The conversion efficiencies are quite low for collisional systems and considering that these listed are ideal theoretical values, the experimental values can be expected to be around an order of magnitude smaller. Those for solid target systems may be around 10^{-6} to 10^{-5} (of the optical laser energy input, not including the considerable inefficiencies involved in generating the optical laser in the first place). The

efficiency may be increased by a factor of two or three by using elliptically polarised light which would create a significantly larger volume of the lasing ion

A point of note is that although the saturated irradiances are largest for xenon and smallest for argon at a given density (for the valence shell lines) the total energy emitted by the X-ray laser is largest for argon. This is due to the stability against collisional ionisation provided by the large ionisation potential of the ion to the next stage which allows for much longer periods of lasing.

4.10 Conclusions

A range of atomic / hydrodynamic simulations for the three gases has been carried out and the temporal and spatial evolution of the gain coefficients and saturation irradiances examined. It is found that the valence shell line for each system is characterised by very large gains of the order ~100 to ~1000 cm^{-1} and small saturated irradiances of around 10^6 to 10^8 W/cm^2 for gas densities in the range 10^{17} to 10^{18} cm^{-3}. The inner sub-shell lines of argon exhibit gains of only a few 10 cm^{-1} although they show larger saturated irradiances of 10^8 to 10^9 W/cm^2.

In all gases, at low densities around 10^{17} cm^{-3}, the gain duration can be long, with considerable gain still produced for times of greater than 100 ps. The initial very rapid growth in the gain is due to the hot electrons which fairly rapidly equilibrate with adjacent regions of plasma where the ionisation state and initial temperatures are lower. The value of the gain coefficient then decreases steadily in line with the electron temperature reflecting the reduced collisional pumping rate. At higher densities, collisional ionisation acts to remove the lasant ion from the regions initially created in the plasma by OFI. However, the same process also creates the required species in adjacent region and can produce regions of useable gain itself. Collisional ionisation is most restrictive in xenon which also shows the lowest overall conversion efficiencies at higher densities.

The low values of the saturation irradiance are largely attributable to the very narrow line widths associated with the lasing transitions. At low densities doppler broadening dominates and since the ions are left cold due to the short duration of the driving pulse, the line width and hence saturation irradiance are small. At higher densities collisional broadening dominates. High densities naturally create large gains and saturated irradiances through the stronger collisional pumping of the levels, however the densities are still relatively low compared to solid target systems and the line width is still narrow enough to limit the saturated irradiance.

Changing the driving pulse polarisation from circular to slightly elliptical and thereby reducing the electron temperature does not increase the gain as might be expected given the behaviour of the collision strengths from the ground to laser levels as discussed in section 3.5. However, this may be advantageous given that a lower gain should result in a larger saturated irradiances and hence output energies.

Using an elliptically polarised driving laser can significantly increase the volume of lasant ions produced.

Finally, comparisons of the gain coefficients has been made with the limited experimental data and found to be considerably greater than those measured. The krypton is expected to be in reasonable agreement given that no refractive effects of either the driving pulse or the X-ray output have been considered at this point. The xenon gains are larger still than those measured and a more complete comparison will be made in light of the driving pulse propagation simulations presented in the next chapter. The peak gains are found to be larger than those predicted by Lemoff *at al* [16] by factors of approximately 32, 7 and 13 for argon (valence line), krypton and xenon respectively. This considerable discrepancy is expected to be due to the difference between his QSS calculations and our more complete collisional / radiative treatment which includes high lying states which approach the ionisation limit.

Chapter 5

Simulations of the driving pulse

5.1 Introduction

The previous chapter investigated the gain and saturated output of the laser schemes and concluded that strong lasing was present on the outer shell lines for significant lengths of time. Lasing on the shorter wavelength lines of the inner shell transitions was only significant at atomic densities of greater than 10^{18} cm^{-3}. These calculations were performed on the *a priori* assumption that the plasma could be formed in the first place. This should be by no means a forgone conclusion.

Unlike solid target systems in which the driving laser is focussed tangentially into a strip a few mm long onto the target, the power requirements and restrictions of the OFI schemes require that the pulse be driven longitudinally into the gas. Since one would ideally require plasma channels of many mm to be formed in order to produce a reasonable gain region, the question of propagation and refraction of the driving beam becomes an important consideration.

Much of the work in this chapter is similar to chapter 5 of Grout [33] and of Grout *et al* [73] who looked at the propagation of driving pulses into gases for OFI recombination schemes. He found that propagation and the subsequent formation of the plasma channel posed no significant problems. However, for collisional schemes the situation is less clear because of the longer wavelength of the driving laser (800 nm as used throughout this thesis compared to the 248 nm in [17]). The problem is simply illustrated given that the refractive index of a medium scales as λ^2. Thus it is expected that refraction of the driving pulse for the case of collisional systems is around 10 times more significant than for the recombination schemes therefore warranting a new investigation.

This chapter is devoted to investigating the propagation effects of the driving laser into the initially neutral gas in order to form the plasma channel. Firstly the computational model, PROPAGATE, is described which is essentially unchanged from that used in [17] and [73]. Work is then presented which models the propagation of the laser beam into the noble gases and the problems observed are discussed. Finally, a novel approach to the solution of propagating the driving beam through the use of parabolic wave guides is discussed and results of such simulations presented.

5.2 The computational model PROPAGATE

The computational code PROPAGATE simulates the time dependent propagation of the driving pulse in a 3D cylindrically symmetric geometry and has been developed from that described by Rae [96]. The pulse is assumed to be initially spatially and temporally of Gaussian profiles and is modelled by the solution of the paraxial wave equation in cylindrical geometry as it travels through the initially neutral gas. The pulse may be arbitrarily polarised although the computational demands involved in calculating the tunnelling rate for elliptic polarisation over the entire domain of the pulse have restricted the investigation in this chapter to purely circular polarisation. OFI of the gas is determined from the rate equation (2.12) thereby allowing the ionisation profile to be determined and its refraction effects upon the beam via the refractive index given by equation (2.40). The mean electron temperature of the plasma is calculated from ATI and IB effects using the same ANALYTIC package as used by BREAKDOWN.

A slice of gas/plasma is modelled in the propagation/radial plane of the beam with the radial direction about the beam centre assumed azimuthally symmetric. The shape of the pulse itself is followed in its own frame with a separate mesh which travels along the plasma mesh. The long wavelength of 800nm used means that significant refraction is expected and as such care must be taken to ensure that the radial size of the two meshes is sufficient to prevent non-physical reflective effects at the outer limit. To mitigate against this, the radial mesh is defined using half of the available cells to be of regular spacing at distances up to $^4/_3 w_{1/e}$ where $w_{1/e}$ is the

radius of the beam where its irradiance has declined by e times its peak vacuum irradiance. Beyond this point the remaining half of the grid points have a spacing that increases quadratically. Simulations trace the pulse from a vacuum position outside the gas across a sharp vacuum/gas interface, through to the ideal focal position at z = 0 mm and out to a vacuum position on the opposite side. Hydrodynamic effects within the plasma are assumed to be insignificant on the femtosecond timescales of propagation and are not calculated.

5.3 Propagation into the noble gases

The examination of pulse propagation into the pure noble gases was performed using 250 cells radially with the uniform spacing of 0.4 μm extending up to just under 40 μm thus allowing an accurate determination of the pulse over the region where the required ionisation is expected to be created. Beyond this point, the mesh extended quadratically up to a total radius of 115 μm. A large number of cells, 400, was used to describe the propagation axis of the pulse since the refraction due to the long wavelength tends to rapidly disperse the pulse and can cause non-physical numerical effects if a much smaller mesh is used. The pulse used is of the same parameters for that used in the BREAKDOWN simulations in the previous chapter, that is, λ = 800 nm, ϕ = ½, radius HW($^1/_e$)M = 30 μm and of duration HWHM = 30 fs. The Rayleigh length for this pulse is therefore around 3.5 mm. These spatial characteristics would require that the beam be focussed with an angle of around 0.12° into the focal position experimentally. The peak vacuum irradiance is varied from the 10^{17} W/cm^2 previously used and is quoted where different.

5.3.1 Argon targets

Of the three gases examined, Ar IX is the most difficult to create given its larger ionisation potential than the other gases. The detailed examination of the lasing line schemes for the gas presented in the previous chapter was done on the assumption that Ar IX could be produced with an incident peak pulse irradiance of 10^{17} W/cm^2.

The OFI calculations in BREAKDOWN show that in the 1-D radial direction of the pulse, Ar IX can be produced up to a radius of around 7 – 8 μm. Figure 5.1 clearly illustrates that this irradiance is insufficient to create any useable volume of Ar IX at the lowest examined density of 10^{17} cm^{-3}.

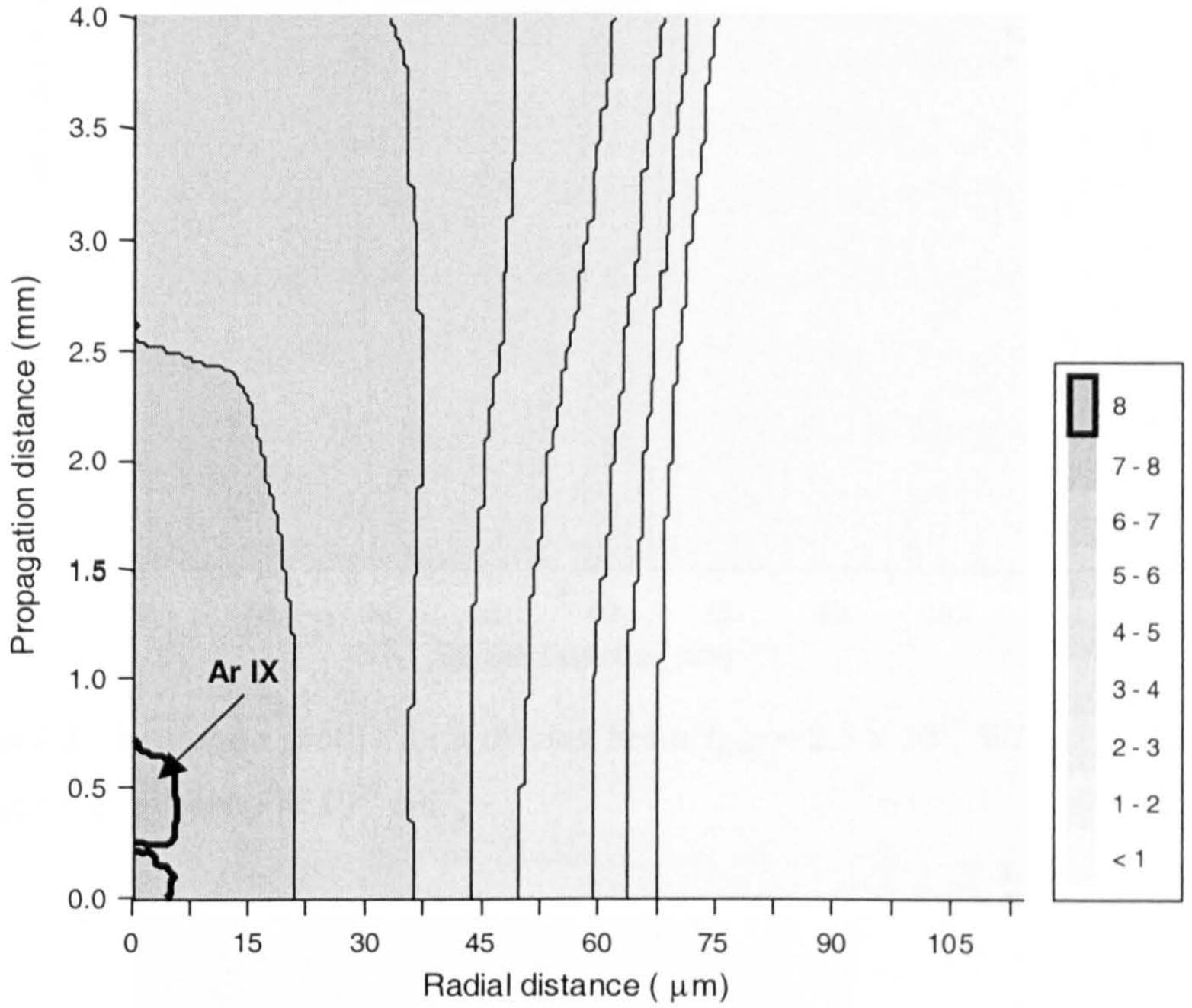

Figure 5.1. Ionisation profile for a driving beam $I_{peak} = 10^{17}$ W/cm^2 propagating into argon at a density of 10^{17} cm^{-3}.

Only by increasing the irradiance to 2.5×10^{17} W/cm^2 as shown in Figure 5.2 is a reasonable channel formed and even at this irradiance, refraction is restricting this channel to not much longer than 4mm in total length.

While increasing the diving pulse peak irradiance to a few times 10^{17} W/cm^2 is no longer a technological difficulty, the results from the previous chapter have shown that it will be necessary to operate these schemes at much high densities than the 10^{17} cm^{-3} and that 10^{18} cm^{-3} is a more realistic minimum. Propagation of a beam of peak irradiance 2.5×10^{17} W/cm^2 into argon at a density of 10^{18} cm^{-3} is shown in Figure 5.3 and shows that at this density ionisation induced refraction of the beam is causing significant beam break up. In this case an irregular channel of around 15 μm in radius and no more than 1.5 mm in length is formed.

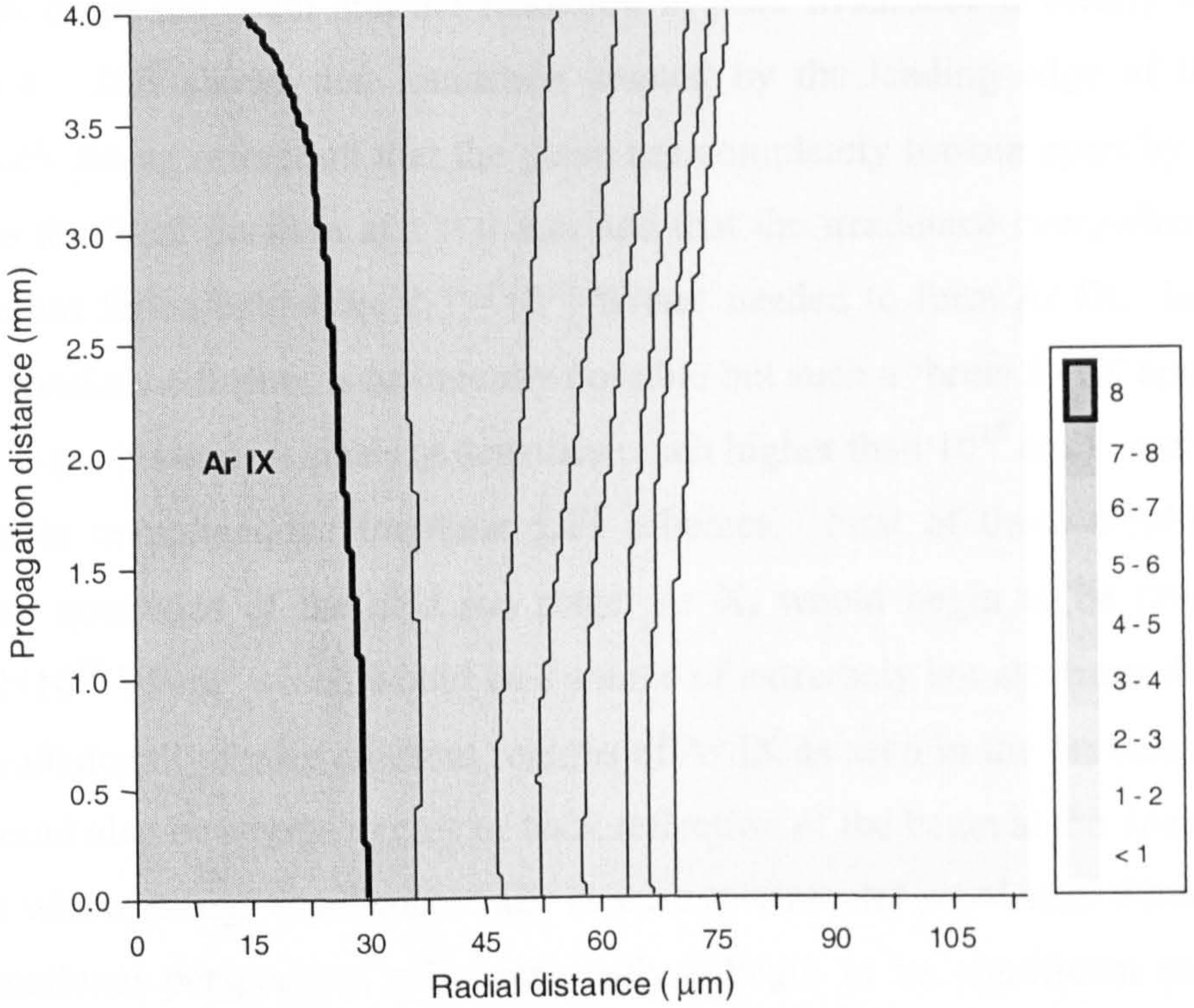

Figure 5.2. Ionisation profile for a driving beam $I_{peak} = 2.5 \times 10^{17}$ W/cm^2 propagating into argon at a density of 10^{17} cm^{-3}.

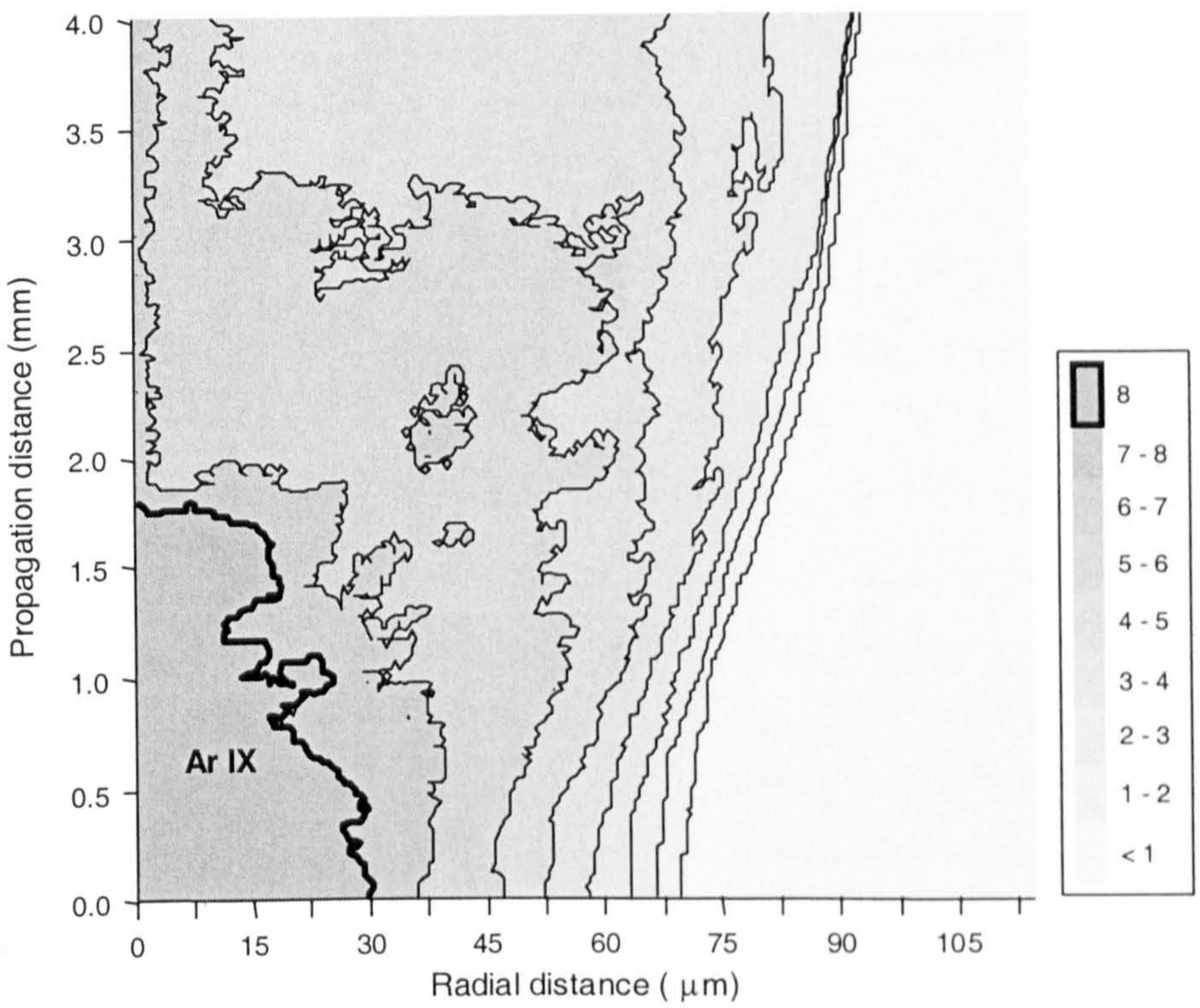

Figure 5.3. Ionisation profile for a driving beam $I_{peak} = 2.5 \times 10^{17}$ W/cm^2 propagating into argon at a density of 10^{18} cm^{-3}.

The break up of the beam and the reduction in peak irradiance is clearly shown in Figure 5.4. This shows that ionisation created by the leading edge of the pulse causes such strong refraction that the pulse has completely broken apart by the time it reaches the focal position at $z = 0$ mm and that the irradiance everywhere within the pulse has fallen below the 2.7×10^{16} W/cm^2 needed to form Ar IX. Increasing the peak irradiance further is technically possible but such a 'brute force' approach to creating larger plasma channels at densities much higher than 10^{18} cm^{-3} would lead to considerable complications for these OFI schemes. First of these would be that significant quantities of the next ion stage, Ar X, would begin to be produced at around 2×10^{18} W/cm^2 which would be a source of extremely hot electrons that would rapidly collisionally ionise adjacent regions of Ar IX as seen in the previous chapter. There would also be a large degree of back reflection of the beam at the vacuum / gas interface which at high irradiances may cause experimental problems. Finally, from a computational perspective, relativistic effects begin to be significant and would require a much more detailed model than used here.

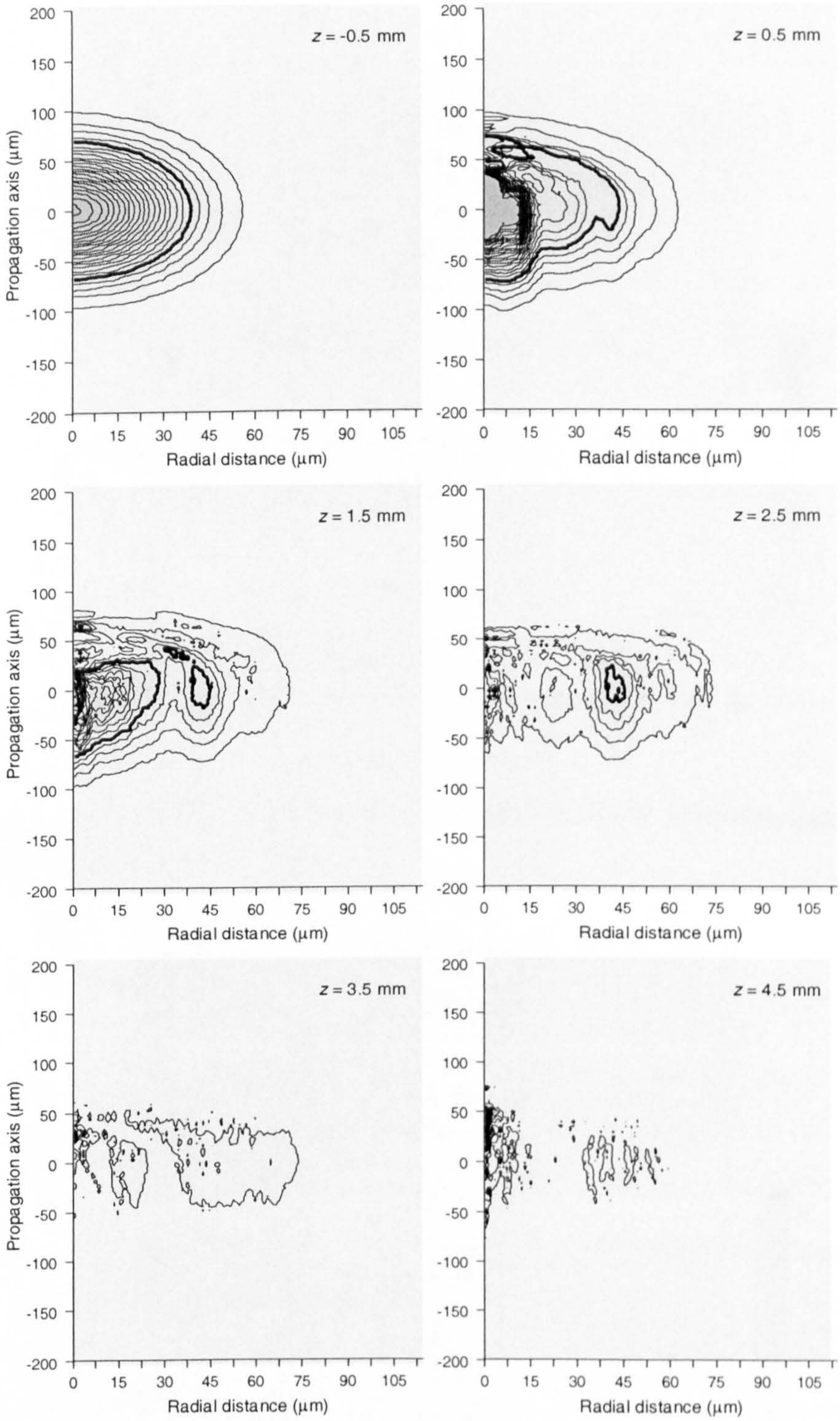

Figure 5.4. Irradiance contour plots for a pulse of initial peak irradiance of 2.5×10^{17} W/cm^2 propagating into Ar of density 10^{18} cm^{-3} (same case as in Figure 5.3). Plots are labelled showing the position of the centre of the pulse (0 μm on the propagation axis) with respect to its position within the plasma. Thus the first plot is the vacuum image. The bold contour line shows an irradiance of 4×10^{16} W/cm^2 which is just sufficient to create Ar IX (on this scale). All contours show 1×10^{16} W/cm^2 intervals.

5.3.2 Krypton and xenon targets

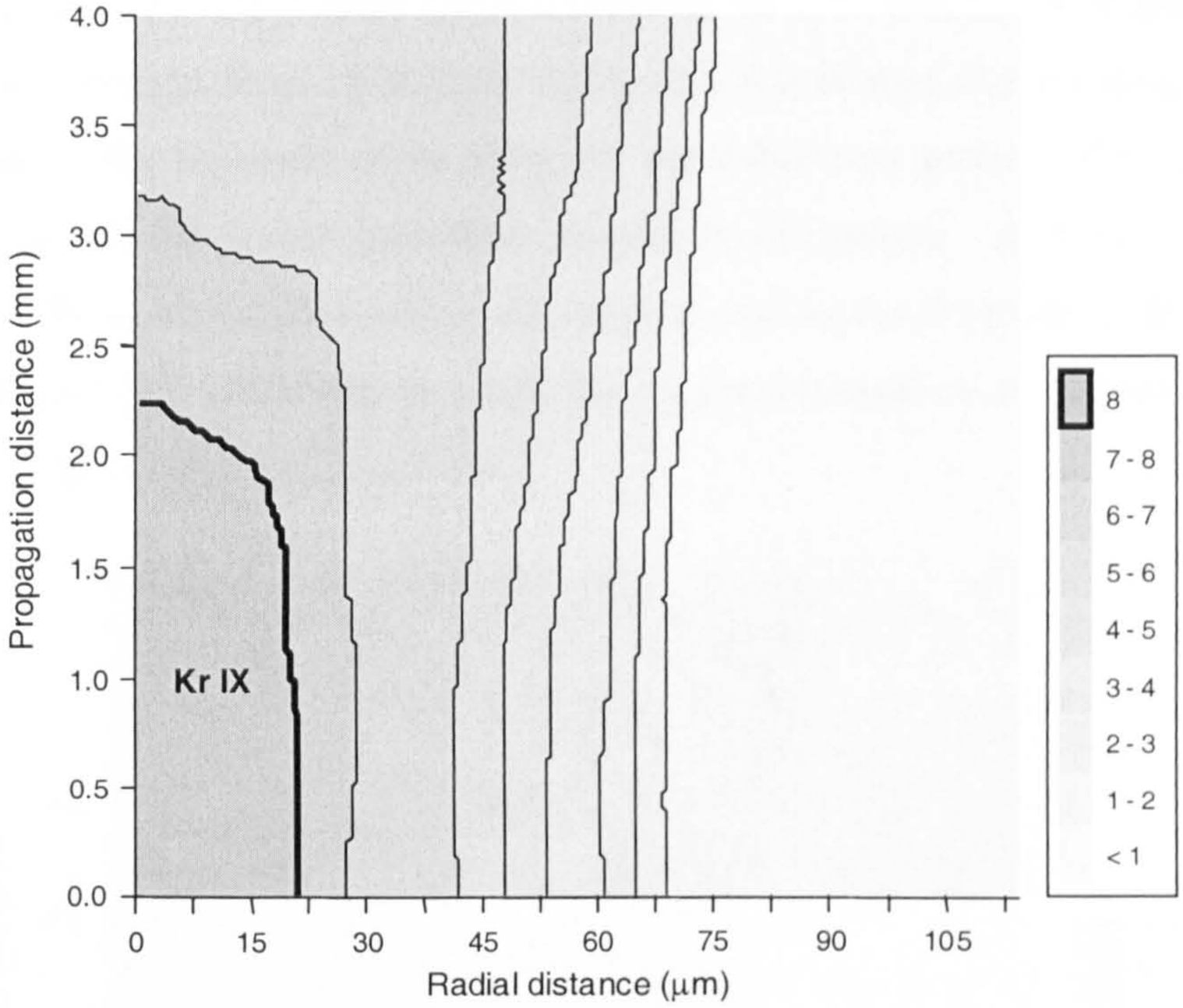

Figure 5.5. Ionisation profile for a driving beam $I_{peak} = 10^{17}$ W/cm^2 propagating into krypton at a density of 10^{17} cm^{-3}

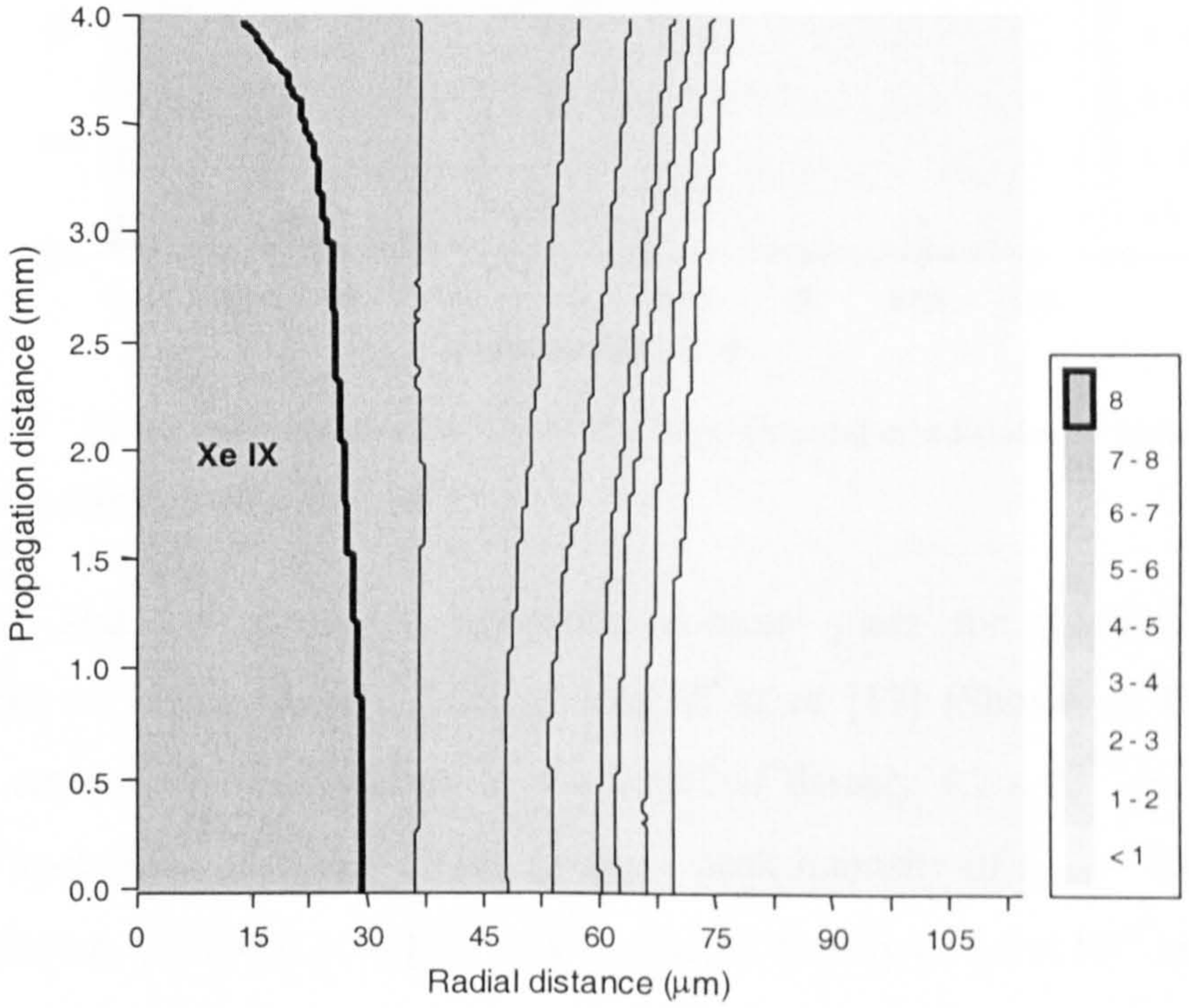

Figure 5.6. Ionisation profile for a driving beam $I_{peak} = 10^{17}$ W/cm^2 propagating into xenon at a density of 10^{17} cm^{-3}

The above two figures show the ionisation profiles for krypton and xenon at a density of 10^{17} cm^{-3} for a peak pulse irradiance of 10^{17} W/cm^2. Comparing these with argon under the same conditions in Figure 5.1 it is seen that creating a useable channel of xenon is much easier than for the other two gases. This is a direct consequence of the lower ionisation potentials of xenon. Although the beam refraction effects are no less severe for krypton and xenon than argon, the fact that they require a lower irradiance to create the required ionisation stage means that the break up of the beam is not so critical.

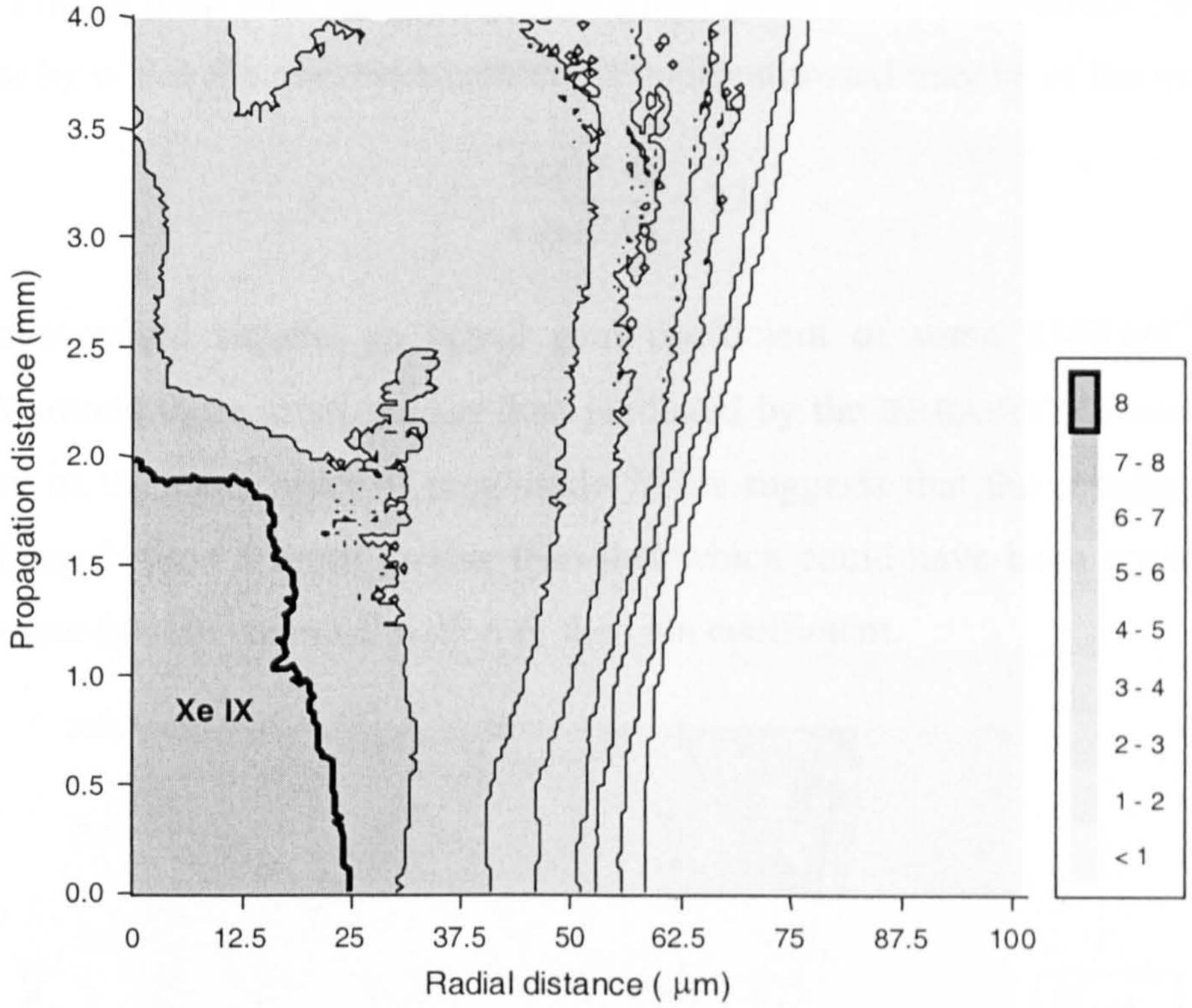

Figure 5.7. Ionisation contours for Xe for the experimental conditions of Lemoff [17] at an ion density of 4.7×10^{17} cm^{-3}.

Figure 5.7 and 5.8 show the ionisation contour plots for the two reported observations of lasing in Xe. That of Lemoff *et al* [17] (Shown in Figure 5.7) delivered around 90 mJ of energy to the target of density 4.7×10^{17} cm^{-3} with an estimated spot radius of $w_{1/e} = 30$ μm giving a peak intensity of $I_{peak} = 10^{17}$ W/cm^2. The experiment of Balcou *et al* [19] was at a target density of 5.8×10^{17} cm^{-3}, a spot radius $w_{1/e} = 20$ μm and a beam energy of ~350 mJ giving a peak intensity of $I_{peak} = 9.3 \times 10^{17}$ W/cm^2.

The Lemoff experiment shows a roughly regular channel of Xe IX of around 20 μm radius and 2 mm in length. They did not measure the size of the channel in their experiments but the gain measurement of $16.8 \pm 0.5\ \mathrm{cm}^{-1}$ was made on the assumption that it extended the entire length of the target of 7.4 mm. For this reason it becomes clear that they have considerably underestimated the gain. It is possible to make a crude estimate of the factor by which the gain is underestimated by making use of the exponential nature of the growth in output irradiance with the length of the medium as given by equation (2.62). Assuming that saturated output was observed (which is likely even with small lengths of 2 mm given gains of hundreds cm^{-1}), then the factor by which the gain measurement is underestimated may be of the order

$$f \sim \frac{\exp(7.4)}{\exp(2.0)} \sim 220 \tag{5.1}$$

This factor would suggest an actual gain coefficient of some $3300\ \mathrm{cm}^{-1}$ which, although around three times greater than predicted by the BREAKDOWN simulations, is at least of the same order of magnitude. This suggests that the assumption of a lasing channel some 3 times greater than that which could have been produced has led to a considerable underestimation of the gain coefficient.

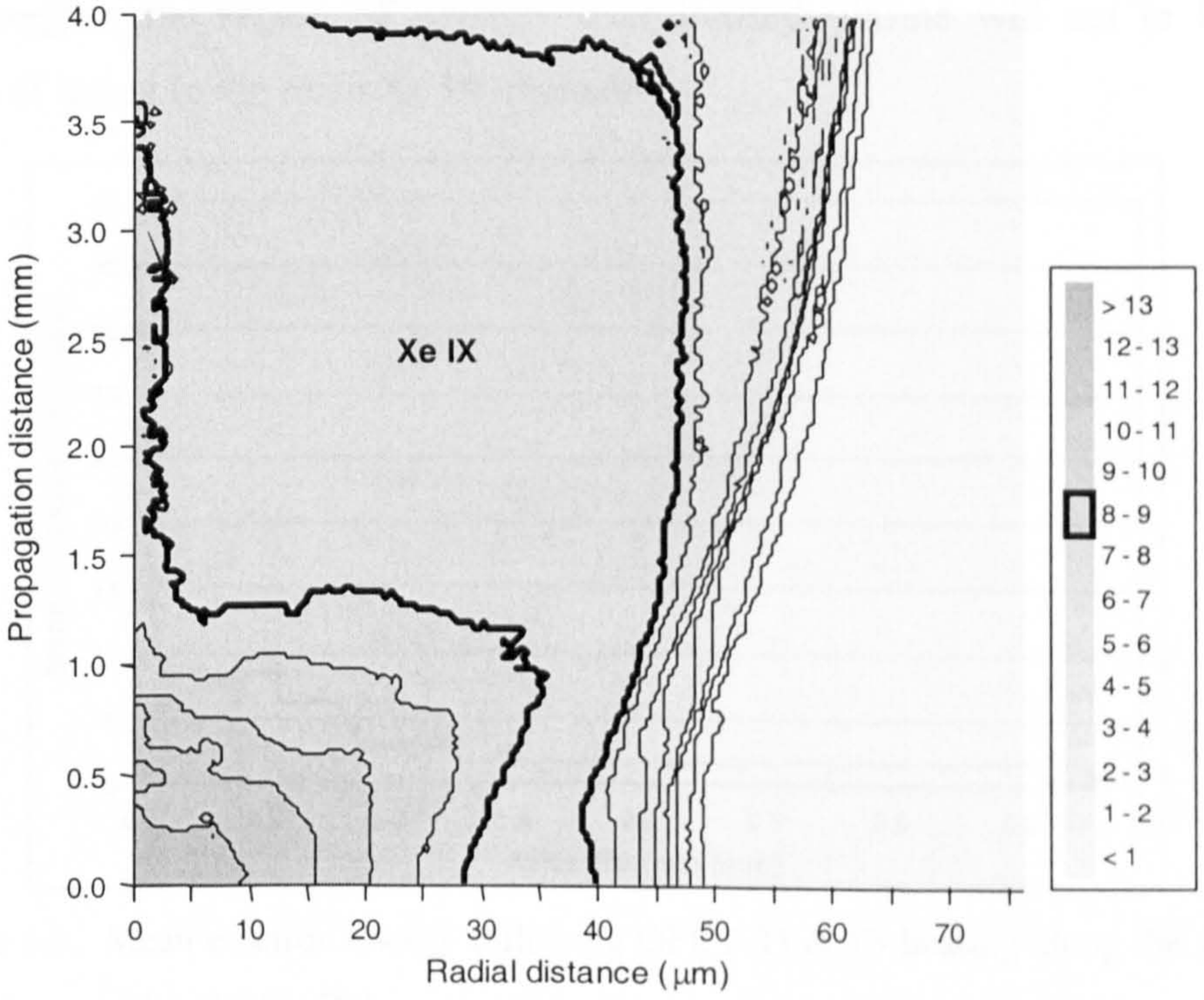

Figure 5.8. Ionisation contours for Xe for the experimental conditions of Balcou [19] .

The much larger pulse energy used by the Balcou group means that ion stages higher than Xe IX are created as the pulse entered the gas, with a small surrounding region of Xe IX thus forming a ring of the lasing ion at radii of 30 to 40 μm. As the irradiance drops through refraction, Xe IX could have been expected to be produced from around 1.25 mm into the gas up to about 4 mm and a considerable uniform channel of around 40 μm radius by 2.75 mm in length may be formed. Although there should therefore be lasing over all target lengths up to around 4 mm, that in the ring preceding the uniform region will not act to significantly amplify the emission in the bulk of the desired plasma. The gain measurement in this experiment was made assuming plasma lengths of up to 5 mm. Again performing this crude analysis, then the factor by which the measured gain may be underestimated may be of the order

$$f \sim \frac{\exp(5.0)}{\exp(2.75)} \sim 9.5 \tag{5.2}$$

which would suggest a gain coefficient of around $67 \times 9.5 \approx 640\ \mathrm{cm}^{-1}$. This compares with a predicted value of $\sim 1200\ \mathrm{cm}^{-1}$ and given the expected losses due to refraction, this again brings the value into the same region as that predicted.

Although the experiment of Balcou *et al* has clearly demonstrated lasing using larger pulse energies, the region of strongly over ionised plasma will act to limit the duration of lasing in the main Xe IX channel.

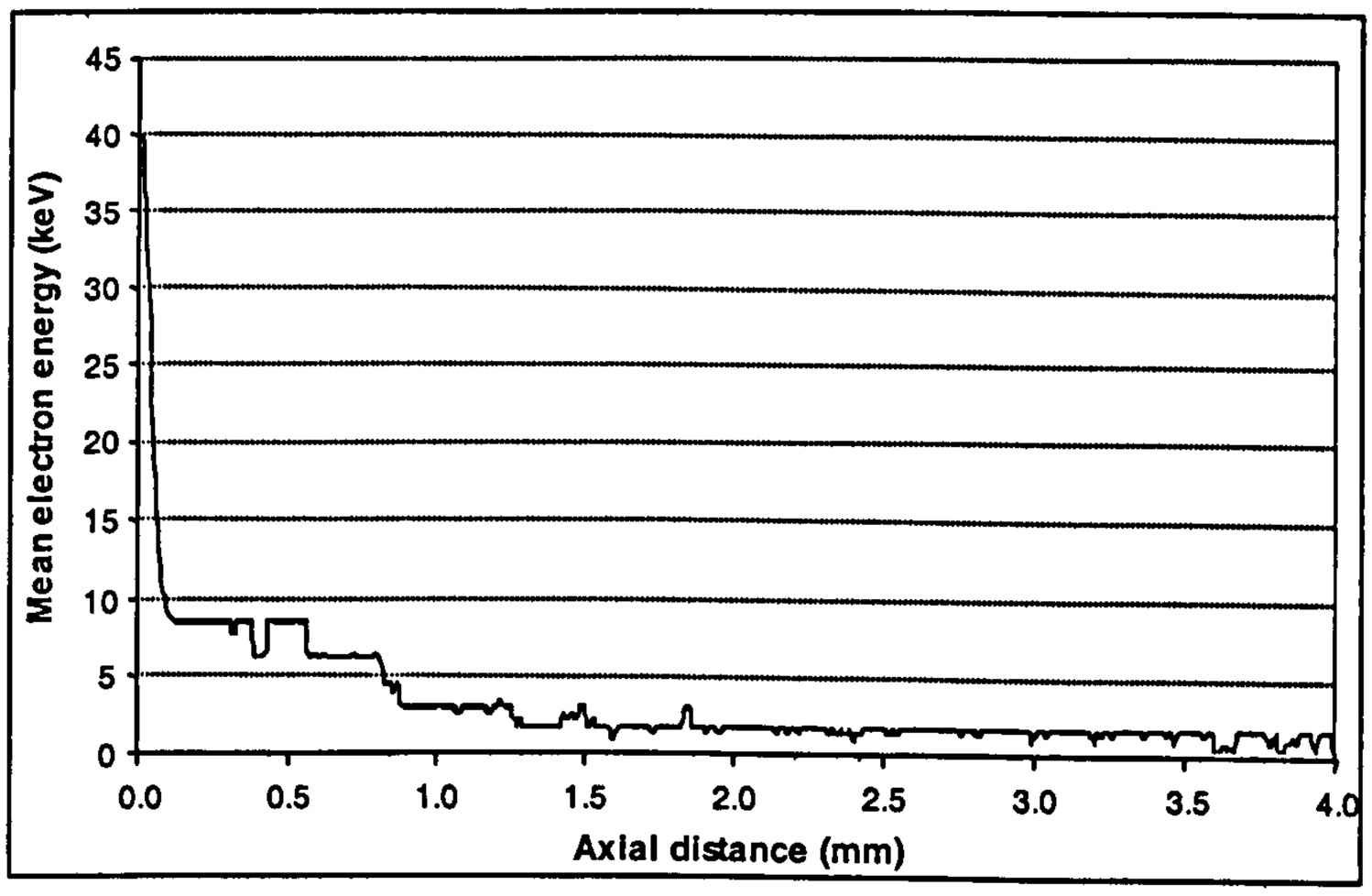

Figure 5.9. Mean electron energy following OFI, ATI & IB heating along the axis of beam propagation for the Balcou experiment.

The electrons resulting from this over ionised region will be of extremely high energies as shown in Figure 5.9. These keV electrons will rapidly move down the electron and temperature gradients into the region of Xe IX where they will act to collisionally ionise the ions and terminate lasing. An accurate evaluation of this effect requires a 2-D hydrodynamic simulation which is beyond the scope of the codes available for this work. A rough estimate is possible by noting that 10 keV electrons would take around 10 ps to travel into the region of Xe IX where they would then begin to over ionise this region of plasma. The time of peak gain as predicted by BREAKDOWN for this density is around 5 ps with significant gain still being produced at up to 20 ps. It is therefore expected that collisional ionisation would significantly reduce the lasing output available in regions adjacent to the over ionised plasma. This may also result in an additional slight overestimation of the length of the lasing region experimentally.

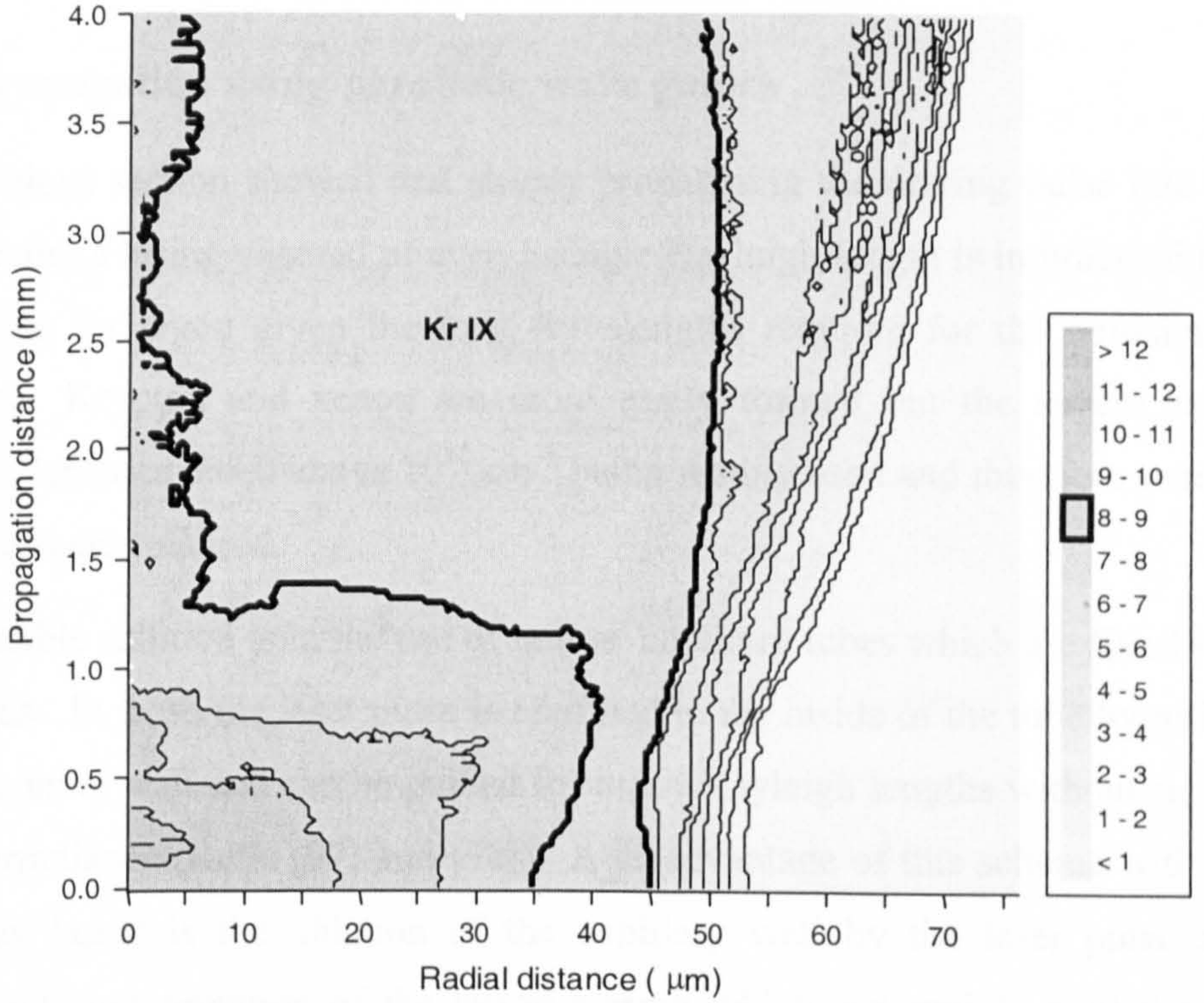

Figure 5.10. Ionisation contours for Kr for the experimental conditions of Sebban [20] at an ion density of 7.7×10^{17} cm^{-3}.

Figure 5.10 shows the ionisation state of a Kr plasma for the unpublished experiment of Sebban [20]. In this case, a larger driving pulse energy of 700 mJ was used,

representing a peak intensity of around 1.8×10^{18} W/cm^2. The plasma shows the same features as for the Xe with a ring of Kr IX formed surrounding an over ionised region before the intensity falls sufficiently to form a near uniform region of Kr IX approximately 35 μm in radius and at least 2.5 mm in length. A minor difference in this case is that a channel of Kr X is formed on the axis indicating that a slightly smaller peak intensity would have created a more uniform region of Kr IX.

The experimental analysis in this case estimated saturation at a plasma length of 4.0 mm. The simulation in Figure 5.10 does not extend far enough to show where the Kr IX column ceases to be produced but faster, lower resolution simulations show a column length of around 3 mm is produced. Thus we can again estimate that the gain is underestimated by a factor of $e^4 / e^3 \sim 2.7$, suggesting a gain coefficient of around 200 cm^{-1} compared to ~ 500 cm^{-1} from the BREAKDOWN simulations.

5.4 Propagation using parabolic wave guides

The previous section showed that simply propagating the driving pulse into the gas and forming a lasing channel of even a single Rayleigh length is impracticable if not impossible for argon given the long wavelengths required for the collisional OFI schemes. Krypton and xenon are more easily formed but the severe refraction prevents densities much above 10^{18} cm^{-3} being readily used and therefore more novel approaches are required.

One possible solution is in the use of hollow capillary tubes which are filled with the lasing gas. In these the laser pulse is confined to the inside of the tube by reflections from the inner wall and can be guided for many Rayleigh lengths without significant loss in irradiance (Refs. [97] and [98]). A disadvantage of this scheme with respect to X-Ray lasers is the ablation of the capillary wall by the laser pulse and the subsequent contamination of the lasing plasma which can rapidly cool the plasma and terminate the collisional pumping.

A more promising alternative to capillary tubes is to somehow manipulate the refractive index within the plasma in order to counteract the OFI inducing refraction.

An alternative form of the refractive index for a laser beam in a plasma, as a function of radial distance r, from that given by equation (2.40) is;

$$\eta(r) = \sqrt{1 - \frac{n_e(r)e^2}{\gamma m_e \omega^2}} \tag{5.3}$$

where ω is the angular frequency of the laser and n_e is the electron density as function of radial position. γ is the Lorentz factor which describes the relativistic increase in the electron mass due its quiver velocity in the field. As previously discussed, this may need to be considered at the intensities that may be required.

In order to prevent a beam refracting away from the axis, the refractive index gradient (with respect to radius) must be negative. It can be seen from (5.3) that this is never the case for an electron density profile created by the OFI process since this density profile has a negative gradient. (At intensities of greater than around 10^{19} W/cm^2 the relativistic increase in the electron mass can create this effect in a process known as relativistic self guiding and was first observed by Borisov *et al* [99] in 1992.) A thorough review of various aspects of high intensity laser interactions with plasmas is given in [100].

Work by Sprangle *et* al [101] and Esarey *et al* [102] in examining how the envelope function of an intense laser pulse is self modulated by relativistic effects in a plasma, showed that a laser beam with a Gaussian radial profile can be guided with a constant spot size if the radial electron density profile is of the parabolic form;

$$n_e(r) = n_e(0) + \Delta n_e (r / r_m)^2 \tag{5.4}$$

where $n_e(0)$ is the axial electron density and $\Delta n_e(r)$ is the increase in electron density at radius $r = r_m$. The radius of the Gaussian beam must be 'matched' to the electron density profile as shown in Figure 5.11.

The depth of the plasma profile is given by

$$\Delta n = \frac{1}{\pi r_e r_m^2} \tag{5.5}$$

where the classical electron radius

$$r_e = \frac{e^2}{4\pi\varepsilon_0 m_e c^2} \tag{5.6}$$

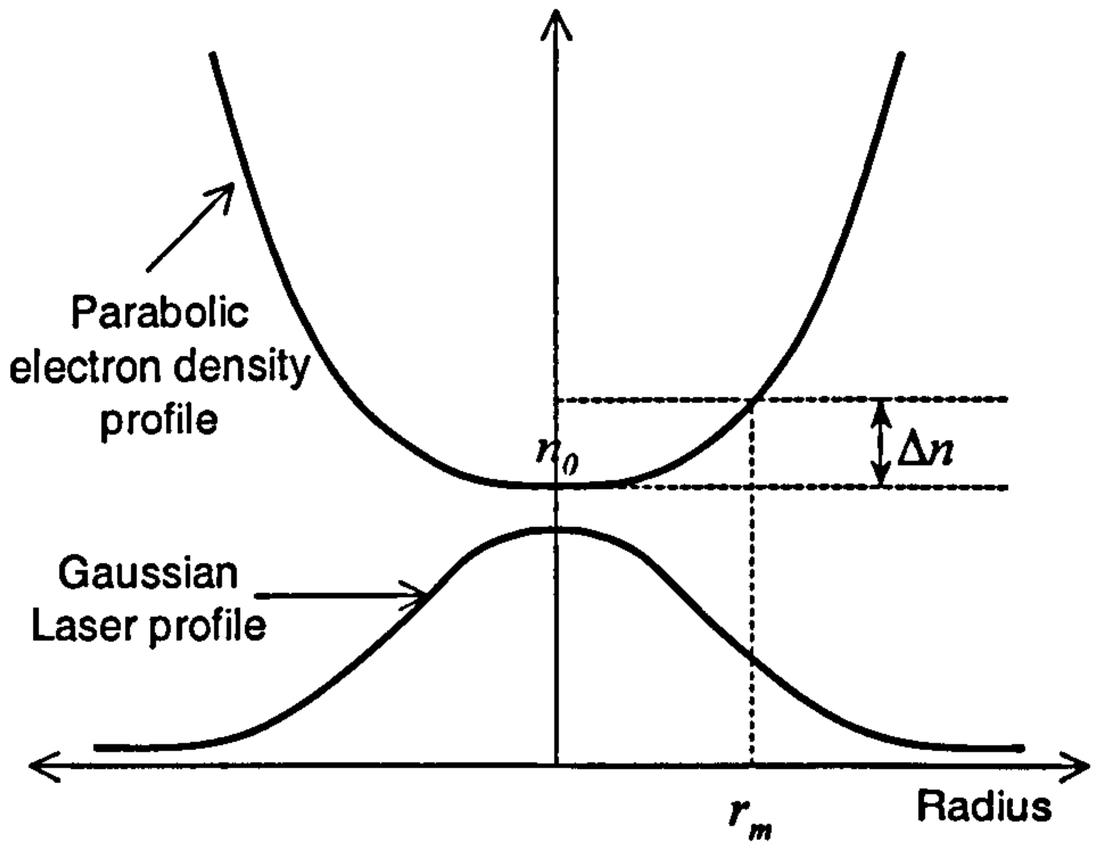

Figure 5.11. Channel parameters required for optical guiding of a laser pulse in a pre-formed parabolic plasma.

Numerical simulations of such guides by Spence *et al* [103] have shown that such channels should be efficient at guiding while more recently a number of groups (refs. [104], [105], [106], [107], [108] and [109]) have successfully demonstrated experimental guiding of laser pulses over many tens of Rayleigh lengths with no significant attenuation of irradiance. The notable work Ehrlich *et al* [106] showed that the technique can also be used to guide pulses around curves.

The matching of the beam radius to the channel parameters is only practically possible for a single radius, usually measured as that from the width at the time of the pulse peak. The pulse radii are different for the leading and trailing edges of the pulse and so complete guiding is not possible. Consequently, the pulse radius oscillates sinusoidally about its initial value as it propagates through the channel. Propagation therefore occurs as quasi-matched guiding (QMG). Calculations of this effect have been made [100] and showed that the spatial period of these oscillations for the guided pulse, p_g, is approximately;

$$p_g \approx \frac{c\tau}{z_R} \tag{5.7}$$

This oscillation is seen in simulations made on a modified version of PROPAGATE in which a pulse propagates through a pre-formed parabolic waveguide, but which has no noble gas component. The waveguide is based on that produced and measured by Spence *et al* [105] in which they produced a hydrogen plasma with an on axis density of $n_e(0) = 2.72 \times 10^{18}$ cm^{-3}. The depth of the channel was such that the ideally matched pulse radius was determined to be 37.5 μm. Thus for a pulse of duration $\tau \sim 30$ fs, then the pulse radius should fluctuate with a spatial period of around 1.6 cm. The radius of such a pulse propagating within this waveguide is shown in Figure 5.12. The period is as expected and thus confirms the validity of the code modifications.

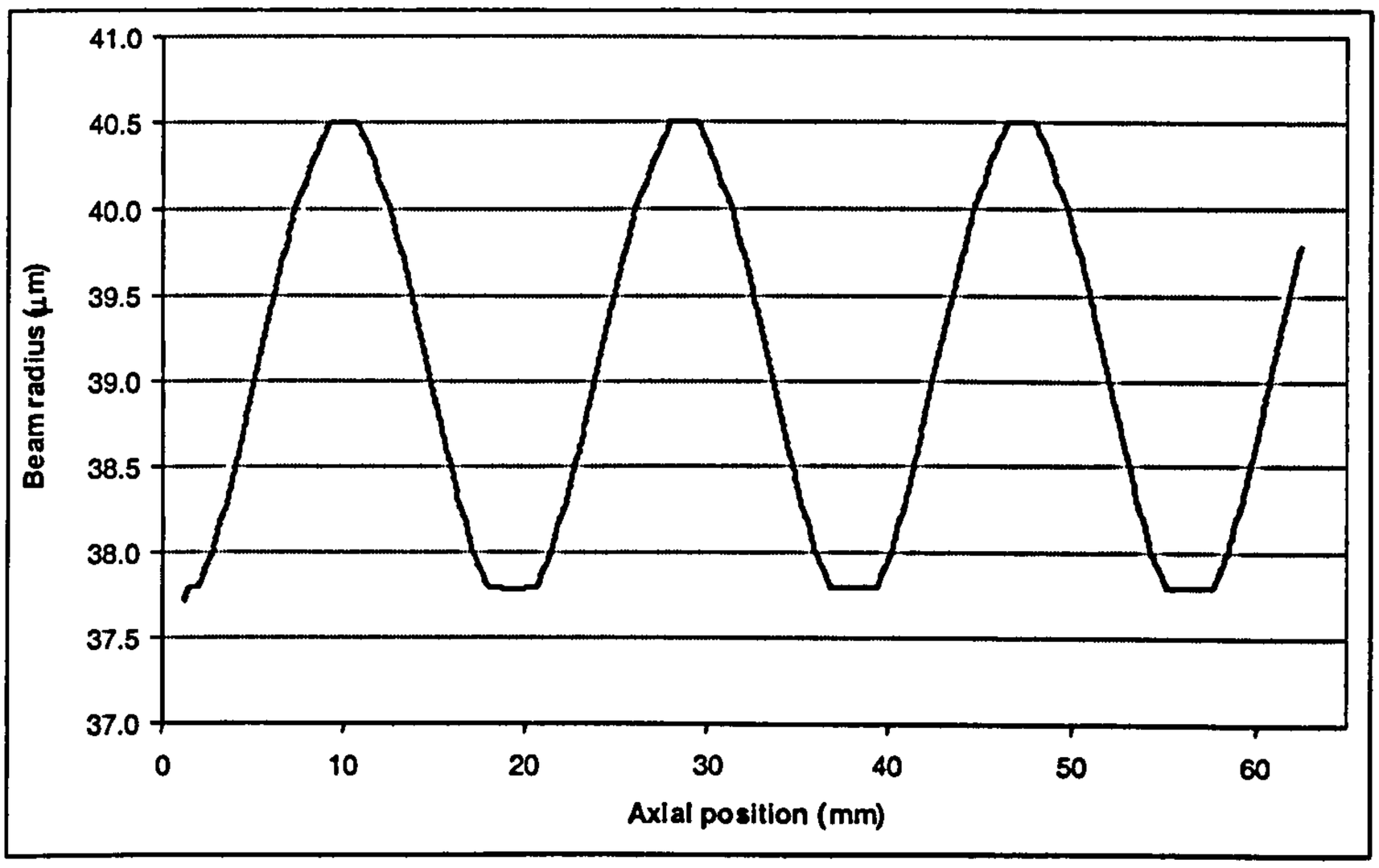

Figure 5.12. Radius of a pulse with initial radius 37.5 μm propagation along the axis of a parabolic plasma waveguide. The waveguide is based upon the hydrogen structure measured by Spence *et al* [105].

There are currently two distinct techniques used to create these wave guiding structures. The first of these is by thermally driven laser expansion of the plasma (Refs. [108], [109] and [111]). A pulse of intensity ~10^{13} W/cm^2 and duration ~100 ps is tangentially focused onto a gas jet. The electrons initially released by multi-photon ionisation are heated by IB and cause further collisional ionisation. The heated electrons move into the surrounding neutral gas creating an electron density minimum on axis. Charge separation effects will also tend to drag the ions

after electrons. The experimental work of Clarke and Milchberg [109] showed that expansion of the plasma was in good agreement with that of a self-similar cylindrical blast wave [112].

The second method is by electric discharge through a capillary. This method works in a manner very similar to the Z-pinch and electrically discharged X-ray laser. A plasma is formed by discharge through a gas as in [105] and [113] or by direct ablation by the current of the capillary wall as in [106]. The magnetic fields created by the current then cause the plasma column to collapse upon itself thereby creating a density minimum on axis. The advantages of this scheme over the laser driven expansion are primarily that these discharge devices are now well understood and the plasma density can be modified over a wide range which is independent of the required the guiding conditions (Refs. [114] and [115]).

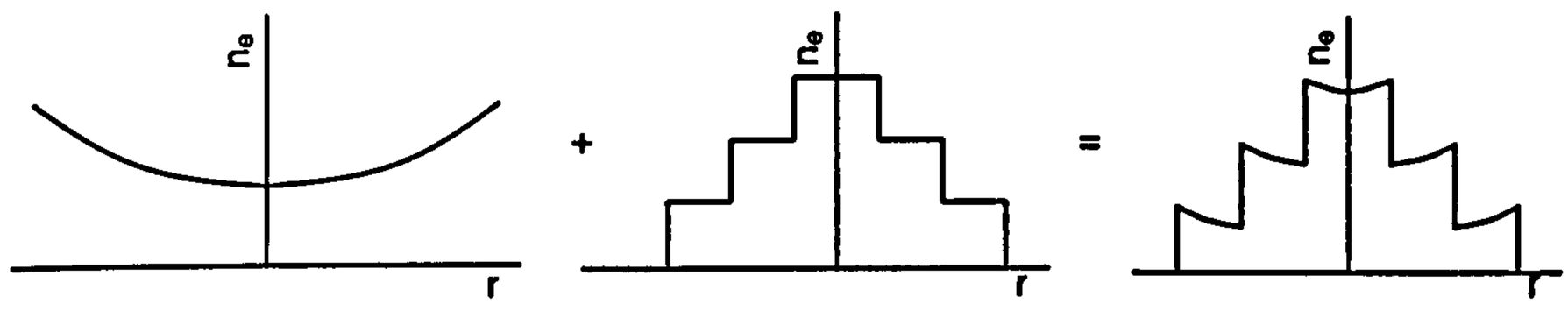

Figure 5.13. Schematic diagrams illustrating the formation of a parabolic electron gradients for use as wave guides. The superposition of a parabolic profile (left) with a subsequent step wise OFI profile (centre) produces a central region of ionisation that is also parabolic (right).

Figure 5.13 illustrates how the creation of a parabolic electron density profile becomes useful for the OFI laser schemes. By doping the gas in the discharge capillary with gas of the lasant species, any OFI laser pulse that is propagated through the capillary after the creation of the parabolic profile will have the step like profile superimposed upon the parabolic profile. If the gases are suitably chosen such that the gas forming the parabolic profile is completely ionised (or to a configuration unaffected by the subsequent OFI pulse) by the discharge current while the dopant gas is largely unaffected by the discharge but only by the OFI pulse, then a central channel of the required ionisation stage can be produced which will have the required electron and refractive index profiles to guide the OFI pulse over significant distances. The ideal capillary gas for this is hydrogen since it can be

easily completely ionised by the electric current. The work of Ehrlich *et al* [106] used electric currents of around 500 A to ablate a hydrogen rich plastic capillary, while Hosokai *et al* [113] used 2.5 kA to ionise a helium filled capillary. Both these currents are small enough (for example when compared to the ~40 kA used by the argon capillary discharge X-ray laser in [12] and [13].) not to significantly affect argon up to Ar IX.

Finally, these gas filled capillaries are expected to have long lifetimes of up to 10^6 shots [105] and this coupled with the few Hz operating rate of the driving laser makes them particularly attractive for use in OFI X-ray schemes.

Although much experimental and computational work has now been published on the use of this technique to guide laser pulses, there is no work available examining the use of dopant gases. These are now examined here. PROPAGATE was modified to allow for a pre-formed parabolic electron density profile to be created in the form of (5.4) which extends the full axial distance of the mesh. In order to simulate some degree of experimental 'noise' in this profile, random variations are added such that the exact form used is;

$$n_e(r) = n_e(0) + [1 \pm \delta f]\Delta n_e (r/r_m)^2 \tag{5.8}$$

where δ is a uniformly distributed random number ($\delta \in \Re(0,1)$) and f is an error estimate less than unity. The propagation calculations then proceed as before with the contribution to the electron density from (5.8) added to that of the OFI electrons to form the refractive index. It is assumed that once formed, this 'background' electron density does not change further for the duration of the pulse propagation.

5.4.1 Doped parabolic waveguides

The waveguide used here is based on that previously mentioned of Spence *et al* [105]. However, the matched pulse radius of 37.5 μm is larger than is typically used in OFI experiments since the smaller spot size allows for higher intensities. As a result, the simulations here use the same on axis density but the depth, Δn_e, is varied in order to propagate a pulse of radius 20 μm. This smaller radius requires $\Delta n_e = 2.8 \times 10^{17}$ cm^{-3} compared to the $\sim 8.0 \times 10^{16}$ cm^{-3} of [105]. For a discharge

capillary plasma this higher density may be obtained at later times in the collapse of the plasma.

The oscillatory nature of the pulse guiding means that it may not be desirable to operate at the channel depth which matches this radius and as such a range of depths is examined. Those considered are $\Delta n_e = 1.1 \times 10^{18}$, 5.0×10^{17}, 2.8×10^{17} and 1.8×10^{17} cm^{-3} corresponding to matched radii of 10, 15, 20 and 25 μm respectively. The initial pulse radius remains at 20 μm in all cases. The pulse duration is set of FWHM 30 fs. The error estimate for the parabolic density profile is set at 10% for all simulations unless stated to be different. This figure is based upon the measured profile of Spence *et al* [105] which showed fluctuations of the order of 5%.

Preliminary simulations showed that at noble gas densities of a few percent (less than 5%) of the axial density of the plasma channel then the driving laser could be guided for many cm while still retaining sufficient intensity to create regions of the required lasant ion. The oscillatory nature of the pulse radius was evident in the production of a plasma which consisted of periodic regions of the lasant ion separated by a few mm of under ionised plasma. These low ion densities of around 10^{15} cm^{-3} are far too small to be useable as an X-ray laser source given that the BREAKDOWN simulations suggest a density of at least 10^{18} is required for a significant output irradiance. At these densities, guiding may still be expected to occur but the discontinuous radial electron gradients between regions of adjacent ionisation will now become larger than the background electron density and the beam will therefore break-up into individual regions which should themselves be guided.

Simulations for Ar at a density of 10^{18} cm^{-3} show that useable channels of Ar IX may be created which are in excess of 1 cm in length (the total length modelled here is 2 cm which is imposed by the demands of a suitably small resolution in the cell size and the total number of cells available). Figure 5.14 shows the plasmas created for the four channel depths considered. All plots show the initially oscillatory nature of the pulse radius but it is most apparent in the 'tighter' channels with matched radii of 10 and 15 μm. In these, regions of Ar IX of length around 2 mm are formed which are separated by regions of under ionised plasma. In each case considered, the pulse propagates for around 1 cm before a roughly uniform channel is produced.

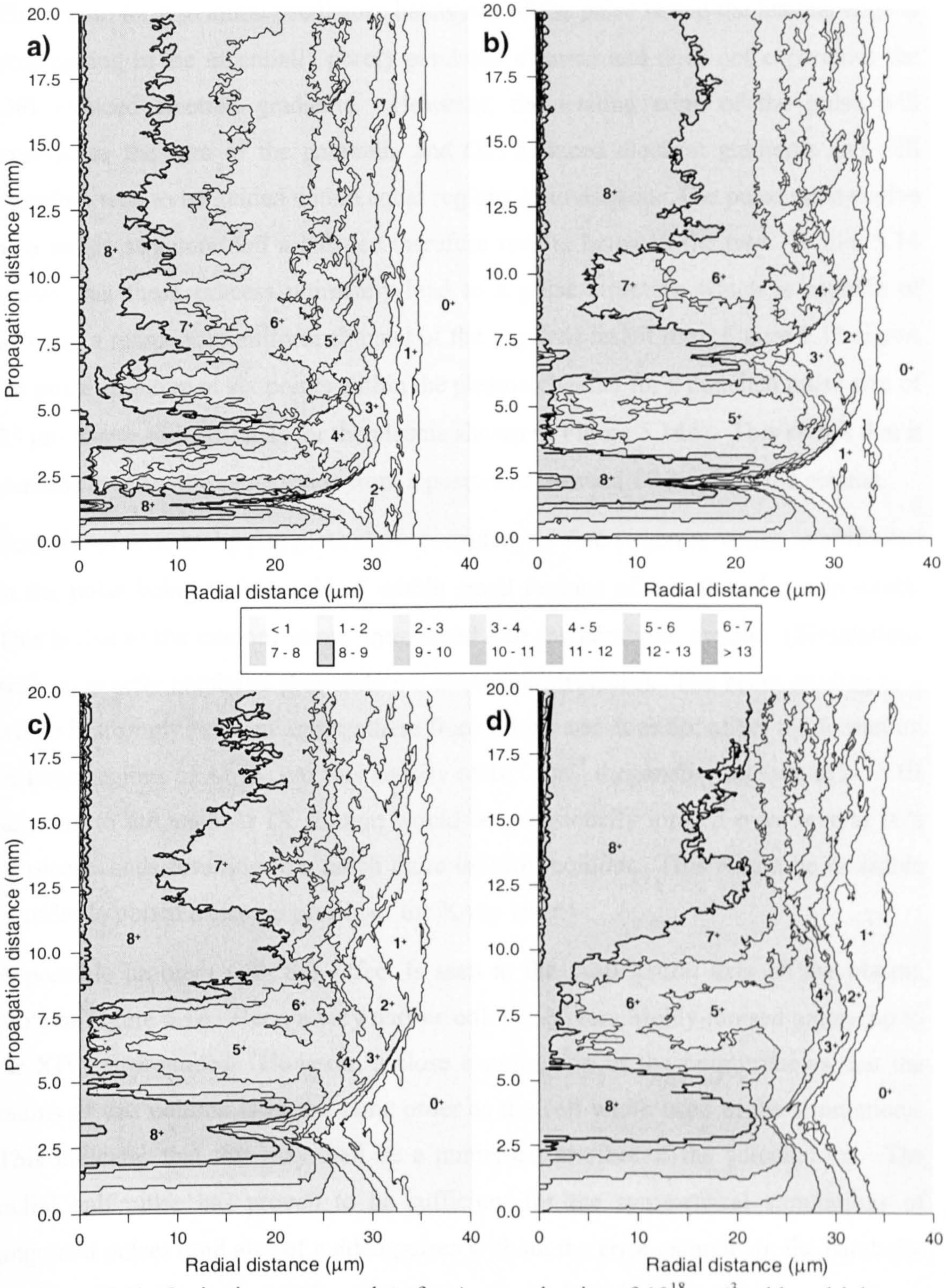

Figure 5.14. Ionisation contour plots for Ar at a density of 10^{18} cm^{-3} with a driving pulse of $I_{peak} = 5 \times 10^{17}$ W/cm^2. The parabolic pre-plasma has channel depths for matched pulse radii of 10, 15, 20 and 25 μm shown on plots a, b, c and d respectively. The region of lasing plasma (Ar IX) is that within the bold contour line. Adjacent regions of ionisation are labelled (up to Ar IX) with the charge state.

The reason for this initial oscillatory behaviour of the pulse is that the leading edge is propagating in the essentially purely parabolic channel and does not experience the OFI induced electron gradients. However, the trailing edge of the pulse will experience the sum of the parabolic and OFI induced electron gradients and will therefore tend to be guided within equal regions of ionisation. The pulse must evolve as a single structure and a balance therefore results between the two. Figure 5.14 shows that these process ultimately lead to a pulse structure which is capable of forming a reasonably uniform channel of the required lasant ion. Figure 5.15 shows the pulse structure at six points within the plasma channel for a matched pulse size of 25 μm (same simulation as for the plasma shown in Figure 5.14d). This shows that it remains roughly the same shape from a position of around 10 mm into the plasma.

Both the plasma and pulse plots show considerable fine structure which is attributed to the pulse being 'micro-guided' within small regions of less than 1 μm in width. This is due to the random 'error' introduced into the parabolic profile. (Simulations with an exactly parabolic profile do not show this structure). The beam guiding as a whole is strongly resilient against these fluctuations and does not affect the formation of large regions of Ar IX. At this density of 10^{18} cm^{-3} the smaller regions of Ar VIII adjacent to the main Ar IX column would be collisionally ionised over several 10's of picoseconds resulting in a much more uniform column. This would be desirable in order to obtain a cleaner profile of the X-ray laser.

A possible problem with this effect is seen at the propagation axis on the plasma plots of Figure 5.14. Here, a very narrow column of very highly ionised argon (up to Ar XIV) is produced. However, a close examination of the output shows that the radius of this column is of the same order as the cell width used in the simulations. This indicates that this may well be a numerical artefact of the calculations. The radial half pulse has proven to be sufficient for the symmetrical simulations of unguided pulses (and also of guided pulses without the error estimate in the parabolic profile which do not show this affect.) however the introduction of the error estimate means that the pulse will not be guided exactly symmetrically through the channel.

This may cause problems in the calculations which assume that the centre of the pulse is fixed at the $r = 0$ position. Simulations of the full radial pulse are needed to

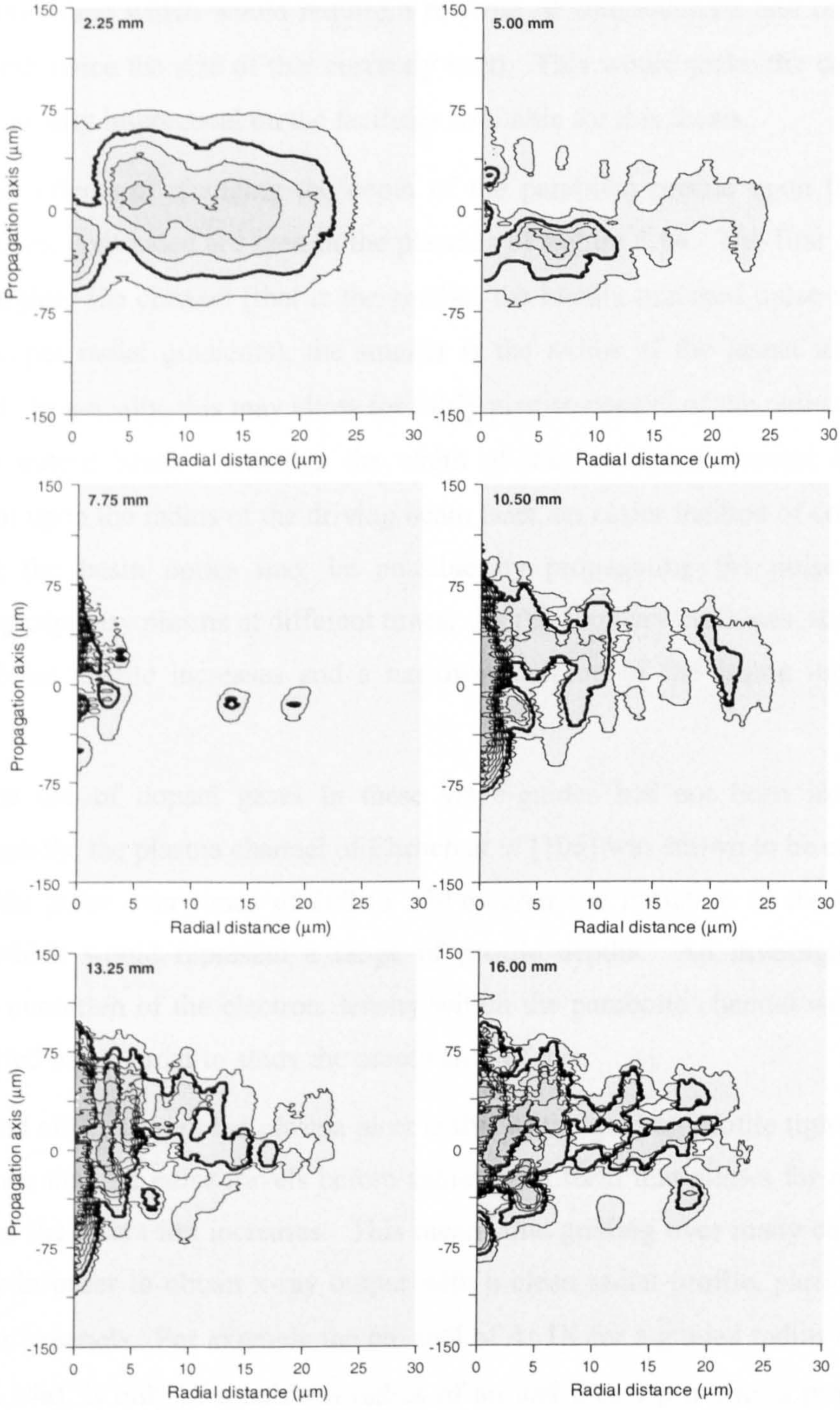

Figure 5.15. Irradiance contour plots for a pulse of initial peak irradiance of 5×10^{17} W/cm^2 propagating through Ar of density 10^{18} cm^{-3} in a pre-formed parabolic plasma channel of matched radius 25 μm. (Same case as in Figure 5.14d). Plots are labelled with the position of the centre of the pulse (0 μm on the propagation axis) at the axial position in the plasma channel. The bold contour shows an irradiance of 4×10^{16} W/cm^2 which is just sufficient to create Ar IX (on this scale). All contours show 2×10^{16} W/cm^2 intervals.

resolve this issue which would require a re-write of PROPAGATE and the use of a radial mesh twice the size of that currently used. This would make the calculations computationally impractical on the facilities available for this thesis.

Two main effects of changing the depth of the parabolic profile upon the size of Ar IX channel produced are seen in the plasmas of Figure 5.14. The first of these is that the tighter the channel (that is the smaller the ideally matched pulse radius and hence steeper radial gradients), the smaller is the radius of the lasant ion channel produced. Practically, this may allow for fairly precise control of the radius of the X-ray laser output beam. Although the width of the lasant ion channel is directly dependant upon the radius of the driving beam laser, an easier method of control than adjusting the beam optics may be possible by propagating the pulse into the collapsing capillary plasma at different times. As the capillary collapses, the depth of the parabolic profile increases and a narrower column of the lasing ion may be created.

While the use of dopant gases in these wave-guides has not been investigated experimentally, the plasma channel of Ehrlich *et al* [106] was shown to be efficient at guiding the pulse over times of 200 to 350 ns after the initiation of the discharge current which would represent a range of profile depths. An investigation into temporal evolution of the electron density within the parabolic channel would need to be carried out in order to study the practicality of this.

The second effect seen in the plasma plots is that as the guiding profile tightens, then the distance that the pulse travels before achieving a form that allows for a uniform channel of the lasant ion increases. This means that guiding over many cm may be necessary in order to obtain x-ray output with a clean radial profile, particularly in the tighter channels. For example the channel of Ar IX for a guided radius of 10 μm (Figure 5.14a), is only of a uniform radius of around 6 or 7 μm after a propagation distance of 2 cm.

Simulations have also been performed on krypton and xenon at a density of 10^{18} cm^{-3} using the same wave-guide structure and are shown in figures 5.16 and 5.17 respectively. In these, the peak pulse irradiance has been lowered to 10^{17} W/cm^2 which may be expected to be sufficient given the lower ionisation potentials of these gases. The beam radius is left unchanged at 20 μm.

Plasmas from both these gases show the same features as for argon although it is clear that the lower irradiance is insufficient to create channels of more than around 5 μm in radius of the lasant ion. Raising the irradiance to 5×10^{17} W/cm^2 is necessary for wider channels. The non-physical axial core of highly ionised plasma is particularly evident in the xenon simulations.

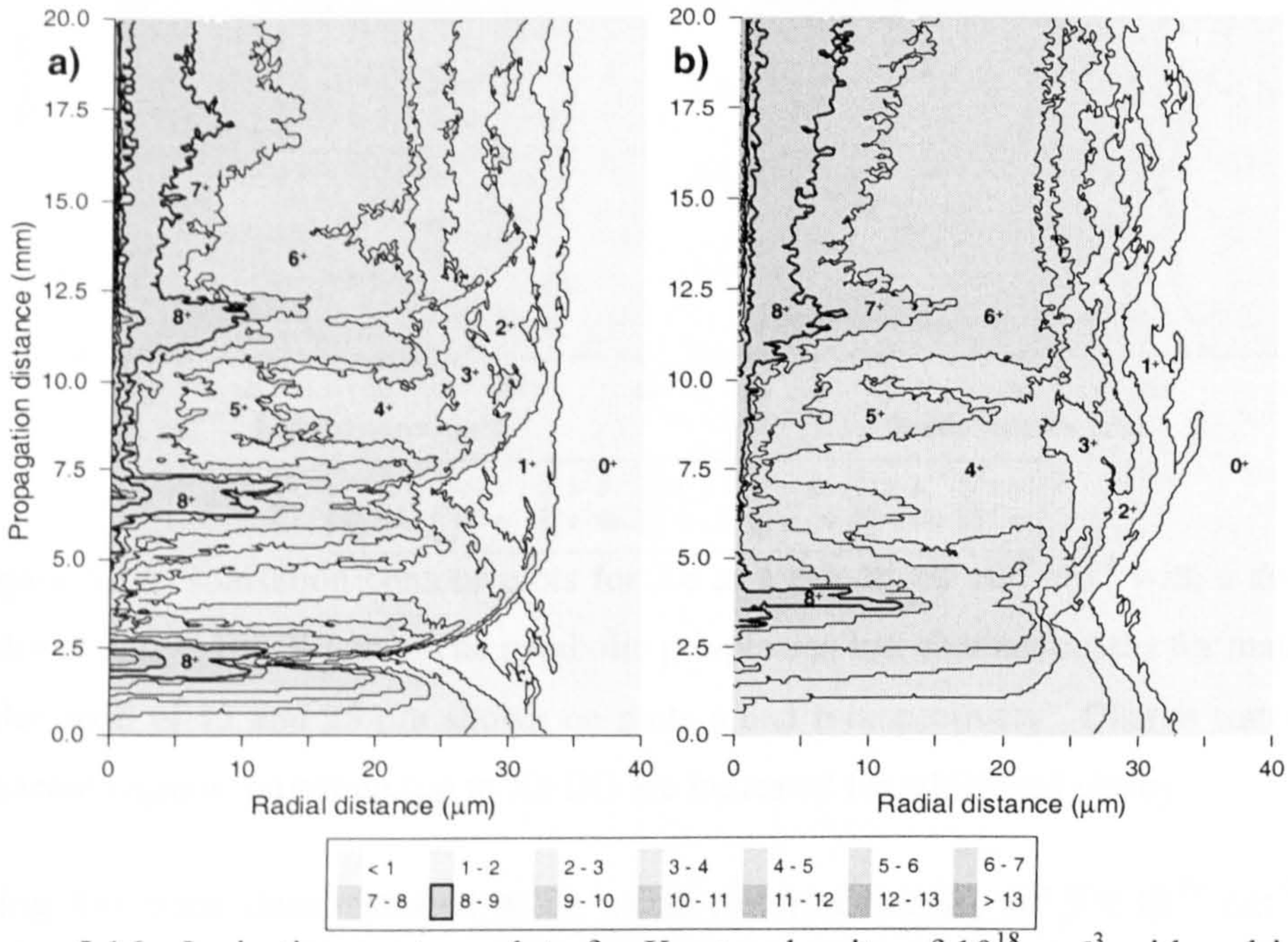

Figure 5.16. Ionisation contour plots for Kr at a density of 10^{18} cm^{-3} with a driving pulse of $I_{peak} = 10^{17}$ W/cm^2. The parabolic pre-plasma has channel depths for matched pulse radii of 15 and 25 μm shown on plots a and b respectively. Charge states for adjacent regions ionisation (up to Kr IX) are indicated for additional clarity.

The ionic density of 10^{18} cm^{-3} so far considered is interesting in that it is of the same order as the density of the hydrogen plasma. At a noble gas / hydrogen ratio of 1:2.7 the combination of the parabolic profile and OFI electrons results in an electron density which is around 4 times that used in the experiment of Spence *et al* [105] and 0.2 times that of Ehrlich *et al* [106]. As a result, guiding of the driving pulse in this mixture should not be too problematic providing that the noble gases do not significantly alter the dynamics of the plasma channel before the arrival of the driving pulse. Collisional ionisation of the noble gases by the discharge current can be expected to ionise at least the first stage of each where the ionisation energy (see Table 3.1) is less than for hydrogen in each case.

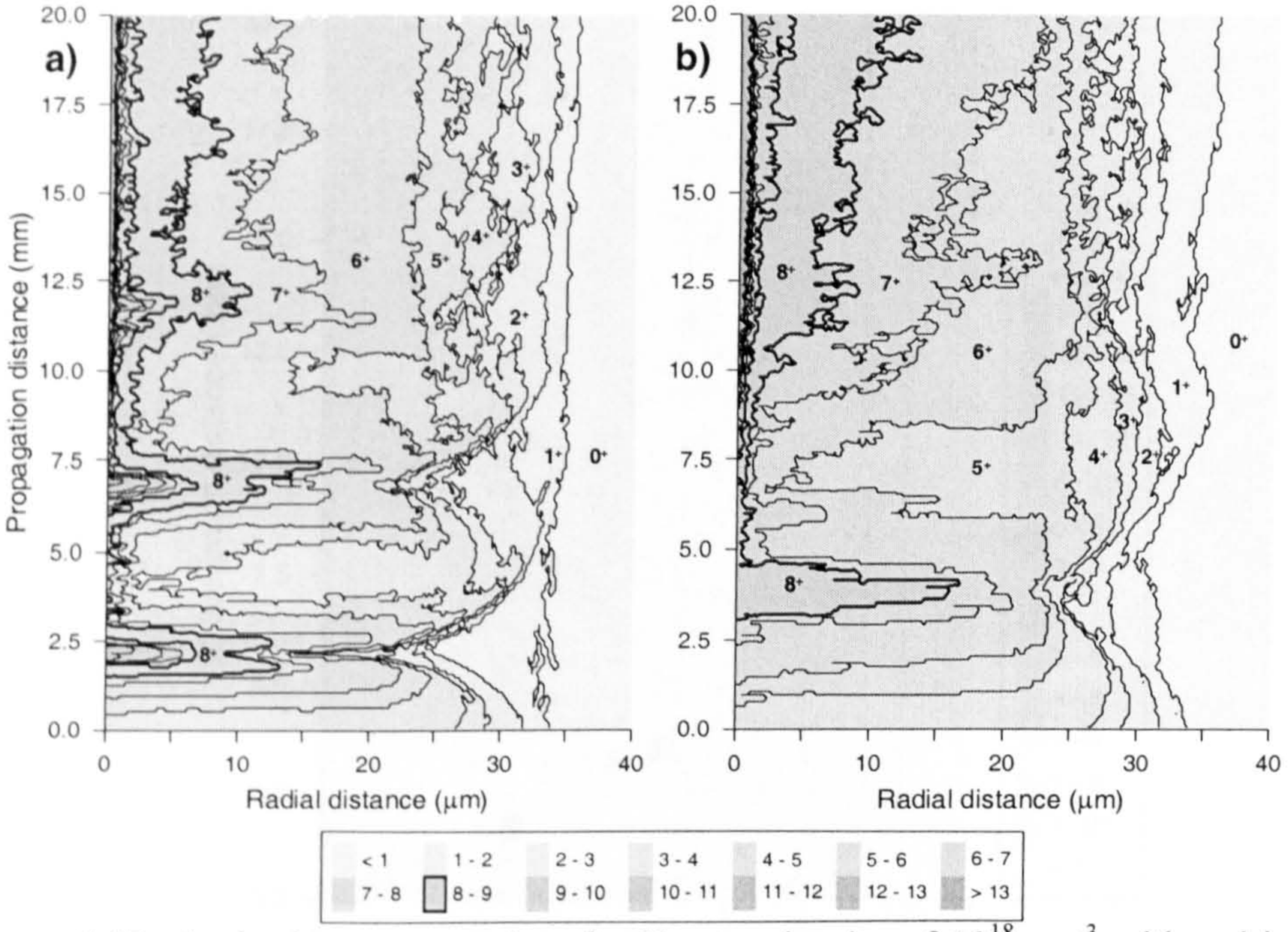

Figure 5.17. Ionisation contour plots for Xe at a density of 10^{18} cm^{-3} with a driving pulse of $I_{peak} = 10^{17}$ W/cm^2. The parabolic pre-plasma has channel depths for matched pulse radii of 15 and 25 μm shown on plots a and b respectively. Charge states for adjacent regions ionisation (up to Xe IX) are indicated for additional clarity.

Guiding has been demonstrated at an axial electron density of 5×10^{19} cm^{-3} [106] and since it is the absolute change in electron density, Δn_e, which is responsible for guiding, it may therefore be possible to operate at even higher densities which would enable the higher saturated irradiances on the x-ray lines to be achieved. This should allow for the saturated output of the inner sub-shell lines of argon to be observed in target lengths of less than a centimetre. Figure 5.18 shows the results of guiding in a plasma channel where the ion density is now 10^{19} cm^{-3} and illustrates that a very uniform column of Ar IX is produced of radius ~22 μm.

The plasma in this case displays nothing of the oscillatory nature of the pulse radius and indicates that where the total electron density is much greater than the parabolic profile density (in this case 29 times greater on the axis) a pulse structure is formed within a distance of a few Rayleigh lengths ($z_R = 1.6$ mm in this case) which allows for a uniform plasma channel to be created. The pulse shape at the end of the 2 cm of plasma is shown in Figure 5.19. This shows that while considerable structure has been imposed by the fluctuations in the guiding profile density, it retains a shape which is much more regular than those at the lower density of 10^{18} cm^{-3}.

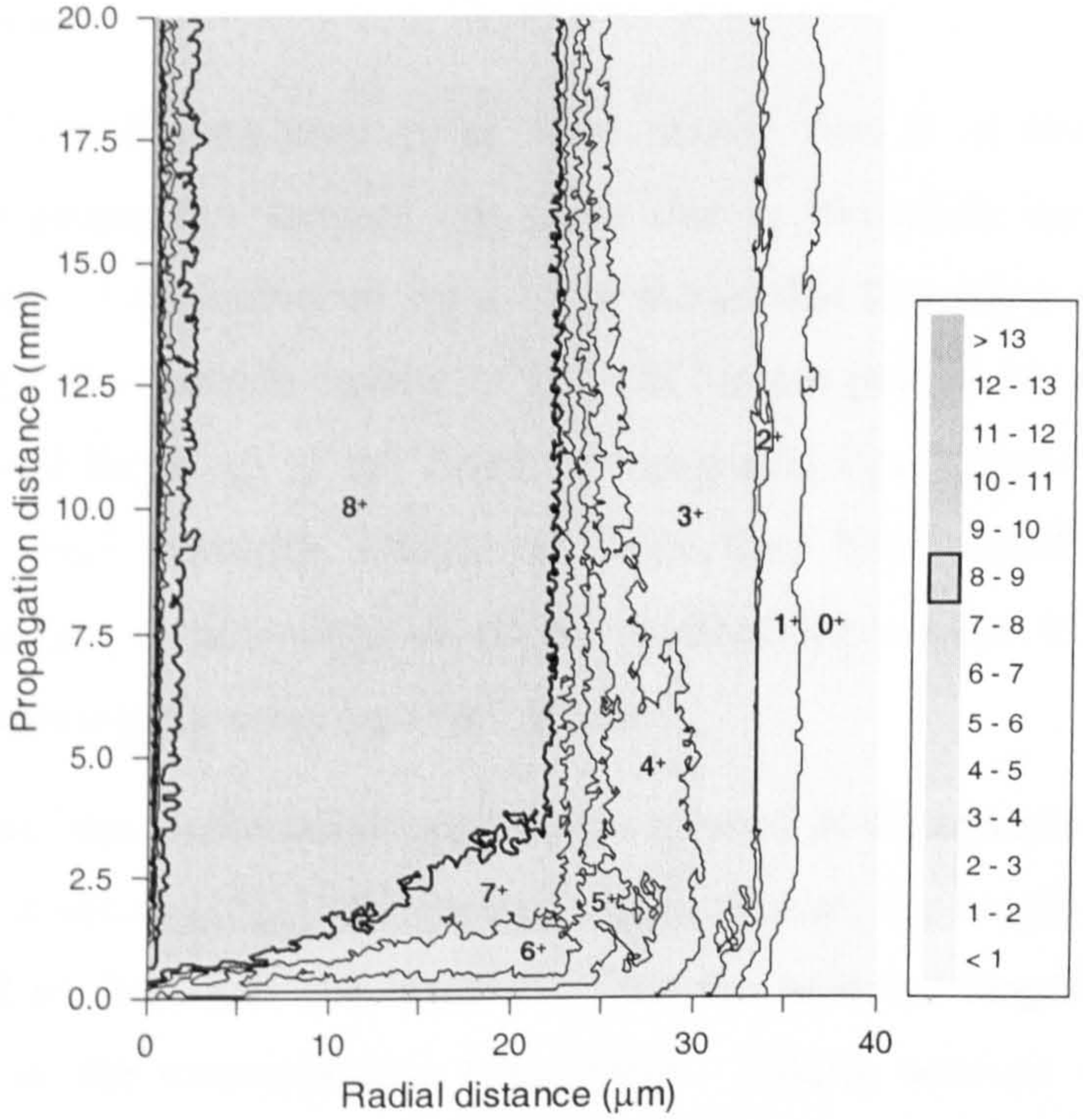

Figure 5.18. Plasma formed in a channel of matched radius 25 μm for argon at a density of 10^{19} cm^{-3} for a pulse of $I_{peak} = 5 \times 10^{17}$ W/cm^2. Regions of adjacent ionisation (up to Ar IX) are labelled with the charge state.

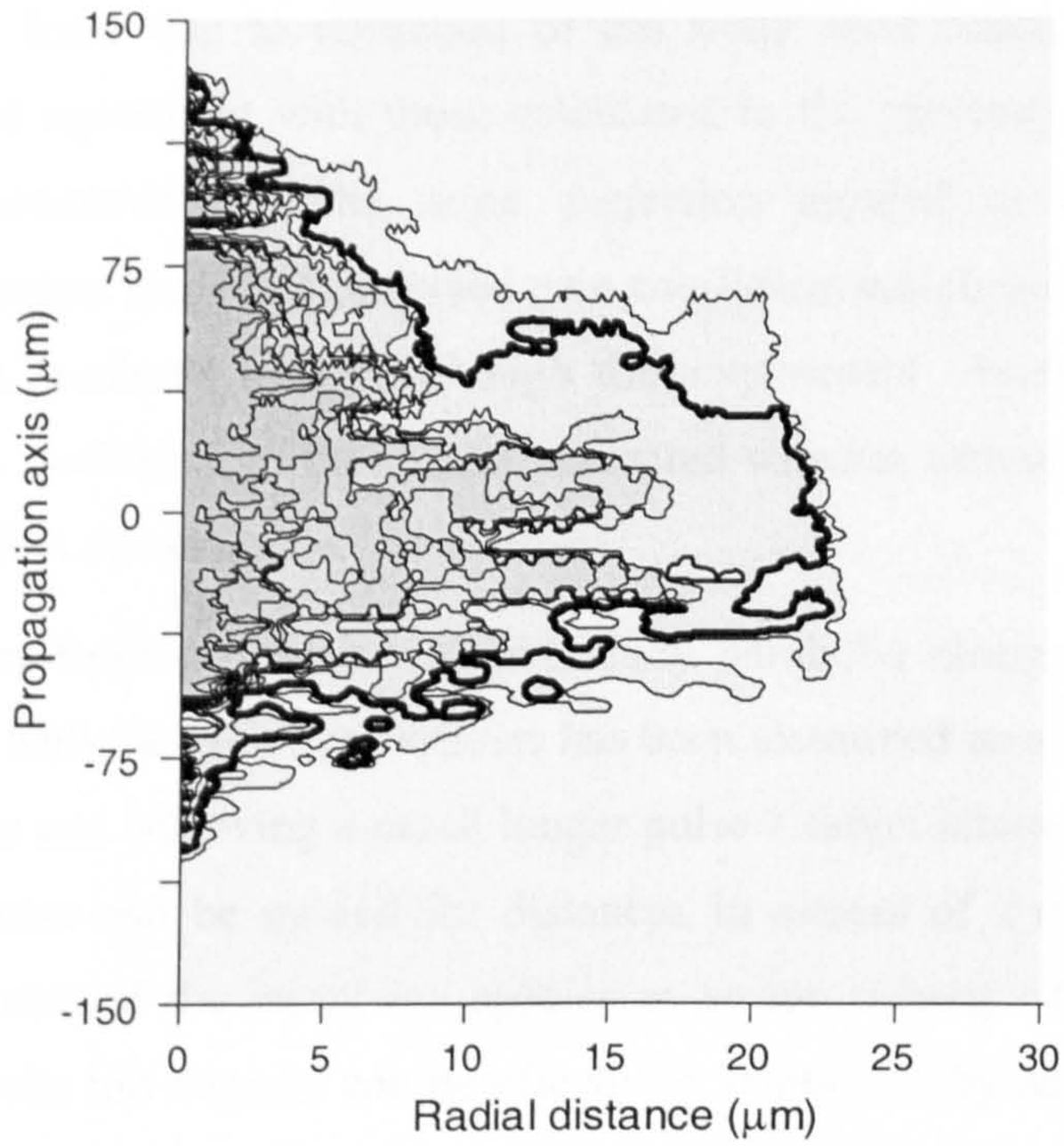

Figure 5.19. Pulse structure at the end of propagation into the parabolic channel with an argon density of 10^{19} cm^{-3}. (The same simulation as the above figure) The region enclosed by the bold contour is of sufficient irradiance to create Ar IX. All contours show 2×10^{16} W/cm^2 intervals.

5.5 Conclusions

Simulations of the driving laser pulse have shown that it is subject to severe refraction as it propagates through the gases due to ionisation and the resulting electron gradients. Simulations on argon have shown that forming a suitable plasma channel of Ar IX at a useable density of 10^{18} cm^{-3} is not practically possible due to refraction induced break up of the beam. Propagation into krypton and xenon is subject to the same refractive effects but since they have significantly smaller ionisation potentials, useable channels of the required species can be formed using irradiances of somewhat greater than 10^{17} W/cm^2.

Simulations have been presented for conditions as used in the reported lasing on the krypton [20] and xenon [17], [19] schemes. In each case, the length of the plasma channel formed of the lasant ion is shorter than the reported length of the lasing medium made in the corresponding experiment. Taking account of this factor, simple corrections to the reported gain coefficients have been made which lead us to believe that the reported gains are significantly under-estimated. These corrected gains for krypton [20] and xenon [19] are approximately half those predicted which, given expected loses due to refraction of the x-ray laser beam, bring them into reasonably good agreement with those calculated in the previous chapter from the BREAKDOWN simulations. The same correction applied to the Lemoff [17] experiment on xenon leads to a corrected gain coefficient which is around three times larger than that predicted here. Although this experiment observed lasing of the xenon line, it is unclear from the results presented whether saturation was achieved which would affect this estimate.

The use of a pre-formed plasma with a radially parabolic electron density profile which is doped with the lasant gas species has been examined as a means of guiding the driving pulse and achieving a much longer pulse – target interaction length. It is seen that the pulse can be guided for distances in excess of 2 cm while creating significant volumes of the lasant ion species at an ion density of 10^{18} cm^{-3}. The radius of the lasant ion channel can be effectively controlled by adjusting the depth of the parabolic guiding profile. The width of the x-ray laser output therefore may possibly be easily adjusted by propagating the driving laser into the pre-formed plasma channel at different times.

A simulation of argon at a density of 10^{19} cm^{-3} indicates that the formation of a considerable channel of Ar IX may be created using this technique. At this density, lasing on the inner sub-shell lines should be observable.

Chapter 6

Simulations of electron energy distributions

6.1 Introduction

Chapter 4 examined the gain coefficients and output intensities as determined from the BREAKDOWN code which assumes a thermal electron energy distribution (EED). This chapter now investigates the production and temporal evolution of the true EED following OFI and examines the validity of using thermal distributions in simulations.

The EED for Ar IX under a variety of driving pulse configurations is examined in order to determine the feasibility of producing an EED of arbitrary form in order that it can be "tuned" to suit the collisional pumping of the upper laser level. After briefly looking at the EEDs for Kr and Xe, those for the hydrogen mixtures previously examined for use in wave-guides are examined in order to determine how the inclusion of a significant low temperature electron component affects the overall EED. The computational work presented in this chapter has been obtained using the FPBREAKDOWN code which is briefly described next.

The complete Fokker – Planck with collisional – radiative and hydrodynamic calculations are computationally very expensive, particularly for realistic cases involving many tens or hundreds of radial mesh points. Time and computational constraints have meant that the scope of the simulations performed here has been curtailed and as such only a single radial cell at the centre of the pulse is examined, there is therefore no radial transport of the electrons. The requirements of integrating the EEDs over hundreds of velocity cells for the thousands of transitions involved has meant that no atomic calculations have been performed at present.

6.2 The FPBREAKDOWN code

The FPBREAKDOWN (Fokker – Planck BREAKDOWN) code is based upon BREAKDOWN and can be used in the same manner but includes the determination and evolution of the true EED following OFI of the gas. For each radial cell a velocity mesh is constructed which is used to track the number of electrons per ion in a range $u \rightarrow u + du$. The extent of this mesh is based upon calculations of the mean energy as obtained from the ANALYTIC package. The velocity cell widths need not be constant and indeed the code continually adjusts the velocity range and cell widths as the simulation proceeds in order to balance the opposing demands of accurate distribution representation and the limited cells available.

With the initial meshes prepared, OFI rates are calculated using the instantaneous rates at time steps throughout the pulse. ATI and IB heating are also calculated throughout the pulse. Note that this effective numerical integration over the pulse is in contrast to the ANALYTIC subroutines of BREAKDOWN which use cycle averaged rates.

The evolution of the EED is calculated from the Boltzmann equation (2.36) in the same 1D spatial geometry as for the hydrodynamics of BREAKDOWN with the velocity of the particles (only electrons are considered) taken as isotropic in the 1-D velocity space. For each radial cell the Fokker – Planck collisional term given by equation (2.37) is evaluated by the numerical scheme of Tingpin *et al* [116] which is more fully detailed with respect to OFI plasmas by Pert [65].

The Boltzmann equation is then numerically integrated along with the hydrodynamic and atomic calculations. With the EEDs available, the code is then able to use these to numerically integrate the collision rates for any transitions where the collision strengths as a function of energy are supplied. Any transitions for which collision strengths are not supplied use the van Wyngaarden form if data is provided or the van Regemorter if not. These rates assume a Maxwellian temperature of the same mean energy as the EED. This same mean temperature is used to calculate collisional ionisation rates. Finally, the effects of collisional ionisation upon the EEDs are included with released electrons being added to the distributions. The effects of

recombination, i.e. removal of electrons from the distributions, is not currently modelled and it is not important for this thesis.

6.3 Electron distributions of Ar IX

FPBREAKDOWN was run using identical pulse parameters as for the calculations of BREAKDOWN in Chapter 4 with a single radial cell representing the focus of the driving pulse at the peak intensity of 10^{17} W/cm^2. 400 velocity cells were used to sample the distribution at this point.

The work on the argon EED distributions is split into two parts. Firstly, the distribution at the spatial centre of the pulse is examined following the end of the driving pulse and its non-Maxwellian characteristics discussed. The possibilities of adjusting the EED through the driving beam polarisation to optimise the pumping rates of the lasing levels is considered. Secondly, the temporal evolution towards the Maxwellian distributions is discussed.

6.3.1 Electron energy distributions following the driving pulse

Electron distribution functions from Ar IX following OFI at ion densities of 10^{17}, 10^{18} and 10^{19} cm^{-3} are shown in Figure 6.1. Immediately at the end of the driving pulse at low density, the EED shows considerable structure that is almost noisy in nature. This is attributable to the fact that for circularly polarised light electrons are released at any point in the field cycle and with the rapid rise time of the pulse, the field strength changes significantly over that period thereby allowing a large range of electron energies to be produced by ATI heating. Although physically accurate and worthy of note, this effect is unlikely to be observed practically given that electron collisions will tend to quickly remove such small differences. This is observed in the simulations whereby this structure has been completely removed within 200 fs of the end of the pulse.

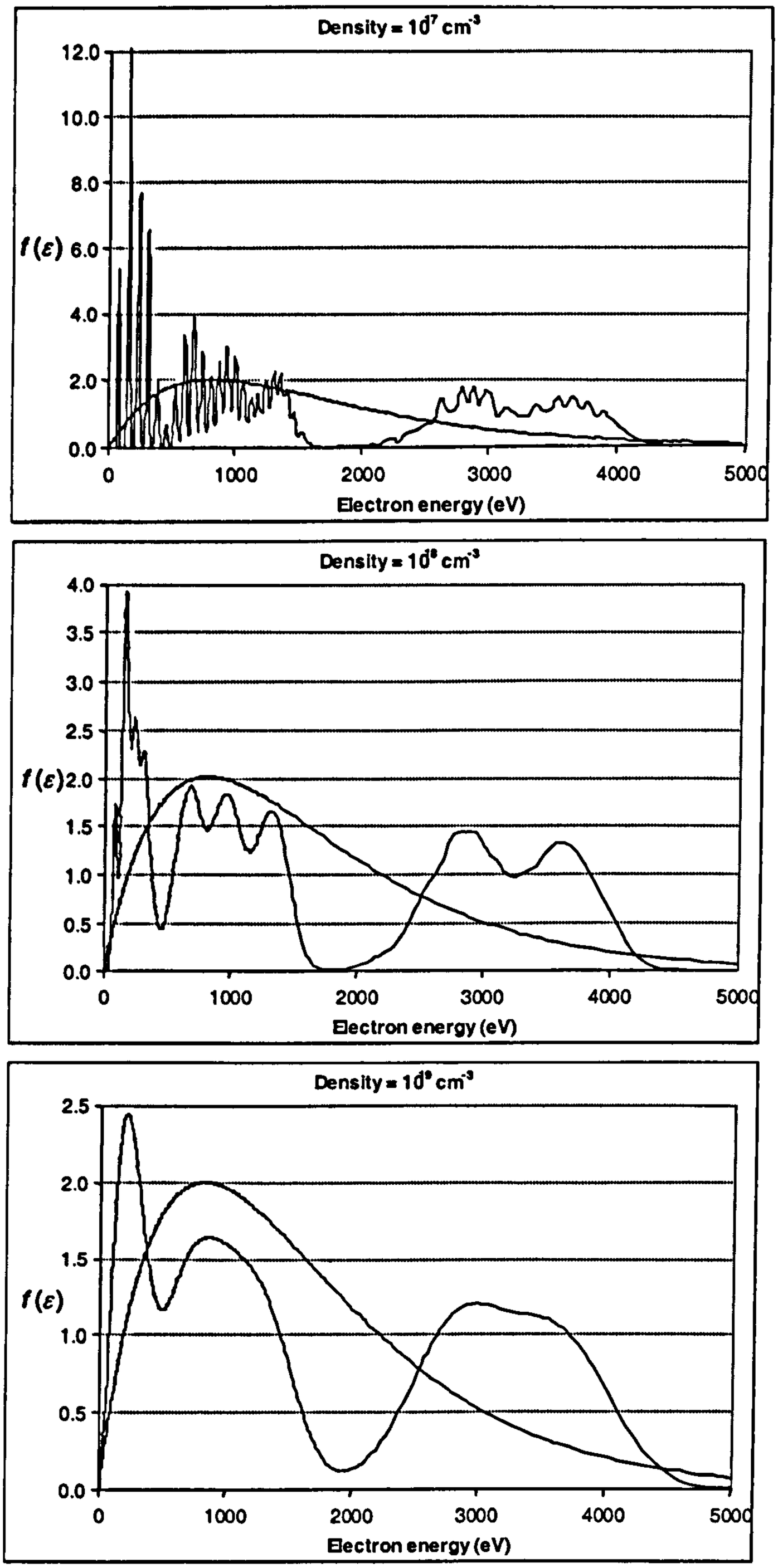

Figure 6.1. Electron distribution functions, $f(\varepsilon)$, from Ar IX following OFI by a pulse of HWHM 30 fs at the centre of a pulse of peak irradiance 10^{17} W/cm^2 at ion densities of 10^{17}, 10^{18} and 10^{19} cm^{-3}. $f(\varepsilon)$ is given in terms of the number of electrons per ion. Also shown are the Maxwellian distributions for the same mean energy. These are at a time immediately after the end of the driving pulse.

The effect is also made insignificant by the effects of inverse bremsstrahlung as shown in Figure 6.1 for ion densities of 10^{18} and 10^{19} cm^{-3}. Although section 4.3 showed that IB has a negligible effect on the overall mean electron energy, it is sufficient to broaden the peaks resulting from this structure. Despite the initial EEDs at densities of 10^{17} cm^{-3} and 10^{18} cm^{-3} looking very different, they have mean energies of 1224.23 eV and 1224.68 eV respectively. This energy difference is in good agreement with those listed in Table 4.2 for the cycle averaged ATI and IB rates.

It should be stated now that there is a significant difference between the electron energies as calculated by the cycle averaged rates used by BREAKDOWN / ANALYTIC and those calculated by the integration of rates over the entire pulse duration as done here in FPBREAKDOWN. Referring back to Table 4.2, then there is a difference of around 380 eV (and a corresponding temperature difference of around 250 eV) for argon. This effect has been found to be in the choice of the cut-off field strength used to calculate OFI rates at the very low fields early in the pulse (as discussed in presentation of BREAKDOWN in section 4.2). The complete temporal integration used by FBPREAKDOWN has allowed a smaller value to be used without numerical difficulties. As a result, ionisation is included here at lower field strengths resulting in lower ATI energies. This has illustrated the considerable variability of these collisionally pumped sytems to small deviations in pulse characteristics.

It is therefore acknowledged the electron pumping rates and hence the gains previously presented will be over-estimated. Exploratory BREAKDOWN simulations using these lower temperatures have shown that the gain coefficients are around 15 % smaller than those predicted in Chapter 4 for each of the gases. While this is considerable, the still large values are a consequence of the complete collisional / radiative model in which only the rates from the lower to the highest lying levels will be significantly altered. A compensating factor is shown in that the total lasing time is increased by a similar factor due to the weaker effect of collisional ionisation.

The non-thermal nature of the EED is clearly shown in Figure 6.1 and there are a number of important comparisons that can be made. Considering the ion density of 10^{18} cm^{-3}, then by simple numerical integration of the area under the two curves, then for the equivalent MB distribution, only 4.7% of the electrons have energies below the 280 eV needed to pump the upper laser level from the ground state. For the

correct EED, 12.0% of the electrons lie below this threshold meaning that there are fewer electrons able to pump the laser. Secondly, there is a considerable 'hole' in the distribution in the region around 1.5 to 2.5 keV compared to that of the MB. A glance at the two peaks at the tail of the distribution (which arise from ionisation of the two 3s electrons) would suggest that the greater proportion of hotter electrons in the 3 to 4 keV region would offset this hole to a large degree.

However, these electrons in the tail of the distribution will cause further detrimental effects to the pumping. This can be seen in the comparison of the collision strengths for transitions from the ground state to the upper and lower laser levels as shown in Figure 3.1. While the collision strength to the upper level remains larger than for the lower at all energies, it remains roughly constant from an energy of around 2.5 keV while the lower continues to rise strongly. Thus as the electron energy increases we expect the lower level to be populated more rapidly. We would ideally like to keep the electron temperature below around 2 keV in order to have the largest difference between the two pumping rates and thereby establish a larger population inversion.

Graphs showing the different EEDs available by changing the degree of polarisation of the driving laser from circular to linear are shown in Figure 6.2. These show that while there is a considerable proportion of the electrons below the threshold energy at all polarisations, the high energy tail can be removed. Also, the well defined structure resulting from each ionisation stage for circular polarisation is lost as the laser becomes more linearly polarised and the distribution becomes better approximated by the MB.

With a view to optimising the EED to pumping of the laser levels, it is more instructive to examine the relative proportions of electrons in various bands of energy. For the valence shell line then three groups can be identified; those below threshold for the upper level at 280 eV, those in the range 280 eV to around 2 keV and those above 2 keV where they will strongly pump the lower laser level. These proportions for driving beam polarisations from linear to circular are shown in Figure 6.3. This suggests that a large degree of ellipticity of around $\phi = 0.2$ to 0.3 may be required to significantly increase the proportion of electrons in the 280 eV to 2 keV region at the expense of the hotter electrons and without greatly increasing the number of electrons below the threshold energy.

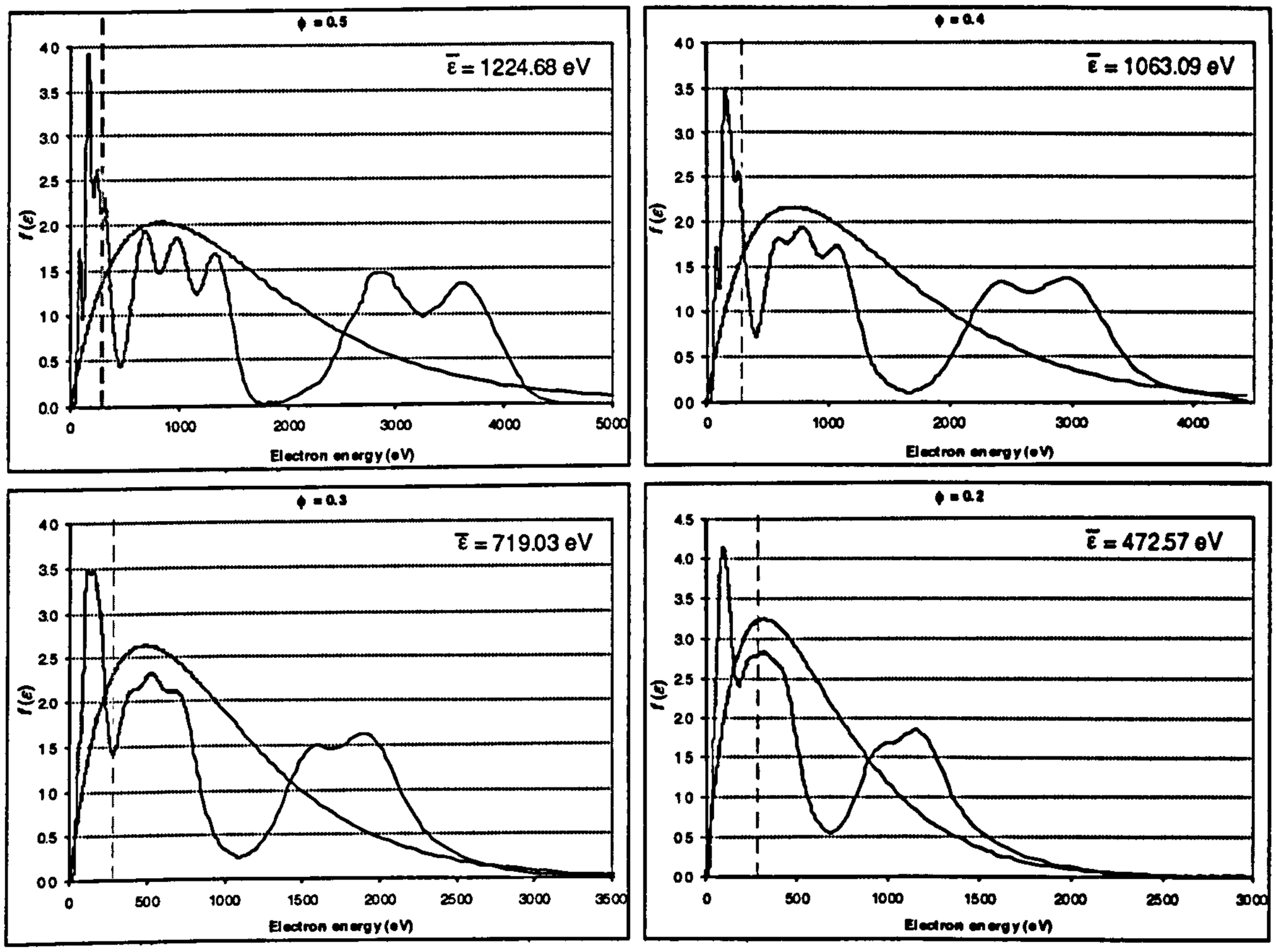

Figure 6.2. EEDs for argon at a density of 10^{18} cm^{-3} from pulses of circular through to linear polarisation. The mean electron temperature for each case is shown inset and a Maxwellian distribution of the same mean is plotted for each case. The vertical line at 280 eV is the energy required to pump the upper laser level from the ground state.

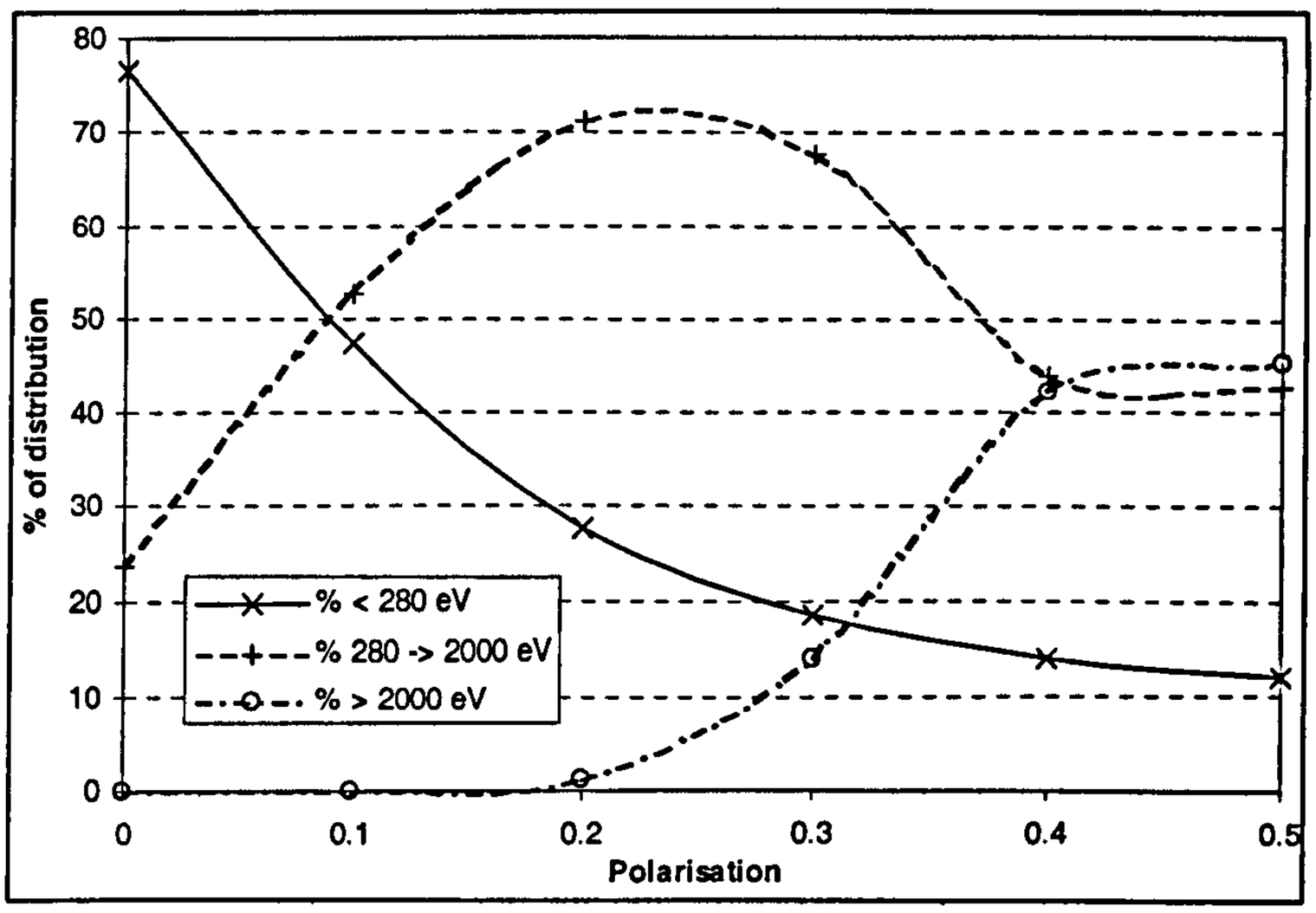

Figure 6.3. Relative proportions of important energy groups of electrons of Ar with respect to optimal pumping of the valence shell line for a range of laser polarisations from linear ($\phi = 0$) to circular ($\phi = 0.5$).

The above analysis can be performed for the inner-sub shell lines where the threshold energy for the upper level is 334 eV. The collision strength from the ground state to this level is again very flat from around 2 keV and the results obtained are similar to those for the valence shell line. Optimal pumping may be expected at polarisations in the range around $0.2 < \phi < 0.3$ where some 66 % of the total electron population lies in the energy range of 334 to 2000 eV. This compares to only 41 % in the same range for circular polarisation.

6.3.2 Electron thermalisation

The non-equilibrium EEDs produced by OFI will ultimately tend to the thermal MB distribution. The time taken to achieve this equilibration is important since any attempt to make use of the non-thermal nature of the true EED can only be considered worthwhile if the equilibration time scale is shorter than the characteristic gain life time. For the purposes of comparison, this latter time is taken to be the time of peak gain as predicted from the BREAKDOWN calculations of Chapter 4.

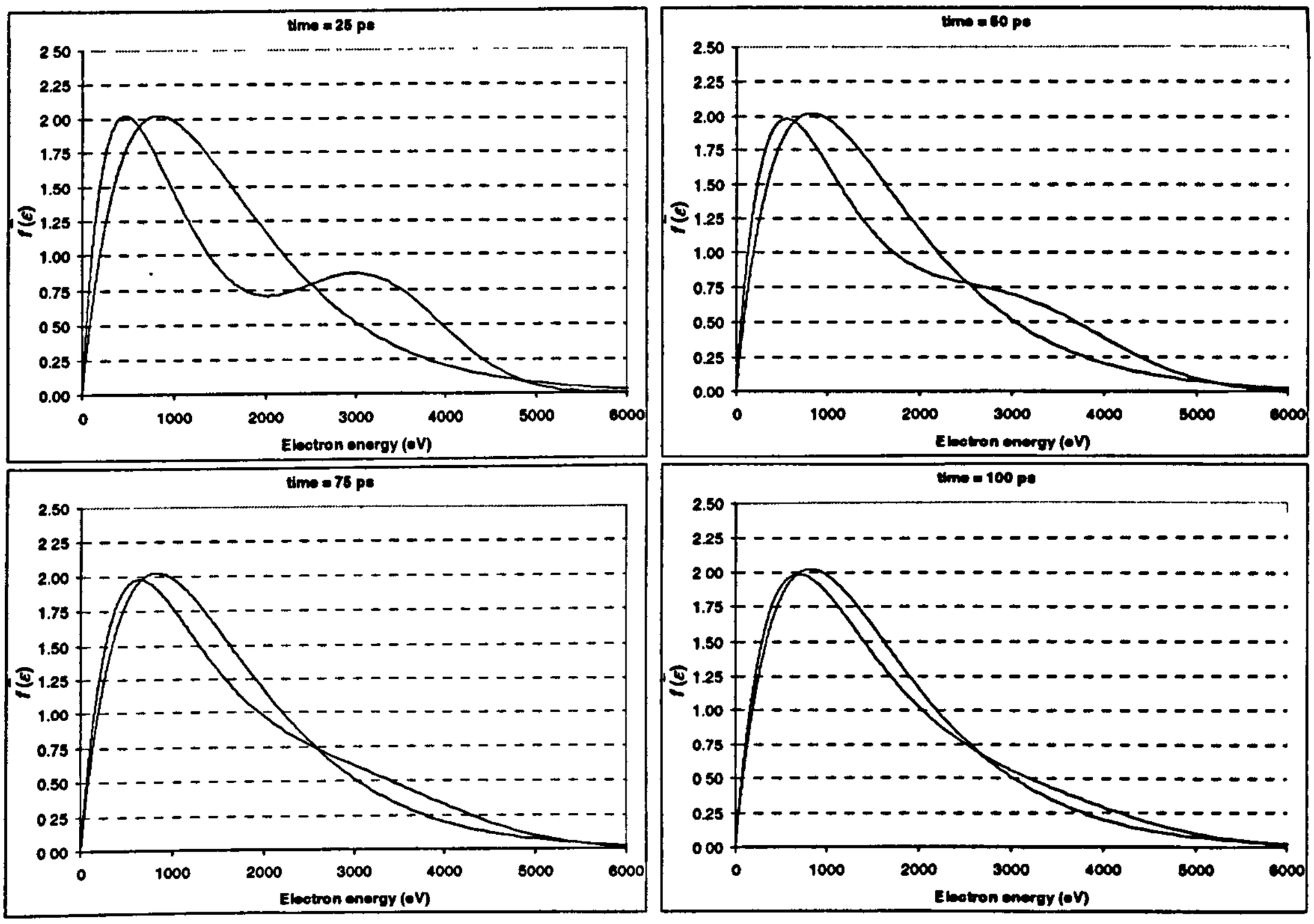

Figure 6.4. EEDs for argon at a density of 10^{18} cm^{-3} at times of 25, 50, 75 and 100 ps.

The above figures show that the EED takes around 100 ps to approach the MB at an ion density of 10^{18} cm^{-3} while it remains characterised by a smaller proportion of cooler electrons and larger proportion of hotter electrons in the tail of the distribution than the equivalent MB. BREAKDOWN predicts that the time of peak gain for this density is 9.2 ps and we can therefore predict that this non-thermal distribution may have significant effects upon the atomic level populations over the gain lifetime. The Spitzer electron self collision time, t_{ce}, for the same temperature (~ 810 eV in this case) is 14 ps. An estimate of the thermalisation time using this is therefore approximately an order of magnitude too small. A more detailed breakdown of the comparison of these times for a range of argon targets is given in Table 6.1.

This table lists the times required for the exact EED to thermalise to the MB as predicted by the single cell FPBREAKDOWN simulations for a range of target densities and driving pulse polarisations. In each case this time is around 15 times the Spitzer electron self collision time and is always considerably longer than time of peak gain on the valence shell line. These equilibration times will be larger than the real case since radial transport is absent from these calculations. Exploratory simulations with

radial transport at a low spatial and velocity resolution suggest that these times should be reduced by a factor of 2 to 3 times.

Density (cm^{-3})	Pulse ϕ	T_e (eV)	t_{ce} (ps)	t_{peak} (ps)	t_{eq} (ps)
10^{17}	0.5	816.3	135	51.5	>1250
10^{18}	0.5	817.4	13.9	9.22	190
10^{18}	0.4	708.8	11.3	9.20	150
10^{18}	0.3	479.6	6.48	9.02	100
10^{18}	0.2	315.2	3.45	-	55
10^{18}	0.1	178.2	1.50	-	30
10^{18}	0.0	59.0	0.30	-	12
10^{19}	0.5	829.1	1.46	1.84	30

Table 6.1. Electron temperatures, T_e, Spitzer electron self collision times, t_{ce}, time for the peak gain, t_{peak}, and the time taken for the true EED to equilibrate to the Maxwellian, t_{eq}, for a range of argon targets.

Even with this additional reduction, the EEDs are still non thermal for considerably longer periods of time than the time of peak gain as predicted by BREAKDOWN. Thus providing that calculations with the true EED do not significantly alter the time of the peak gain, then more detailed calculations with the non thermal distributions may be worth consideration.

6.4 Electron distributions of Kr IX and Xe IX

The EEDs for krypton and xenon under the same pulse conditions as examined for argon with circular polarisation are shown in Figure 6.5 and are qualitatively similar in that they show a number of distinct ionisation peaks at low energies with a high energy tail resulting from ionisation of the final two electrons.

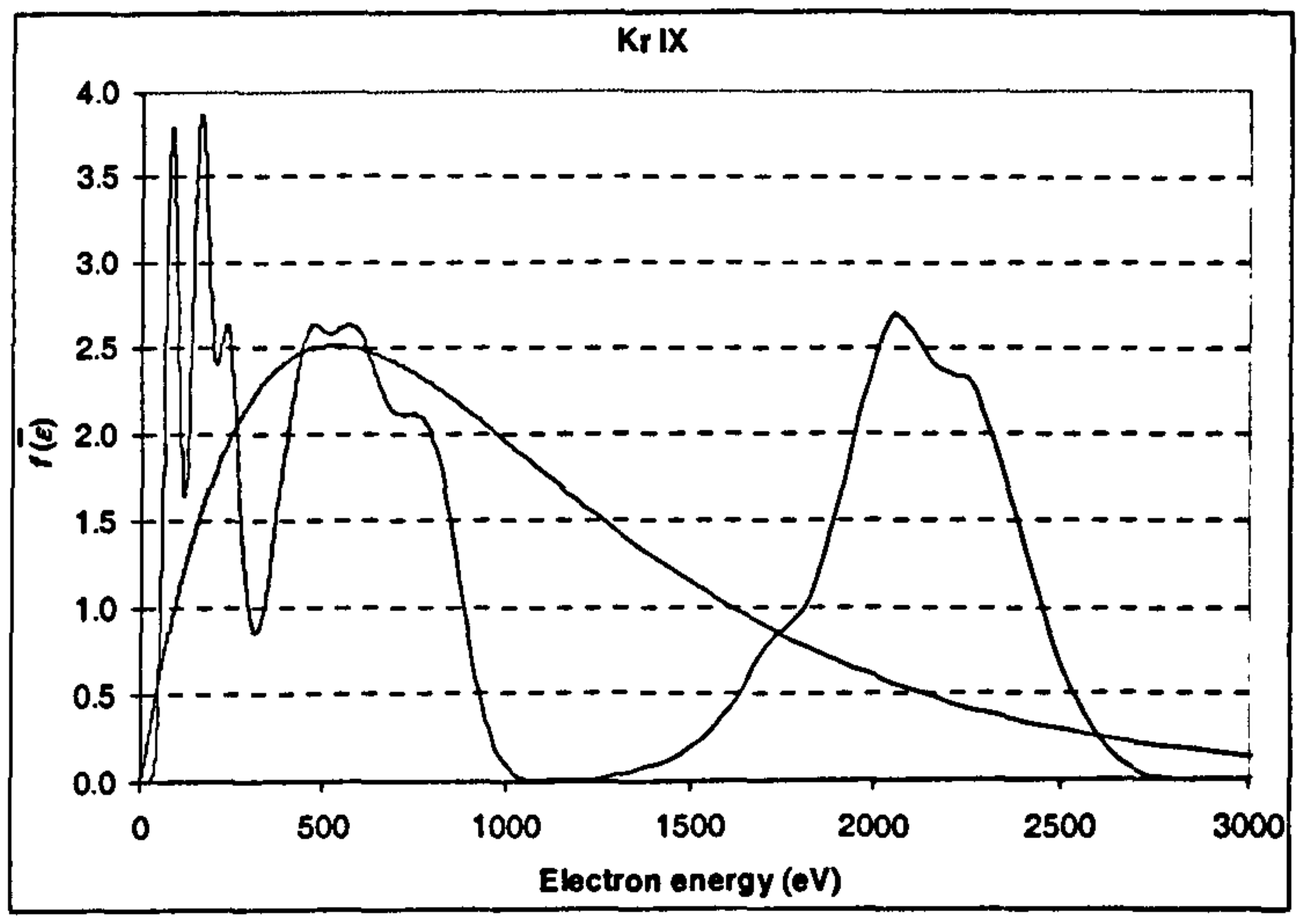

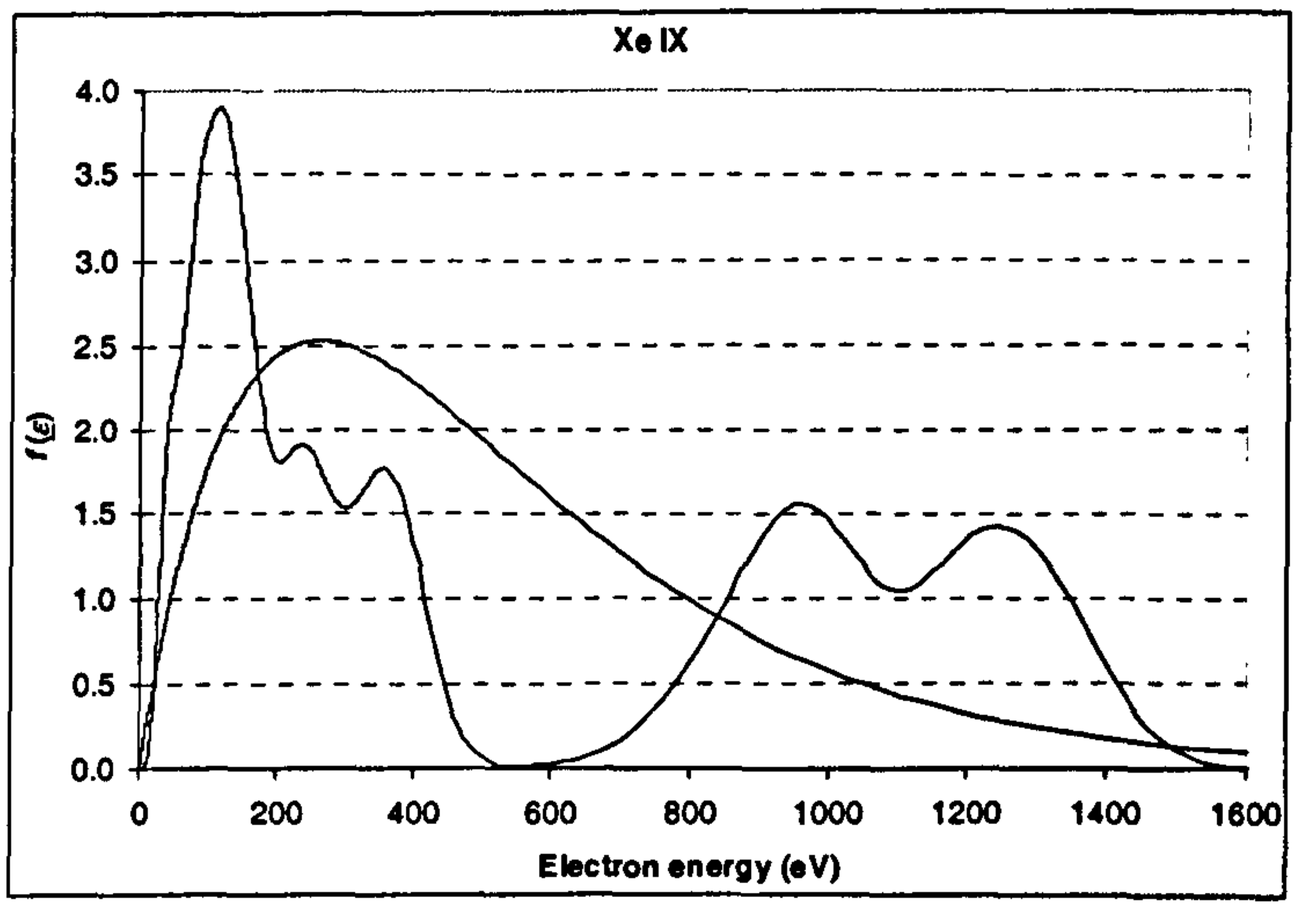

Figure 6.5. EEDs for Kr IX and Xe IX at the centre of a driving pulse of peak intensity 10^{17} W/cm^2 for ion densities of 10^{18} cm^{-3}.

The collision strengths for the lasing levels of Kr IX and Xe IX presented in section 2.9.4 showed that at lower electron energies the lower laser level would be more strongly pumped than the upper from the ground state. It is clear from the above figures that both the Kr IX and Xe IX EEDs have a considerably larger proportion of electrons at lower energies than the equivalent MB.

For Kr IX, this detrimental pumping occurs for electron energies of less than 450 eV. The true EED contains 24.8 % of the electrons below this point compared to 20.7 % for the equivalent MB distribution. For Xe IX, where this point lies at 180 eV, the corresponding figures are 25.4 % for the true EED and 13.4 % for the MB. This means that there is likely to be a significant error involved in the gain calculations for Xe IX which assume a MB distribution.

For argon, possible optimisation of the EED to the pumping rates by use of the pulse polarisation was identified. No such process is possible for krypton and xenon since changing the polarisation from circular to elliptical can only produce cooler electrons at the expense of the hotter tail. For these two systems, the nature of the collision strengths would suggest that higher electron energies are desirable for the creation of the largest population inversions which cannot be achieved using any of the driving pulse parameters investigated here.

A final difference of note between the EEDs for the three gases is that the effects of IB are most apparent in xenon and least so in argon (compare Figure 6.5 with that for argon at 10^{18} cm^{-3} in Figure 6.1). The smaller ionisation potentials of xenon than krypton and in turn argon, mean that electrons are released earlier in the pulse duration and therefore have more time to absorb energy through IB. As a result, the EED curve for xenon at 10^{18} cm^{-3} shows none of the individual peaks due to the loosely bound electrons that are visible in the krypton and argon graphs.

6.5 Noble gas / hydrogen mixtures

The previous chapter identified that a pre-formed plasma with a radial parabolic profile which is doped with a noble gas should allow for a considerable length of lasing plasma to be formed. This pre-plasma will consist of electrons which are of a different energy distribution to those released from the noble gas by OFI and will therefore affect the pumping rates as equilibration occurs between the two groups. For a pre-plasma which is created by a capillary discharge, the ohmic heating produces an energy distribution which is thermal in nature. Of the experimental results published which demonstrate optical guiding of laser pulses, only Ehrlich *et al* [106] have measured the electron temperature of the plasma where they determined it to be around 3 eV on the plasma axis at electron densities of 1 to 5 $\times 10^{18}$ cm^{-3}.

FPBREAKDOWN has been run with the conditions used to investigate guiding in the previous chapter with argon at a density of 10^{18} cm^{-3}. Once the EED due to OFI of the argon has been calculated, a hydrogen plasma of density 2.72×10^{18} cm^{-3} is included which has a MB distribution of temperature 3 eV. The calculations then proceed to determine the evolution of this combined distribution.

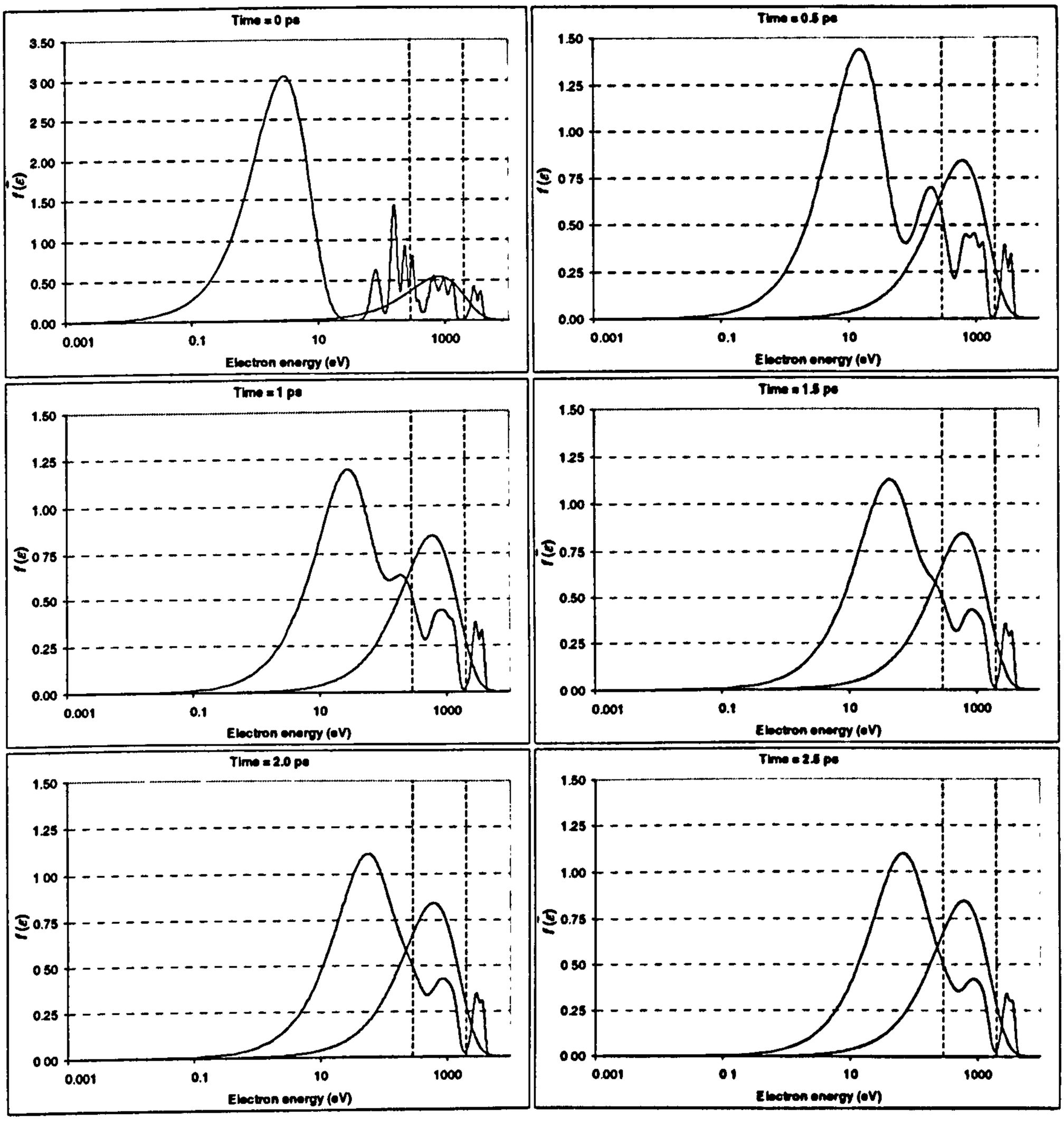

Figure 6.6. Temporal development of the EEDs for argon at 10^{18} cm^{-3} following OFI with a thermal hydrogen component of temperature 3 eV. The vertical dashed lines indicate energies of 280 and 2000 eV. Note that the energy axis is logarithmic in scale.

Figure 6.6 shows the EED for this mixture and it's development up to 2½ ps following the driving pulse. Initially the hydrogen component is distinctly separate from the argon but the two rapidly merge. While the low energy electrons themselves cannot pump the lasing levels and will act to cool the distribution as a whole, these results show that they can actually increase the proportion of electrons in the energy range of 280 to 2000 eV where optimal pumping of the upper (valence) level should occur. The large number of cold electrons effectively cools those in the high energy tail beyond 2 keV without significantly reducing the proportion in this energy range.

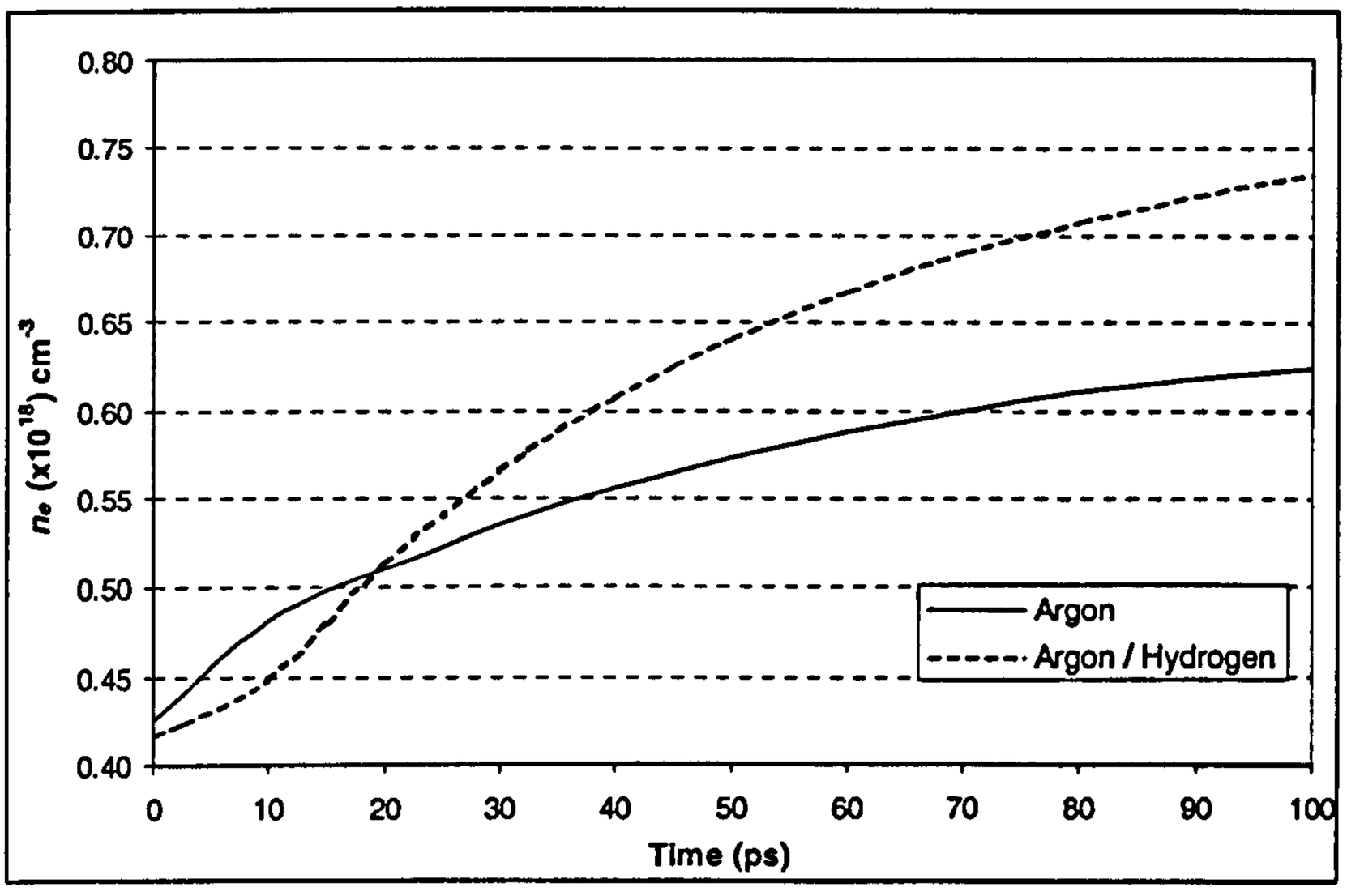

Figure 6.7. Electron density of those in the energy range 280 to 2000 eV for argon and an argon / hydrogen mixture in the ratio 1:2.7 mixtures as a function of time. The Ar / H mixture initially consists of an OFI produced Ar distribution with a 3 eV thermal component. The total electron density is the same for both cases.

Comparing the longer term development of the electrons in the range 280 to 2000 eV for argon at 10^{18} cm^{-3} and argon at the same density in hydrogen of 2.72×10^{18} cm^{-3} shows that the number in this range is increased for the mixture as shown in Figure 6.7. More efficient pumping of the x-ray laser should therefore occur in mixtures which act to remove the high energy tail.

Given the nature of the collision strengths for the lasing levels in krypton and xenon, the same affect is expected to reduce the size of the population inversion that can be formed. The use of these wave-guides should therefore reduce the effectiveness of the X-ray output although the much longer interaction length will be of more significance.

6.6 Conclusions

This chapter has investigated the nature of the true EED which is produced by the optical driving laser. For each of the three noble gases, considerable deviation from an equivalent thermal Maxwell-Boltzman (MB) distribution has been found which is expected to significantly affect the collisional pumping of the x-ray laser levels. The time scale over which the true EED evolves towards the equilibrium MB indicates that these should be used in preference to the MB in order to accurately determine the atomic level populations.

For krypton and xenon it has been found that the true EED will result in a greater proportion of electrons in the energy region where pumping from the ground state to the lower laser level will exceed that to the upper. In these cases, calculations based upon a thermal distribution will over-estimate the gain coefficients. Changing the driving pulse polarisation for these gases will not result in an EED which can improve the lasing conditions.

For argon, the situation is found to be different given that the electron collision strength from the ground state to the lower level increases much faster than that to the upper (valence) at energies above around 2 keV. Here it is found that optimal pumping of the upper level should occur for pulse polarisations in the range of $0.2 < \phi < 0.3$.

The EED for the hydrogen based wave guide doped with argon at a density of 10^{18} cm^{-3} was investigated with the result that equilibration of the high energy tail with the cold hydrogen electrons would act to increase the number of electrons which could be expected to effectively pump the laser.

Chapter 7

Conclusions and further work

The work presented in this thesis represents a detailed investigation into key areas of physics relating to the use of optical field ionisation as an alternative mechanism of creating the required conditions to generate soft X-ray lasing through collisional excitation. A number of computational codes have been used which now allows for the feasibility of this scheme to be discussed.

7.1 Conclusions

Chapter 3 firstly presents the atomic data necessary to model lasing in Ar IX, Kr IX and Xe IX. The atomic code of Cowan [68] was used to calculate all atomic energy levels from the ground state of the ion up to those approaching the ionisation limit. Radiative transition and collisional excitation rates between these levels were also calculated.

Only limited direct validation of the data produced was possible but does indicate that the level energies and radiative rates can be considered sufficiently accurate for the work in this thesis. The electron collision strengths are less accurate and reproduce only the general trend to an accuracy of around 25%. Given the current experimental uncertainties due to poorly characterised driving lasers and problems in determining the length of the lasing region, this level of accuracy in the complete collisional / radiative model is sufficient for current experimental comparisons.

Chapter 4 presents results obtained from an atomic / hydrodynamics code which models the plasma following OFI of the gas. The complete collisional / radiative model COLRAD has enabled accurate calculations of the temporal development of the gain coefficients and saturated irradiances in the three noble gas schemes to be made for the first time.

Large gain coefficients of the order ~100 to ~1000 cm^{-1} are predicted for target densities in the range 10^{17} to 10^{19} cm^{-3}. At an indicative density of 10^{18} cm^{-3}, the peak gains resulting from transitions in the valence shell of the ions are found to be 554, 665 and 1414 cm^{-1} for argon, krypton and xenon respectively. Those for the inner sub shell lines of argon at 15.3 and 15.7 nm are 18.6 and 20.0 cm^{-1} respectively. The gain duration at this density is around 10 to 20 ps for each line.

At densities below 10^{18} cm^{-3} for argon and krypton, the gain duration is limited by the electron cooling through thermal conduction with adjacent regions of colder plasma. At higher densities, collisional ionisation acts to restrict the gain duration to less than 10 ps. However, the same process can also create useable regions of the lasant ion in regions adjacent to that created by the OFI pulse. Gains of around 100 cm^{-1} are produced in these regions in argon at a density of 10^{18} cm^{-3}.

The saturation irradiances are small with values of a few 10^{7} W/cm^{2} at a density of 10^{18} cm^{-3}. These low values are largely attributable to the very narrow line widths associated with the lasing transitions. At low densities, doppler broadening is shown to dominate and since the ions effectively remain at room temperature the saturation irradiance is small. At higher densities collisional broadening dominates. High densities naturally create large gains and saturated irradiances through the stronger collisional pumping of the levels, however the densities are still relatively low compared to solid target systems and the line width is still narrow enough to limit the saturated irradiance.

The temporal evolution of the saturated irradiance has allowed an estimate of the energy available from the X-ray laser to be made. For argon at 10^{18} cm^{-3}, output energies of 109, 150 and 356 nJ are predicted for the 46.9, 15.3 and 15.7 nm lines respectively. These values are indicative of the stability against collisional ionisation of argon thereby allowing lasing for long periods. Output energies of 23 and 17 nJ for krypton and xenon under the same conditions are predicted. The efficiency of these schemes is low by collisional excitation standards at around 10^{-7} to 10^{-6}.

The use of an elliptically polarised driving laser was examined which produces gains that are moderately smaller than those produced using circular polarisation. The saturation irradiances are correspondingly slightly larger. The main effect of interest

in this case is the creation of a volume of the lasant ion which is two or three times larger in radius in the case of argon than for circular polarisation.

Chapter 5 presents the results of simulations of the propagation of the driving pulse into the gas / plasma. It is found that refraction of the beam by the ionisation induced electron gradients is severe. Only at densities below 10^{18} cm^{-3} can significant regions of the lasant ion be produced. Producing a significant volume of Ar IX is the most difficult of the three gases investigated due to its much larger ionisation energies.

Although the following chapter on electron energy distributions has indicated that the BREAKDOWN calculations will have over-estimated the gain coefficients, propagation simulations for the reported observations of lasing in krypton and xenon have identified the cause of the considerable differences in our calculated values and those measured experimentally. These calculations have shown that lasing over the lengths estimated experimentally is not possible given the conditions reported and has led to a significant underestimation of the gain coefficient. Simple corrections have shown that lasing probably occurred with coefficients that are in good agreement with those predicted here.

The use of a pre-formed plasma with a radially parabolic electron density profile which is doped with the lasant gas species has been examined as a means of guiding the driving pulse and achieving a much longer pulse – target interaction length. Considerable lengths (many times the Rayleigh length) of the appropriate lasant ion can be created at ion densities of 10^{18} cm^{-3} and greater. This approach may also enable relatively easy control of the radius of the x-ray laser output. This method should be of particular interest to the argon scheme given that it would allow for plasmas of sufficient length to be created to observe lasing on the inner sub-shell lines.

Chapter 6 discusses the non-thermal nature of the EEDs which result from OFI and the subsequent ATI and IB heating. Considerable non-thermal structure is found in all three cases which persists for much longer than the gain duration predicted on the basis of thermal distributions.

At this point it was found that the cycle averaged OFI, ATI and IB rates in the ANALYTIC routines of BREAKDOWN has resulted in electron temperatures which are

around 20% too high. The gain and saturation irradiance coefficients previously calculated will therefore be too high by a similar factor, while at higher densities, the total lasing time will be longer than predicted due to reduced collisional ionisation. Although unfortunate, this error does not invalidate any of the general statements made in Chapter 4, but will lead to a better agreement with the corrected gain coefficients of Chapter 5.

For argon then a degree of ellipticity in the driving laser should allow for more efficient pumping of the laser than is obtainable from a circularly polarised laser. The same is not expected to be true for krypton and xenon where the nature of the collision strengths suggest that preferential pumping of the lower laser level would occur at the lower electron energies that would result from an elliptically polarised laser.

Finally, the EED for the hydrogen based plasma wave-guide for argon was investigated. Here it was found that the considerable number of low energy electrons formed by the capillary discharge measured by Ehrlich *et al* [106] could be expected to further increase the pumping efficiency of the upper level by rapidly cooling the high energy electrons which result from the ionisation of the 3s electrons.

In summary, large gain coefficients, but relatively low saturated irradiances are predicted. Using a driving laser that is elliptically rather than circularly polarised will increase the efficiency of the X-ray laser output by producing a larger volume of the lasant ion. For argon, analysis of the true EED predicts further enhancement of the lasing output.

Ionisation induced refraction is found to be a considerable limiting factor on these schemes due to the long wavelength of the driving laser. The use of pre-formed wave-guides doped with the lasing gas may prove to be an attractive solution and allow consider lengths of lasing plasma to be formed.

The EEDs have been examined for the conditions used throughout this thesis and it is suggested that more accurate calculations of the atomic processes involved would be obtained from using the exact form as opposed to a thermal distribution.

7.2 Further work

A number of areas have been identified throughout this thesis which would benefit from further work. Perhaps the most significant of these is the use of the true EED rather than MB distributions in any atomic calculations. The computation demands required are considerable but are now within the scope of the more modest workstations that are becoming available.

It is suggested that for such calculations to be worthwhile that more accurate electron collision strengths be first determined. Those used in this thesis are fairly crude and reproduce only the general trend. The combination of the true EED and collision strengths which include the resonant structure which is experimentally present, may suggest new possibilities of matching the EED to some optimal pumping rate.

Propagation of the driving laser into the gas / plasma has been examined here but no attempt has been made to do so for the X-ray output. Ray tracing calculations would indicate how the X-ray laser is affected by the conditions within the plasma and would give an important measure of the degree of divergence that is expected from these devices.

The use of parabolic wave-guides has been investigated and it is has been found that the half radial code used produces what appear to be non-physical affects. For accurate simulation of these wave guides it is therefore suggested that calculations are performed which use the full beam radius.

It has been found that the driving laser peak intensity required to create useable volumes of the lasant ion is significantly above 10^{17} W/cm^2 and indeed that used to recently demonstrate lasing in the krypton [20] system is above 10^{18} W/cm^2. At these intensities, relativistic effects should be considered. This should be examined in two contexts. Firstly, if effort is being made to use the true EEDs in atomic calculations then the >1% shift in the distribution should be considered. Secondly, propagation of the driving laser will be affected by the relativistic mass increase of the electrons. Although the intensities are below the ~10^{20} W/cm^2 required for complete relativistic self focusing of the laser, the refractive index of the plasma will be altered sufficiently to affect the beam propagation and may be important in any future study of wave-guiding structures for OFI schemes.

The variability of the overall electron temperature upon the exact characteristics has been demonstrated by the differences observed between the BREAKDOWN and FPBREAKDOWN models. A detailed analysis of the effects of the pulse shape would be beneficial.

Finally, further experimental characterisation and validation of these schemes is required. Optical lasers are now available that have the power to create small volumes of the lasant ion even given the problems of refraction. This should allow for a greater investigation of the physical conditions which occur in these plasmas.

Measurements of the true EED resulting from these systems would provide valuable insights into the nature of the lasing plasma which may allow for more efficient schemes to be designed. These measurements would also be of considerable importance if detailed measurements of the exact pulse shape could also be obtained.

Work to demonstrate the feasibility of the plasma wave-guide for use as a lasing medium in these OFI schemes may finally enable the demonstration of a true "table-top" X-ray laser.

Bibliography

[1] T. H. Maiman, *Stimulated optical radiation in ruby*, Nature, **187** 493 (1960).

[2] D. L. Matthews, P. L. Hagelstein, M. D. Rosen, M. J. Eckart, N. M. Ceglio, A. U. Hazi, H. Medecki, B. J. MacGowan, J. E. Trebes, B. L. Whitten, E. M. Campbell, C. W. Hatcher, A. M. Hawryluk, R. L. Kauffman, L. D. Pleasance, G. Rambach, J. H. Scofield, G. Stone and T. A. Weaver, *Demonstration of a soft X-Ray amplifier,* Physical Review Letters, **54** (2) 110 (1985)

[3] A. Carillon, H. Z. Chen, P. Dhez, L. Dwivedi, J. Jacoby, P. Jaegle, G. Jamelot, J. Zhang, M. H. Key, A. Kidd, A. Klisnick, R. Kodama, J. Krishnan, C. L. S. Lewis, D. Neely, P. Norris, D. O'Neill, G. J. Pert, S. A Ramsden, J. P. Raucourt, G. J. Tallents and J. Uhomoibhi, *Saturated and near diffraction limited operation of an XUV laser at 23.6nm*, Phys. Rev. Lett, **68** (19) 2917 (1992)

[4] J. G. Lunney, *Waveguiding in soft X-ray laser experiments*, Appl. Phys. Lett. **48** (14) 891 (1986)

[5] J. A. Plowes, G. J. Pert and P. B. Holden, *Refraction compensation by target curvature in X-ray lasers,* Opt. Comm. **116** 260 (1995)

[6] J. A. Plowes, G. J. Pert, S. B. Healy and D. T. Toft, *Beam modelling for X-ray lasers*, Opt. and Quant. Elect. **28** (3) 219 (1996)

[7] S. B. Healy, G. F. Cairns, C. L. S. Lewis, G. J. Pert and J. A. Plowes, *A computational investigation of the neon like germanium collisionally pumped laser considering the effects of prepulses*, IEEE Journal of Selected Topics in Quantum Electronics, **1** (3) 949 (1995)

[8] J. A. Plowes, G. J. Pert and P. B. Holden, *Double pulse irradiation of X-ray laser targets*, Opt. Comm. **117** 189 (1995)

[9] M. P. Kalachnikov, P.V. Nickles, M. Shnürer, W. Sander, V. N. Shlyaptsev, C. Danson, D. Neely, E. Wolfrum, J. Zhang, A. Behat, A. Demir, G. J. Tallents, P. J. Warwick and C. L. S. Lews, *Saturated operation of a transient collisional x-ray laser*, Phys. Rev. A, **57** 4778 (1998)

[10] J. Zhang, E. Wolfrum, A. MacPhee, J. Lin, M. H. Key, C. L. S. Lewis, J. Nilsen, R. M. N. O'Rourke, R. Smith, G. J. Tallents and J. S. Wark, *Experiments of the saturated Ni-like X-ray lasers driven by a double 75ps laser pulse*, X-Ray Lasers 1998, Inst. Of Phys. Conf. Ser. No 159, IOP Publishing Ltd, pp.67 (1999).

[11] R. Smith, G. J. Tallents, J. Zhang, G. Eker, S. McCabe, G. J. Pert, and E. Wolfrum, *Saturation behavior of two x-ray lasing transitions in Ni-like Dy*, Phys Rev A, **59** R47 (1999)

[12] J. J. Rocca, V. N. Shlylaptsev, F. G. Tomasel, O. D. Cortazar, D. Hartshorn and J. L. A. Chilla, *Demonstration of a discharge pumped table-top soft X-ray laser*, Phys. Rev. Lett. **73** 16 (1994)

[13] J. J. Rocca, D. P. Clarke, J. L. A. Chilla, V. N. Shlylaptsev, *Energy extraction and achievement of the saturation limit in a discharge pumped table-top soft x-ray amplifier*, Phys. Rev. Lett. **77** 1476 (1996)

[14] J. J. Gonzalez, M. Frati, J. J. Rocca and V. N. Shlylaptsev, *First experimental results of a very high power density capillary discharge*, X-Ray Lasers 1998, Inst. Of Phys. Conf. Ser. No 159, IOP Publishing Ltd, pp.159 (1999).

[15] F. G. Tomasel, J. J. Rocca, V. N. Shlylaptsev and C. D. Macchietto, *Lasing at 60.8 nm in Ne-like sulfur ions in ablated material excited by capillary discharge*, Phys. Rev. A, **55** 2 (1997)

[16] B. E. Lemoff, C. P. J. Barty and S. E. Harris, *Femtosecond pulse driven, electron excited XUV lasers in eight times ionised noble gases*, Optics Letters, **19** (8) 569 (1994).

[17] B. E. Lemoff, G. Y. Yin, C. L. Gordon III, C. P. J. Barty and S. E. Harris, *Demonstration of a 10 Hz femtosecond pulse driven XUV laser at 41.8 nm in Xe IX*, Phys. Rev. Letters, **74** (9) 1574 (1995).

[18] T. Mocek, H. J. Shin, Y. H. Cha, D. G. Lee, K. H. Hing, C. H. Nam, H. Fiedorowicz, A. Bartnick and M. Szczurek, *Investigation on a femtosecond-laser-driven soft X-ray laser using a gas puff target*, X-Ray Lasers 1998, Inst. Of Phys. Conf. Ser. No 159, IOP Publishing Ltd, pp.329 (1999)

[19] Ph. Balcou, S. Sebban, R. Haroutunian, A. Rousse, G. Grillon, J-Ph Rousseau, L. Notebaert, M. Pittman, J-P Chambaret, D. Hulin, A. Klisnick, D. Ros, P. Jaegle, A. Carillom, G. Jamelot, *Femtosecond laser driven XUV sources, High harmonic and OFI X-Ray laser studies*, 7th International Conference on X-Ray Lasers, St. Malo, France 18-23 July 2000.

[20] S. Sebban, Private communication, (2001)

[21] P. Lu, H. Nakano, T. Nishikawa and N. Uesugi, *Design of a 1Tw/100fs laser driven Ne-like S x-ray laser at 60.8nm*, X-Ray Lasers 1998, Inst. Of Phys. Conf. Ser. No 159, IOP Publishing Ltd, 159 (1999)

[22] S. M. Hooker and S. E. Harris, *Femtosecond-pulse-driven electron excited extreme ultraviolet lasers in Be-like ions*, Opt. Lett. **20** 1994 (1995).

[23] C. D. Decker, D. C. Eder and R. A. London, *Ionization induced refraction in recombination X-ray lasers*, Phys. Plasmas, **3** 414 (1996)

[24] G. A. Gudzenko and L. A. Shelepin, *Amplification in recombining plasmas*, Sov. Phys. JETP. **18** 998 (1965)

[25] G. J. Pert and S. A. Ramsden, *Population inversion in plasmas produced by picosecond laser pulses*, Opt. Comm. **11** 270 (1974).

[26] D. Jacoby, G. J. Pert, S. A. Ramsden, L. D. Shorrock and G. J. Tallents, *Observation of gain in possible extreme ultra-violet lasing system*, Opt. Comm. **37** 193 (1981)

[27] Y. Kato, E. Miura, T. Tachi, H. Shiraga, H. Nishimura, H. Daido, M. Yamanaka, T. Jitsuno, M. Takagi, P. R. Herman, H. Takabe, S. Nakai, C. Yamanakam M. H. Key, G. J. Tallents, S. J. Rose and P. T. Rumsby, *Observation of gain at 54.2Å on the Balmer-α transition of hydrogenic sodium*, Appl. Phys. B, **50** 247 (1990)

[28] J. Zhang, M. H. Key, P. A. Norrys, G. J. Tallents, A. Behjat, C. Danson, A. Demir, L. Dwivedi, M. Holden, P. B. Holden, C. L. S. Lewis,

A. G. MacPhee, D. Neely, G. J. Pert, S. A. Ramsden, S. J. Rose, Y. F. Shao, O. Thomas, F. Walsh and Y. L. You, *Demonstration of high gain in a recombination XUV laser at 18.2nm driven by a 20J, 2ps glass laser,* Phys. Rev. Lett. **74** 1335 (1995)

[29] J. Zhang, E. E. Fill, Y. Li, D. Schlögl, J. Steingruber, M. Holden, G. J. Tallents, A. Demir, P. Zeitoun, C. Danson, P. A. Norreys, F. Walsh, M. H. Key, C. L. S. Lewis and A. G. MacPhee, *High gain x-ray lasing at 11.1 nm in sodium like copper driven by a 20 J 2 ps Nd:glass laser*, Opt. Lett. **15** 1035 (1996)

[30] Y. Nagata, K. Midorikawa, S. Kubodera, M. Obara, H. Tashiro and K. Toyoda, *Soft X-ray amplification of the Lyman-α transition by optical field induced ionisation,* Phys. Rev. Lett. **71** 3774 (1993)

[31] D. V. Korobkin, C. H. Nam, and S. Suckewer. *Lasing to the ground state in LiIII at 13.5nm*, X-Ray Lasers 1996, Inst. Of Phys. Conf. Ser. No 151, IOP Publishing Ltd, pp.151 (1996).

[32] K. Okasaka, T. Kawachi, H. Oyama, T. Hara, N. Yamaguchi and K. Ando, *Effect of wave envelope of pulse train laser on production of X-ray laser gain in recombining lithium-like aluminium plasmas*, X-Ray Lasers 1998, Inst. Of Phys. Conf. Ser. No 159, IOP Publishing Ltd, pp.223 (1999).

[33] M. J. Grout, *Optical field induced gas mixture breakdown for recombination X-ray lasers*, DPhil thesis, University of York, (1997).

[34] S. B. Healy and G. J. Pert, *Simulations of inner-shell photoionization X-ray lasers*, X-Ray Lasers 1996, Inst. Of Phys. Conf. Ser. No 151, IOP Publishing Ltd, pp.169 (1996).

[35] W. T. Silfvast and O. R. Wood II, *Investigations of a new inner shell photionisation laser at 165 nm in the mercury ion*, JOSA B, **4** 609 (1987).

[36] A. Tunnermann, H. Eichmann, A Maezing, M. Hube and B. Wellegahausen, *Photoionisation lasers pumped by broad band soft x-ray flux from laser produced plasmas*, JOSA B, **8** 2042 (1991).

[37] H. C. Kapteyn and R. W. Falcone, *Auger pumped short wavelength lasers in xenon and krypton*, Phys. Rev. A, **37** 2033 (1988).

[38] A. L'Huillier, L. A. Lompré, G. Mainfray and C. Manus, *High order harmonic generation in rare gases*, Atoms in Intense Laser Fields, Boston Academic Press (1992).

[39] K. Zhai, Z. Ku, Y. Wang, X. Li, Y. Liu, X. Yang, Z. Zhang, R. Li and W. Zhang, *High-order harmonic generation in ionized gas media with a 45fs intense laser source*, X-Ray Lasers 1998, Inst. Of Phys. Conf. Ser. No 159, IOP Publishing Ltd, pp.523 (1999).

[40] J. W. G. Tisch, T. Ditmire, D. J. Fraser, N. Hay, M. B. Mason, E. Springate, J. P. Marangos and M. H. R. Hutchinson, *Investigations of high-harmonic generation from xenon atom clusters*, JOSA B, **30** L709 (1997).

[41] S. G. Preston, A. Sanpera, M. Zepf, W. J. Blyth, C. G, Smith, J. S. Walk, M. H. Key, K. Burnett, M. Nakai, D. Neely and A. A. Offenberger, *High order harmonics of 248.5nm KrF laser from helium and neon ions*, Phys. Rev. A, **53** R32 (1996).

[42] P. A. Norreys, M. Zepf, S. Moustaizis, A. P. Fews, J. Zhang, P. Lee, M. Bakarezos, C. N. Danson, A. Dyson, P. Gibbon, P. Loukakos, D. Neely, F. N. Walsh, J. S. Wark and A. E. Dangor, *Efficient extreme UV harmonics generated from picosecond laser-pulse interactions with solid targets*, Phys Rev. Lett. **76** 1832 (1996).

[43] J. M. Madley, *Stimulated emission of Bremsstrahlung in a periodic magnetic field*, J. Appl. Phys. **42** 1906 (1971)

[44] W. B. Colson, *Short wavelength free electron lasers in 1996*, Nucl. Instr. and Meth. in Phys. Res. **A375** 669 (1996)

[45] K. Takahashi, R. Kodama, K. A. Tanaka, H. Hashimoto, Y. Kato, K. Mima, F. A. Weber, T. W. Barbee and L. B. Da Silva, *Laser hole boring into overdense plasmas measured with soft x-ray laser probing*, Phys. Rev. Lett. **84** (2000) 2405

[46] S. Augst, D. Strickland, D. Meyerhöfer, S. L. Chin and J. Eberly, *Tunnelling ionisation of noble gases in a high intensity laser field*, Phys. Rev. Lett. **63** 2122 (1989)

[47] L. V. Keldysh, *Ionisation in the field of a strong electromagnetic wave*, Soviet Physics JETP, **20** (5) 1307 (1965).

[48] S. August, D. D. Meyerhofer, D. Strickland and S. L. Chin, *Laser ionisation of noble gases by Coulomb-barrier suppression*, JOSA B, **8** (1991) 858

[49] B. M. Smirnov and M. I. Chesbisov, *Ionisation of atomic particles by an electric field and by electron impact*, Soviet Physics JETP, **22** (3) 585 (1966).

[50] A. M. Perelomov, V. S. Popov and M. V. Terent'ev, *Ionisation of atoms in an alternating electric field*, Soviet Physics JETP, **23** (5) 924 (1966).

[51] M. V. Ammosov, N. B. Delone and V. B. Krainov, *Tunnel ionisation of complex atoms and of atomic ions in an alternating electromagnetic field*, Soviet Physics JETP, **64** (6) 1191 (1986).

[52] S. C. Rae and K. Burnett, *Possible production of cold plasmas through optical field induced ionisation*, Phys. Rev. A, **46** 2077 (1992)

[53] G. J. Pert, *Electron distributions generated by tunnelling ionisation during gas breakdown by high intensity laser radiation*, JOSA B, **32** 27 (1999)

[54] N. H. Burnett and P. B. Corkum, *Cold plasma production for recombination extreme ultraviolet lasers by optical field ionisation*, JOSA B, **6** 1195 (1989).

[55] N. B. Delone and V. P. Krainov, *Energy and angular electron spectra for the tunnel ionisation of atoms by strong low frequency radiation*, JOSA B, **8** 1207 (1991)

[56] P. B. Corkum, N. H. Burnett and F. Brunel, *above threshold ionisation in the long wavelength limit*, Phys. Rev. Lett. **75** 445 (1989)

[57] M. B. Smirnov and V. P. Krainov, *Hot electrons in the tunnelling ionisation of atoms*, J. Phys. B, **31** L519 (1998)

[58] V. P. Krainov, *Energy and angular distribution of relativistic electrons in the tunnelling ionisation of atoms by circularly polarised light*, Journal of Physics B, **32** 1607 (1999)

[59] G. J. Pert, *Inverse bremsstrahlung in strong radiation fields at low temperatures*, Phys. Rev. E, **51** 4778 (1995)

[60] A. Y. Polishchuk and J. Meyer-ter-Vehn, *Electron – ion relaxation in a plasma interacting with an intense laser field*, Phys. Rev. E, **49** 663 (1994)

[61] Y. B. Zeldovich and Y. P. Raizer, *Physics of shock waves and high temperature phenomena*, Academic Press (1966)

[62] M. Dunne, T. Afshar-Rad, J. Edwards, A. J. MacKinnon, S. M. Viana, O. Willia and G. J. Pert, *Experimental observations of the expansion of an optical-field-induced ionisation channel in a gas jet,* Phys, Rev. Lett, **72** 102 (1994)

[63] L. Spitzer, *Physics of fully ionised gases, 2nd edition*, Interscience Publishers (1962).

[64] A. R. Bell, R. G. Evans and D. J. Nicholas, *Electron energy transport in steep temperature gradients in laser produced plasmas*, Phys. Rev. Lett. **46** 243 (1981).

[65] G. J. Pert, *The calculation of the electron distribution function following tunnelling ionisation using a Fokker-Planck method*, J. Phys B, **34** 881 (2001)

[66] M. N. Rosenbluth, W. M. MacDonald and D. L. Judd, *Fokker-Planck equation for an inverse square force*, Phys. Rev. 2nd Series, **107** 1 (1957)

[67] D. Kim, D. Kim and A. L. Osterheld, *Characteristics of populations and gains in neon like argon (Ar IX)*, Journal of Applied Physics, **84** (11) 5862 (1998)

[68] R. D. Cowan, *The theory of atomic structure and spectra*, University of California Press, Berkeley, California (1981).

[69] S. B. Healy, K. A. Janulewicz, G. J. Pert, *Short wavelength lasing on collisionally pumped, highly excited 2s hole states of neon like ions in preformed plasmas irradiated with intense picosecond pulses*, Optics Communications, **144** 24 (1997).

[70] E. P. Ivanova, L. V. Knight, A. Reyes-Mena, Proc. Laser 94 (1994).

[71] S. M. Hooker, *Inner shell soft X-Ray lasers in Ne-like ions driven by optical field ionisation*, Opt. Comm. **182** 209 (2000).

[72] J. Hawkes and I. Latimer, *Lasers – Theory and Practice,* Prentice Hall International Series in Optoelectronics (1995)

[73] M. J. Grout, G. J. Pert and A. Djaoui, *Propagation effects in optical field induced gas mixture breakdown for recombination x-ray lasers*, J. Phys. B, **31** 197 (1998).

[74] R. Rankin, C. E. Capjack, N. H. Burnett and P. B. Corkum, *Refraction effects associated with multiphoton ionisation and ultrashort-pulse laser propagation in plasma wavguides*, Opt. Lett. **16** 835 (1991)

[75] G. J. Pert, *Output characteristics of amplified-stimulated-emission lasers*, JOSA B, **11** 1425 (1994)

[76] W. L. van Wyngaarden, K. Bhadra and R. J. W. Henry, *Excitation of helium like ions by electron impact*, Phys. Rev. A. **20** 1409 (1979)

[77] D. Salzman, *Atomic physics in hot plasmas*, Oxford University Press (1998).

[78] H. van Regemorter, *Rate of collisional excitation in stellar atmospheres*, Astrophys. J. **A132** 906 (1962)

[79] W. Lotz, Z. Phys., **216** 241 (1968)

[80] D. R. Bates, A. E. Kingston, R. W. P. McWhirter, *Recombination between atomic electrons and ions in optically thin plasmas*, Proc. R. Soc., **267A** 297 (1962)

[81] R. W. P. McWhirter and A. G. Hearn, *A calculation of the instantaneous population densities of the excited levels of hydrogen-like ions in a plasma*, Proc. Phys. Soc., **82** 641 (1963)

[82] A. Burgess, and H. P. Summers, *The recombination and level populations of ions in hydrogen and hydrogenic ions*, Mon. Not. R Astron. Soc., **174** 345 (1976)

[83] G. J. Pert, *Models of collisional-radiative recombination*, J. Phys. B, **23** 619 (1990)

[84] G. J. Pert and S. J. Rose, *Detailed simulations of XUV recombination XUV laser experiments*, Appl. Phys. B, **50** 307 (1990)

[85] P. L. Hagelstein and R. K. Jung, *Relativistic distorted-wave calculations of electron collision cross sections and rate coefficients for Ne-like ions*, Atomic and Nuclear Data Tables, **37** 121 (1987)

[86] D. H. Sampson, H. L. Zhang and C. J. Fontes, *Relativistic distorted wave collision strengths and oscillator strengths for Ne-like ions with* $22 \leq Z \leq 92$, Atomic and Nuclear Data Tables, **48** 25 (1991)

[87] M. Cornille, J. Dabau and S. Jacquemot, *Radiative and collisional atomic data for Ne-like ions*, Atomic and Nuclear Data Tables, **58** 1 (1994)

[88] I. P. Grant, B. J. McKenzie, P. H. Norrington, D. F. Meyers and N. C. Pyper, *An atomic multiconfigurational Dirac-Fock package*, Comp. Phys. Comm., **21** 207 (1980)

[89] N. Shanthi, P. C. Deshmilch and S. T. Marson, *Near threshold structure in the photoionisation of krypton 3p*, Phys. Rev A. **38** 1773 (1988)

[90] C. Guo, *Fully relativistic distorted wave Born procedure for electron-impact excitation*, Phys. Rev. A, **53** 3227 (1996)

[91] W. Eissner, *The UCL distorted wave code*, Comp. Phys. Comm., **114** 295 (1998)

[92] R. E .King, Private communication (2000)

[93] Y. Li, J. Nilsen, J. Dunn and A. L. Osterheld, *Wavelengths of the Ni-like* $4d\ ^1S_0 \rightarrow 4p\ ^1P_1$ *x-ray laser line*, Phys. Rev A, **58** R2668 (1998)

[94] J. Sugar and V. Kaufman, *Resonance lines in the Pd I isoelectronic sequence*, Phys. Scr. **26** 419 (1982)

[95] W. C. Martin, J. Sugar and A. Musgrove, *Atomic Spectra Database*, National Institute of Standards and Technology, http://physics.nist.gov/cgi-bin/AtData/main_asd

[96] S. C. Rae, *Ionisation induced defocusing of intense laser pulses in high-pressure gases*, Opt. Comm., **97** 25 (1993)

[97] S. Jackel, *Channelling of terawatt laser pulses by the use of hollow wave guides*, Opt. Lett. **20** 1086 (1995)

[98] M. Borghesi, A. J. Mackinnon, R. Gaillard, O. Willi and A. A. Offenberger, *Guiding of a 10 TW picoseconds laser pulse through hollow capillary tubes*, Physical Review E, **57** (5) R4899 (1998).

[99] A. B. Borisov, A. V. Borovskiy, V. V. Korobkin, A. M. Prokhorov, J. C. Solem, T. S. Luk, K. Boyer and C. K. Rhodes, *Observation of relativistic and charge displacement self-channeling of intense subpicosecond ultraviolet (248nm) radiation in plasmas,* Phys. Rev. Lett. **68** 2309 (1992).

[100] P. Sprangle and E. Esarey, *Interaction of ultrahigh laser fields with beams and plasmas*, Phys. Fluids B, **4** 2241 (1992)

[101] P. Sprangle, E. Esarey, J. Krall and G. Joyce, *Propagation and guiding of intense laser pulses in plasmas*, Phys. Rev. Lett, **69** 2200 (1992)

[102] E. Esarey, J. Krall and P. Sprangle, *Envelope analysis of intense laser pulse self modulation in plasmas*, Phys. Rev. Lett, **72** 2887 (1994)

[103] D. J. Spence and S. M. Hooker, *Simulations of the propagation of high intensity laser pulses in discharge ablated capillary waveguides*, JOSA B, **17** (9) 1565 (2000)

[104] D. Kaganovich, A. Ting, C. I. Moore, A. Zigler, H. R. Burris, Y. Ehrlich, R. Hubbard and P. Sprangle, *High efficiency guiding of terawatt subpicosecond laser pulses in a capillary discharge plasma channel*, Physical Review E, **59** (5) R4769 (1999)

[105] D. J. Spence and S. M. Hooker, *Investigation of a hydrogen plasma waveguide*, Physical Review E, **63** 1 (2000)

[106] Y. Ehrlich, C. Cohen, A. Zigler, J. Krall, P. Sprangle and E. Esarey, *Guiding of high intensity laser pulses in straight and curved plasma channel experiments*, Phys. Rev. Lett. **77** 4186 (1996)

[107] S. M. Hooker, D. J. Spence and R. A. Smith, *Guiding of high intensity picosecond laser pulses in a discharge ablated capillary waveguide*, JOSA B, **17** 90 (2000)

[108] C. G. Durfee III and H. M. Milchberg, *Light pipe for high intensity laser pulses*, Phys. Rev. Lett.**71** 2409 (1993).

[109] T. R. Clarke and H. M. Milchberg, *Time and space resolved density evolution of the plasma waveguide*, Phys. Rev. Lett. **78** 2373 (1997).

[110] A. Klisnick, D. Ros, P. Zeiton, F. Albert, A. Carillon, P. Fourcade, S. Hubert, P. Jaeglé, G. Jamelot, C. L. S. Lewis, A. MacPhee, R. O'Rouke, R. Keenan, P. Nickles, K, Janulewicz, M. Kalashnikov, J. Warwickk, L. C. Chanteloup, E. Salmon, C. Sauteret, J. P. Zou, D. Joyeux and D. Phalippou, *Generation of intense Ni-like x-ray lasers at LULI from 130ps to 350fs pumping pulses*, X-Ray Lasers 1998, Inst. Of Phys. Conf. Ser. No 159, IOP Publishing Ltd, pp.107 (1999)

[111] S. P. Nikitin, I. Alexeev, J. Fan and H. M. Milchberg, *High efficiency coupling and guiding of intense femtosecond laser pulses in preformed plasma channels in an elongated gas jet*, Phys. Rev. E, **59** R3839 (1999).

[112] Y. A. Zeldovich and Y. P. Raizer, *Physics of Shock Wave and High Temperature Hydrodynamic Phenomena*, Academic Press, New York (1966).

[113] T. Hosokai, S. Kondo, M. Kando, M. Nakajima, K. Horioka and K. Nakjima, *Development of a plasma wavguide using fast capillary discharges,* X-Ray Lasers 1998, Inst. Of Phys. Conf. Ser. No 159, IOP Publishing Ltd, pp.179 (1999).

[114] R. L. Burton and F. D. Witherspoon, *Energy-mass coupling in high pressure liquid injected gas*, IEEE trans. Plasma Sci. **19** 340 (1991).

[115] Y. Ehrlich *Generation of large high density homogeneous plasma by capillary discharge*, Appl. Phys. Lett, **64** 3542 (1994).

[116] Z. Tingbin and S. J. Rose, *Numerical simulation of the electron distribution function in a fully ionised plasma*, Unpublished.